

ACOUSTIC MULTIPLE REFLECTION ELIMINATION IN THE IMAGE DOMAIN AND IN THE DATA DOMAIN

Dissertation

for the purpose of obtaining the degree of doctor

at Delft University of Technology,

by the authority of Rector Magnificus Prof. dr. ir. T.H.J.J. van der Hagen,

chair of the Board of Doctorates,

to be defended publicly on Thursday 12 December 2019 at 12.30 hours

by

Lele ZHANG

Master of Science in Solid Earth Physics,

University of Chinese Academy of Sciences, Beijing, China,

Born in Gansu, China

This dissertation has been approved by the

Promotor: Prof. dr. ir. E.C. Slob

Composition of the doctoral committee:

Rector Magnificus

Chairman

Prof. dr. ir. E.C. Slob

Delft University of Technology, promotor

Independent members:

Prof. dr. W.A. Mulder

Delft University of Technology

Prof. dr. Y. Wang

Chinese Academy of Sciences

Dr. K. de Vos

Shell Global Solutions Int.

Dr. ir. D.J. Verschuur

Delft University of Technology

Other members:

Prof. dr. ir. C.P.A. Wapenaar

Delft University of Technology

Dr. ir. J.W. Thorbecke

Delft University of Technology



Printed by: Gildeprint

Copyright © 2019 by L. Zhang. All rights reserved. No part of this publication may be reproduced or distributed in any form or by any means, or stored in a database or retrieval system, without the prior written permission of the publisher.

ISBN 978-94-6384-094-1

An electronic version of this dissertation is available at

<http://repository.tudelft.nl/>.

Contents

Contents	iii
Summary	vi
Samenvatting	viii
1 Introduction	1
1.1 Free-surface related multiple reflections	1
1.2 Internal multiple reflections	2
1.3 Marchenko schemes	3
1.4 Thesis objective and outline	4
References	5
2 Artefact-free Reverse Time Migration	9
2.1 Introduction	10
2.2 Theory	10
2.3 Example	13
2.4 Conclusions	16
References	16
3 Marchenko Multiple Elimination and Transmission compensated Marchenko Multiple Elimination	18
3.1 Introduction	19
3.2 Marchenko multiple elimination (MME)	20
3.2.1 Theory	20
3.2.2 Examples	22
3.3 Transmission compensated Marchenko multiple elimination (T-MME)	28
3.3.1 Theory	28
3.3.2 Examples	32
3.4 Limitation analysis	36
3.4.1 Thin layer example	36
3.4.2 Refracted wave example	38
3.4.3 Scattered wave example	39
3.5 Discussion	41
3.6 Conclusions	42
References	42
4 Extension of MME and T-MME schemes to account for free-surface related multiple reflections	45

4.1 Introduction.....	46
4.2 Extended MME scheme.....	46
4.2.1 Theory.....	46
4.2.2 Example.....	49
4.3 Extended T-MME scheme.....	53
4.3.1 Theory.....	53
4.3.2 Example.....	54
4.4 Discussion.....	61
4.5 Conclusions.....	62
References.....	62
5 Fast implementation of T-MME scheme.....	63
5.1 Fast implementation of T-MME.....	64
5.1.1 Theory.....	64
5.1.2 Example.....	66
5.2 Fast implementation of extended T-MME.....	70
5.2.1 Theory.....	70
5.2.2 Example.....	71
5.3 Discussion.....	76
5.4 Conclusions.....	76
References.....	76
6 Laboratory and Field Examples.....	77
6.1 Laboratory Example.....	78
6.1.1 Synthetic 2D dataset.....	78
6.1.2 Laboratory 2D dataset.....	81
6.1.3 Discussion.....	83
6.2 Field example.....	84
6.2.1 Application of MME scheme.....	84
6.2.2 Application of T-MME scheme.....	92
6.2.3 Discussions.....	100
6.3 Conclusions.....	101
References.....	101
7 General Conclusions.....	102
Acknowledgments.....	105
Curriculum Vitae.....	107
List of Publications.....	108

Summary

One of the most crucial estimates retrieved from measured seismic reflection data is the subsurface image. The image provides detailed information of the subsurface of the Earth. Seismic reflection data consists of so-called primary and multiple reflections. Primary reflections are events that have been reflected a single time, while multiple reflections have been reflected multiple times before they are recorded by the receivers. Most current migration algorithms assume all reflections in the data are primary reflections. Hence, in order to retrieve an accurate image of the subsurface, multiple reflections need to be eliminated before migration. Keeping the multiple reflections in the measured seismic reflection data will lead to a sub-optimal image of the subsurface, because the multiple reflections will be imaged as if they were primary reflections. Such artefacts in the image can cause erroneous interpretation.

In this thesis, I studied the elimination of multiple reflections in the image domain and in the data domain. This is a challenging topic that attracts much attention from industry and academia. Free-surface and internal multiple reflections can be predicted without information about the subsurface and be subtracted from measured seismic reflection data based on adaptive filtering. Adaptive filtering minimises the energy in a seismic dataset, which is a constraint that cannot distinguish multiple reflections from primary reflections. As a consequence, when primary and multiple reflections are recorded as overlapping events, unintentionally, they will be removed together by the filter. The main research question is whether it is possible to eliminate multiple reflections without impairment of the primary reflections and to design a method that can easily be incorporated in routine work flows presently used in industry.

An artefact-free (reverse time) migration scheme is derived from a revised implementation of the Marchenko redatuming scheme using a modified time-truncation operator. Because of the modified truncation operator, the time-reversed version of the standard wavefield-extrapolation operator is used as initial estimate to retrieve the upgoing focusing function from the regular Marchenko equations. Then, the retrieved upgoing focusing function can be used to directly image the subsurface by correlating it with the standard wavefield-extrapolation operator. Correspondingly, as I show using a synthetic example, an artefact-free RTM image of the subsurface is retrieved.

Then, based on the projected version of the regular Marchenko equations with symmetric and asymmetric time-truncation operators, I derive the Marchenko multiple elimination (MME) and transmission compensated Marchenko multiple elimination (T-MME) schemes. Both schemes can eliminate internal multiple reflections in data domain without subsurface information or adaptive filtering. In the T-MME scheme, the amplitudes of the retrieved

primary reflections are compensated for transmission effects. Furthermore, the MME and T-MME schemes are extended to account for free-surface related multiple reflections. Still, no subsurface information or adaptive filtering is required for the implementation. The potential benefits of MME and T-MME schemes are validated with synthetic examples, showing that multiple reflections can be successfully eliminated without subsurface information or adaptive filtering.

Next, I present a fast implementation of T-MME and extended T-MME schemes to reduce the computational cost. The synthetic examples show that the computational cost is reduced by an order of magnitude. The fast implementation also works for MME and extended MME schemes.

Finally, I apply the MME scheme to a measured laboratory and a field dataset to test the performance. The results show that the performance of the MME scheme largely depends on high-quality pre-processing. The investigation of the application of the MME and T-MME schemes shows that both are appropriate methods to remove internal multiple reflections in reflection data acquired in exploration geophysics.

Samenvatting

De afbeelding van de ondergrond is een van de meest belangrijke schattingen verkregen uit seismische reflectiemetingen. The afbeelding verschaft gedetailleerde informatie over de ondergrond van de Aarde. Seismische reflecties bevatten zogenaamde primaire en meervoudige reflecties. Primaire reflecties zijn events die éénmaal gereflecteerd zijn, terwijl meervoudige reflecties meerdere reflecties ondergaan hebben voordat ze worden opgenomen door de ontvangers. Migratie algoritmen veronderstellen dat alle gemeten reflecties primaire reflecties zijn. Hierdoor moeten meervoudige reflecties eerst worden verwijderd om een nauwkeurig beeld te verkrijgen. Als de meervoudige reflecties in de metingen blijven zitten zal dat tot een suboptimale afbeelding van de ondergrond leiden, omdat de meervoudige reflecties zullen worden afgebeeld alsof zij primaire reflecties waren. Zulke artefacten in de afbeelding kunnen foutieve interpretaties veroorzaken.

In dit proefschrift bestudeer ik het verwijderen van meervoudige reflecties in het domein van de afbeelding en in het domein van de data. Dit is een uitdagend onderwerp dat veel aandacht trekt van de industrie en academies. Vrije-oppervlakte en interne meervoudige reflecties kunnen worden voorspeld zonder informatie over de ondergrond en kunnen worden afgetrokken van de gemeten seismische reflectie data met behulp van zogenaamde adaptieve filtertechnieken. Adaptieve filtertechnieken minimaliseren de energie in een seismische dataset, wat een dwingende regel is die geen onderscheid kan maken tussen primaire en meervoudige reflecties. De consequentie is dat indien primaire en meervoudige reflecties overlappen in de meting, zij per ongeluk samen zullen worden verwijderd door het filter. De hoofdonderzoeksvraag is of het mogelijk is om meervoudige reflecties te verwijderen zonder negatieve invloed op de primaire reflecties en om een methode te ontwerpen die gemakkelijk kan worden ingevoegd in de huidige routinematige data verwerkingstechnieken die door de industrie worden gebruikt.

Een artefact-vrij omgekeerde tijd migratieschema (RTM) wordt afgeleid uit de gewijzigde implementatie van het Marchenko schema waarbij de datum wordt verplaatst van het meetoppervlak naar een bepaald diepteniveau, door gebruik te maken van een nieuwe tijd-afkap operator. Vanwege deze nieuwe tijd-afkap operator wordt de standaard golfveld extrapolatie operator gebruikt in omgekeerde tijd als eerste schatting om de omhoog propagerende golven in de focuserende functie te bepalen. Dat deel van de focuserende functie kan dan worden gebruikt om direct te ondergrond af te beelden door het te correleren met de standaard golfveldextrapolatie operator. Ik laat met een numeriek model zien dat de overeenkomstige artefact vrije RTM-afbeelding van de ondergrond wordt verkregen.

Dan leid ik, gebaseerd op de geprojecteerde versie van de Marchenko vergelijkingen met symmetrische en niet symmetrische tijd-afkap operatoren, de Marchenko meervoudige

reflectie eliminatie (MME) en transmissie effect gecompenseerde Marchenko meervoudige reflectie eliminatie (T-MME) schema's af. Beide schema's kunnen interne meervoudige reflecties verwijderen uit de data zonder informatie over de ondergrond of adaptieve filters te gebruiken. In het T-MME schema worden de amplitudes van de primaire reflecties gecompenseerd voor de transmissie effecten die optreden tijdens de propagatie van oppervlak naar een reflector en weer terug naar het oppervlak. Verder worden beide schema's uitgebreid zodat ze ook werken in het geval dat meervoudige reflecties die gerelateerd zijn aan het oppervlak in de data aanwezig zijn. Nog steeds zijn informatie over de ondergrond en adaptieve filtertechnieken niet nodig voor de implementatie. De potentiële voordelen van de MME en T-MME schema's worden gevalideerd met numerieke voorbeelden, die laten zien dat meervoudige reflecties succesvol kunnen worden verwijderd zonder informatie over de ondergrond of adaptieve filtertechnieken.

Daarna presenteer ik een snelle implementatie van het T-MME schema en zijn uitbreiding om de rekenkosten te reduceren. De numerieke voorbeelden laten een reductie in rekestijd zien van een factor tien. De snelle implementatie werkt op het MME schema en zijn uitbreiding.

Tenslotte pas ik het MME schema toe op een in het laboratorium gemeten dataset om de prestatie te testen. De resultaten laten zien dat de prestatie voornamelijk afhangt van de kwaliteit waarmee de data wordt verwerkt op een manier die recht doet aan de golfvergelijking. Het onderzoek naar de toepassing van het MME en T-MME schema op data gemeten in de exploratie geofysica laat zien dat beide methode geschikt zijn om interne meervoudige reflecties uit de data te verwijderen.

1

Introduction

The processing of acoustic or elastodynamic reflection data plays a central role in seismic exploration and seismology. For seismic exploration, the measured data is the earth reflection response, generated by an active source that emits a signal from the surface or inside the subsurface. The observations are made with the aid of receivers located up to kilometers away from the source. The measured data contain primary reflections followed by multiple reflections. In standard migration images, strong artefacts due to multiple reflections are present in marine (Van Borselen, 2002) and land seismic data (Verschuur et al., 1992; Kelamis et al., 2006) because migration schemes assume only primary reflections have occurred in the medium. The artefacts degrade the quality of the image (Weglein, 2016) and cause erroneous interpretation.

1.1 Free-surface related multiple reflections

The free-surface related multiple reflections can be very strong compared with the measured reflection responses from the subsurface. These free-surface related multiple reflections cause major ghost reflectors in the migration image. Several schemes have been developed to eliminate the free-surface related multiple reflections. The surface-related multiple elimination (SRME) scheme of Verschuur et al. (1992) is a good example. SRME consists of two steps: free-surface related multiple reflection prediction and subtraction. In the first step, free-surface related multiple reflections are predicted by convolution of the traces in the measured data. Because the source wavelet is not known exactly, the predicted events differ from actual events in the measured data. Hence, adaptive subtraction is required to subtract the predicted free-surface related multiple reflections from the measured data in the second step. Unfortunately, adaptive subtraction has a major problem. The energy is minimized which leads to removal of primary reflections when primary and free-surface related multiple reflections overlap in time, which happens quite often in field data. The estimation of primaries by sparse inversion (EPSI) (van Groenestijn and Verschuur, 2009) replaces the two-step processing of SRME, prediction and adaptive subtraction, by a full-waveform inversion process. Both the SRME and EPSI have achieved success for synthetic and field datasets (Lopez and Verschuur, 2015) and been widely accepted as robust tools for free-surface related multiple reflection attenuation in the industry.

Many researchers try to use free-surface related multiple reflections in migration to improve the image quality. [Verschuur and Berkhout \(2005\)](#) propose to transform free-surface related multiple reflections into primary reflections and then the retrieved primary reflections can be imaged using conventional migration schemes. [Guitton \(2002\)](#) and [Shan \(2003\)](#) propose to use free-surface related multiple reflections as areal sources in the migration of single-sided dataset and VSP dataset ([Xiao and Schuster, 2009](#)). [Zuberi and Alkhalifah \(2013\)](#) propose to forward and backward propagate the recorded dataset with free-surface related multiple reflections in reverse time migration. [Wang et al. \(2014, 2017\)](#) propose to eliminate artefacts due to reverse time migration of free-surface related multiple reflections in angle domain common image gathers or by using the wavefield decomposition imaging condition. Although using free-surface related multiple reflections for migration can give extended illumination of the subsurface, crosstalk is present in the resulting image as coherent noise.

1.2 Internal multiple reflections

Besides free-surface related multiple reflections there are internal multiple reflections that also introduce ghost reflectors in the migration image. The internal multiple reflections can be strong enough to cause artefacts in land and marine seismic data and less effort has been devoted to their removal.

A method that relies on discrimination of move-out between primary and internal multiple reflections is proposed by [Hampson \(1986\)](#). Unfortunately, it is difficult to distinguish the move-out velocities of internal multiple reflections from those of primary reflections in most cases. The internal multiple elimination scheme (IME) proposed by [Berkhout and Verschuur \(1997\)](#) is a layer-stripping scheme. The IME scheme downward extrapolates shot records to a virtual surface and attenuates internal multiple reflections related to that surface. Therefore, velocity information is required for its implementation. Adaptive subtraction is also required for subtracting predicted events from the measured data because of the approximate nature of the predicted events. [Jakubowicz \(1998\)](#) proposes to combine three primary reflections to predict and attenuate the first-order internal multiple reflections. However, these primary reflections need to be identified and picked from the measured reflection response. [Araújo et al. \(1994\)](#) derive a scheme for internal multiple reflection attenuation from Inverse Scattering Series (ISS), which has been developed in more detail by [Weglein et al. \(1997\)](#). The ISS aims to find the scattering potential of the subsurface relative to a chosen background model. [Ten Kroode \(2002\)](#) modified the ISS scheme to approximately predict and subtract internal multiple reflections from the data. This involves removing the background medium and changing depth truncations to time truncations. [Löer et al. \(2016\)](#) derive the same scheme from source-receiver interferometry and ISS. The approximate nature of the predicted events implies that a global or local matching filter is required to subtract the predicted internal multiple reflections from the measured reflection response ([Matson et al., 1999](#); [Luo et al., 2011](#); [de Melo et al., 2014](#)). Using internal multiple reflections in imaging is done via full wavefield migration (FWM) in a close-loop scheme ([Berkhout, 2014](#)). [Davydenko and Verschuur \(2018\)](#) show results of applying FWM on field dataset.

1.3 Marchenko schemes

Recently, Marchenko redatuming schemes have been introduced to deal with internal multiple reflections (Slob et al., 2014; Wapenaar et al., 2014a). For these schemes, up- and downgoing focusing functions with a focal point at an arbitrary position in the subsurface can be retrieved by solving the coupled Marchenko equations and up- and downgoing Green's functions can be computed from the associated Green's function representations once the focusing functions are known. By deconvolving the retrieved upgoing Green's function with the downgoing Green's function, a virtual reflection response with virtual source and virtual receivers in the subsurface can be obtained. The virtual reflection response forms the basis for obtaining an artefact-free image when the zero-time-lag crosscorrelation between the retrieved up- and downgoing virtual responses is extracted at all image points (Wapenaar et al., 2014b; Broggini et al., 2014). The image can also be formed by deconvolving the retrieved upgoing Green's function with the first event of the downgoing Green's function, which makes the deconvolution processing much cheaper (van der Neut et al., 2018). Singh et al. (2015, 2017) extend the Marchenko redatuming scheme to account for free-surface related multiple reflections, such that the free-surface and internal multiple reflections are accounted for in one step and do not end up in the migration image. Ravasi (2017) modifies the scheme of Singh et al. (2017) for marine data and shows the performance in synthetic and field examples. Thus, source and receiver ghosts, free-surface and internal multiple reflections are successfully accounted for in one step. Meles et al. (2018) propose a different time-focusing condition of the Marchenko redatuming scheme for the retrieval of virtual plane-wave response. The plane-wave scheme allows multiple-free imaging with a fraction of the computational cost of the regular Marchenko scheme. Although it is derived initially for acoustic wavefield, the Marchenko scheme has been extended to elastic media (Wapenaar and Slob, 2014) and to dissipative media (Slob, 2016). Except for the 1D case, these variants of Marchenko redatuming schemes require an estimate of the first arrival of the downgoing focusing function to be able to create a virtual receiver inside the medium. This estimation requires a smooth velocity model to be built before the method can be applied. The quality of this initial estimate has influence on the quality of the final image.

Based on the Marchenko redatuming scheme and convolutional interferometry, an internal multiple reflection attenuation scheme has been proposed by Meles et al. (2015) to predict internal multiple reflections with approximate amplitude. Model information and adaptive subtraction are required for its implementation. Van der Neut and Wapenaar (2016) rewrite the coupled Marchenko equations by projecting focusing points back to the acquisition surface to avoid the requirement of macro model information. An overburden elimination scheme can be derived from the projected Marchenko scheme, which can be extended to eliminate all orders of internal multiple reflections that are initiated in the overburden. In the implementation, velocity model information is needed to create time truncations. Wapenaar et al. (2018) derive a homogeneous Green's function retrieval scheme from the regular Marchenko redatuming scheme, where the homogeneous Green's function between any two points inside a medium can be retrieved from the measured single-sided reflection response.

Staring et al. (2018) derive a source-receiver Marchenko redatuming scheme for internal multiple reflection attenuation and the application to field dataset validates the success. Knowledge of the medium and adaptive subtraction are required for this scheme. Many other methods, such as target oriented velocity analysis (Mildner et al., 2017), equations for inverse source problems (van der Neut et al., 2017) and immersive wave simulation (Elison et al., 2018), are also derived from the regular Marchenko redatuming scheme.

1.4 Thesis objective and outline

The objective of this thesis is motivated by the presence of multiple reflections in the measured dataset in exploration geophysics. Despite the fact that a variety of schemes dealing with free-surface and internal multiple reflections exist, as described above, until now the multiple reflection elimination is still a popular topic and attracts much attention from academia and industry. The aim of this study is to develop schemes for dealing with multiple reflections without adaptive subtraction in data domain or in image domain that can be easily incorporated in routine operational workflows for seismic data processing. The main body of this thesis consists of six chapters.

- Chapter 2 presents an improved reverse-time migration scheme to image the medium without artefacts arising from internal multiple reflections. This is based on a revised implementation of Marchenko redatuming scheme using a modified time-truncation operator. Because of the modified truncation operator, we can use the time-reversed version of the standard wavefield-extrapolation operator as initial estimate for retrieving the upgoing focusing function. Then, the retrieved upgoing focusing function can be used to directly image the medium by correlating it with the standard wavefield-extrapolation operator. This imaging scheme can be seen as an artefact-free reverse-time migration scheme with two terms. The first term gives the conventional reverse-time migration image with wrong amplitudes and artefacts due to internal multiple reflections. The second term gives a correction image which removes artefacts in the image generated by the first term. We illustrate the method with a two-dimensional synthetic example that illustrates the effectiveness of the method.
- Chapter 3 is split into two parts. In the first part we propose a Marchenko multiple elimination (MME) scheme to retrieve primary reflections in the two-way travel time domain. The MME scheme is derived from the projected version of the regular Marchenko equations presented by van der Neut and Wapenaar (2016). This scheme works with the acoustic subsurface reflection response. There is no model information or adaptive subtraction required for the implementation. In the second part, we propose a transmission compensated Marchenko multiple elimination (T-MME) scheme to remove internal multiple reflections and compensate for transmission losses in primary reflections. The T-MME scheme is also derived from the projected version of the modified Marchenko equations. Still, no model information or adaptive subtraction is required for its implementation. For both MME and T-MME methods, the measured data works as its own filter. The retrieved datasets by both schemes can be used as

inputs to construct better velocity models than the one that would be obtained by working directly with the original data, and to construct enhanced subsurface images. Synthetic examples show the effectiveness of both methods. We study limitations by analyzing the effects of the presence of a thin layer on the ability to remove internal multiple reflections. Presence of refracted and scattered waves are known limitations of both methods and we study them as well. Our analysis shows that a thin layer is treated as a more complicated reflector and internal multiple reflections related to the thin layer are properly removed. We find that the presence of refracted and scattered waves generate artefacts in the retrieved data.

- Chapter 4 is also split into two parts. It is an extension of Chapter 3 to account for free-surface related multiple reflections. In the first part we extend the MME scheme to account for free-surface related multiple reflections. Thus, both free-surface and internal multiple reflections can be eliminated in one step. In the second part, we extend the T-MME scheme to deal in one step with free-surface and internal multiple reflections and compensate for transmission losses in primary reflections. Still, no model information or adaptive subtraction is required for the implementation of these schemes. We evaluate the success of both methods with two-dimensional synthetic examples.
- Chapter 5 presents the fast implementation of T-MME and extended T-MME schemes. The substantial computational cost of both MME and T-MME schemes can be reduced by an order of magnitude with a fast implementation version. This is achieved by using the previously computed filter functions as initial estimate for every new truncation time value. Considering the similarity of MME and T-MME schemes, we give only the fast implementation of the T-MME and the extended T-MME schemes in detail in this chapter. 2D synthetic examples are given to illustrate the success.
- Chapter 6 shows the applications of the MME and T-MME schemes on Laboratory and field datasets. They are the first measured data examples to validate the capabilities of both schemes for removal of internal multiple reflections without model information or adaptive subtraction. Here we only focus on the application of both schemes, because the underlying theory is given in Chapter 3. The performance of both schemes is analysed in some detail in the discussion section.
- Chapter 7 concludes the thesis.

References

- Araújo, F. V., A. B. Weglein, P. M. Carvalho, and R. H. Stolt, 1994, Inverse scattering series for multiple attenuation: An example with surface and internal multiples: 64th Annual Meeting, SEG, Expanded Abstracts, 1039–1041.
- Berkhout, A. J., and D. J. Verschuur, 1997, Estimation of multiple scattering by iterative inversion, Part I: Theoretical considerations: *Geophysics*, **62**, 1586–1595.

- Berkhout, A. J., 2014, Review paper: An outlook on the future of seismic imaging. Part II: Full-wavefield migration: *Geophysical Prospecting*, **62**, 931–949.
- Broggini, F., R. Snieder, and K. Wapenaar, 2014, Data-driven wave field focusing and imaging with multidimensional deconvolution: Numerical examples from reflection data with internal multiples: *Geophysics*, **79**, no. 3, WA107–WA115.
- Davydenko, M., and D. J. Verschuur, 2018, Including and using internal multiples in closed-loop imaging—Field data examples: *Geophysics*, **83**, no. 4, R297–R305.
- de Melo, F. X., M. Idris, Z. J. Wu, and C. Kostov, 2014, Cascaded internal multiple attenuation with inverse scattering series: 84th Annual Meeting, SEG, Expanded Abstracts, 4113–4117.
- Elison, P., D. J. van Manen, J. O. A. Robertsson, M. S. Dukalski, and K. de Vos, 2018, Marchenko-based immersive wave simulation: *Geophysical Journal International*, **215**, 1118–1131.
- Guitton, A., 2002, Shot-profile migration of multiple reflections: 72nd Annual Meeting, SEG, Expanded Abstracts, 1296–1299.
- Hampson, D., 1986, Inverse velocity stacking for multiple elimination: *Canadian Journal of Exploration Geophysicists*, **22**, 44–55.
- Jakubowicz, H., 1998, Wave equation prediction and removal of interbed multiples: 68th Annual Meeting, SEG, Expanded Abstracts, 1527–1530.
- Kelamis, P. G., W. Zhu, K. O. Rufaii, and Y. Luo, 2006, Land multiple attenuation: The future is bright: 76th Annual Meeting, SEG, Expanded Abstracts, 2699–2703.
- Löer, K., A. Curtis, and G. A. Meles, 2016, Relating source-receiver interferometry to an inverse-scattering series to derive a new method to estimate internal multiples: *Geophysics*, **81**, no. 3, Q27–Q40.
- Lopez, G. A., and D. J. Verschuur, 2015, Closed-loop surface-related multiple elimination and its application to simultaneous data reconstruction: *Geophysics*, **80**, no. 6, V189–V199.
- Luo, Y., P. G. Kelamis, S. Huo, G. Sindi, S. Hsu, and A. B. Weglein, 2011, Elimination of land internal multiples based on the inverse scattering series: *The Leading Edge*, **30**, 884–889.
- Matson, K., D. Corrigan, A. Weglein, C. Young, and P. Carvalho, 1999, Inverse scattering internal multiple attenuation: Results from complex synthetic and field data examples: 89th Annual Meeting, SEG, Expanded Abstracts, 1060–1063.
- Mildner, C., F. Broggin, J. O. A. Robertsson, D. J. van Manen, and S. Greenhalgh, 2017, Target-oriented velocity analysis using Marchenko-redatumed data: *Geophysics*, **82**, R75–R86.
- Meles, G., K. Löer, M. Ravais, A. Curtis, and C. A. da Costa Filho, 2015, Internal multiple prediction and removal using Marchenko autofocusing and seismic interferometry: *Geophysics*, **80**, no. 1, A7–A11.

- Meles, G. A., K. Wapenaar, and J. Thorbecke, 2018, Virtual plane-wave imaging via Marchenko redatuming: *Geophysical Journal International*, **214**, 508-519.
- Ravasi, M., 2017, Rayleigh-Marchenko redatuming for target-oriented, true-amplitude imaging: *Geophysics*, **82**, no. 6, S439–S452.
- Shan, G., 2003, Source-receiver migration of multiple reflections: 73rd Annual Meeting, SEG, Expanded Abstracts, 1008–1011.
- Singh, S., R. Snieder, J. Behura, J. van der Neut, K. Wapenaar, and E. Slob, 2015, Marchenko imaging: Imaging with primaries, internal multiples, and free-surface multiples: *Geophysics*, **80**, no. 5, S165–S174.
- Singh, S., R. Snieder, J. van der Neut, J. Thorbecke, E. Slob, and K. Wapenaar, 2017, Accounting for free-surface multiples in Marchenko imaging: *Geophysics*, **82**, no. 1, R19–R30.
- Slob, E., K. Wapenaar, F. Broggini, and R. Snieder, 2014, Seismic reflector imaging using internal multiples with Marchenko-type equations: *Geophysics*, **79**, no. 2, S63–S76.
- Slob, E., 2016, Green's function retrieval and Marchenko imaging in a dissipative acoustic medium: *Physical Review Letters*, **116**, 164301.
- Staring, M., R. Pereira, H. Douma, J. van der Neut, and K. Wapenaar, 2018, Source-receiver Marchenko redatuming on field data using an adaptive double-focusing method: *Geophysics*, **83**, no. 6, S570–S590.
- Ten Kroode, P. E., 2002, Prediction of internal multiples: *Wave Motion*, **35**, 315–338.
- Van Borselen, R. G., 2002, Fast-track, data-driven interbed multiple removal: A North Sea data example: 64th Annual Meeting, EAGE, Extended Abstracts.
- van der Neut, J., and K. Wapenaar, 2016, Adaptive overburden elimination with the multidimensional Marchenko equation: *Geophysics*, **81**, no. 5, T265–T284.
- van der Neut, J., J. L. Johnson, K. van Wijk, S. Singh, E. Slob, and K. Wapenaar, 2017, A Marchenko equation for acoustic inverse source problems: *Journal of the Acoustical Society of America*, **141**, 4332-4346.
- Van der Neut, J., J. Brackenhoff, M. Staring, L. Zhang, S. de Ridder, E. Slob, and K. Wapenaar, 2018, Single- and Double-sided Marchenko Imaging Conditions in Acoustic Media: *IEEE Transactions on computational imaging*, **4**, no. 4, 160-171.
- van Groenestijn, G. J. A., and D. J. Verschuur, 2009, Estimating primaries by sparse inversion and application to near-offset data reconstruction: *Geophysics*, **74**, no. 3, A23–A28.
- Verschuur, D., A. Berkhout, and K. Wapenaar, 1992, Adaptive surface-related multiple elimination: *Geophysics*, **57**, 1166–1177.
- Verschuur, D. J., and A. J. Berkhout, 2005, Transforming multiples into primaries: Experience with field data: 75th Annual Meeting, SEG, Expanded Abstracts, 2103–2106.

- Wang, Y., Y. Zheng, L. Zhang, X. Chang, and Z. Yao, 2014, Reverse time migration of multiples: Eliminating migration artifacts in angle domain common image gathers: *Geophysics*, **79**, no. 6, S263–S270.
- Wang, Y., Y. Zheng, Q. Xue, X. Chang, T. W. Fei, and Y. Luo, 2017, Reverse time migration of multiples: Reducing migration artifacts using the wavefield decomposition imaging condition: *Geophysics*, **82**, no. 4, S307– S314.
- Wapenaar, K., and E. Slob, 2014, On the Marchenko equation for multicomponent single-sided reflection data: *Geophysical Journal International*, **199**, 1367–1371.
- Wapenaar, K., J. Thorbecke, J. van der Neut, F. Brogini, E. Slob, and R. Snieder, 2014a, Green’s function retrieval from reflection data, in absence of a receiver at the virtual source position: *Journal of the Acoustical Society of America*, **135**, 2847–2861.
- Wapenaar, K., J. Thorbecke, J. van der Neut, F. Brogini, E. Slob, and R. Snieder, 2014b, Marchenko imaging: *Geophysics*, **79**, no. 3, WA39– WA57.
- Wapenaar, K., J. Brackenhoff, J. Thorbecke, J. van der Neut, E. Slob, and E. Verschuur, 2018, Virtual acoustics in inhomogeneous media with single-sided access: *Scientific Reports*, **8**, 2497.
- Weglein, A. B., F. A. Gasparotto, P. M. Carvalho, and R. H. Stolt, 1997, An inverse scattering series method for attenuating multiples in seismic reflection data: *Geophysics*, **62**, 1975–1989.
- Weglein, A. B., 2016, Multiples: Signal or noise: *Geophysics*, **81**, no. 4, V283-V302.
- Xiao, X., and G. Schuster, 2009, Local migration with extrapolated VSP Green’s functions: *Geophysics*, **74**, no. 1, S115-S126.
- Zuberi, A., and T. Alkhalifah, 2013, Imaging by forward propagating the data: Theory and application: *Geophysical Prospecting*, **61**, 248–267.

2

Artefact-free Reverse Time Migration

In this chapter, we derive an improved reverse-time migration scheme to image the medium without artefacts arising from internal multiple reflections. This is based on a revised implementation of Marchenko redatuming scheme using a modified time-truncation operator. Because of the modified truncation operator, we can use the time-reversed version of the standard wavefield-extrapolation operator as initial estimate for retrieving the upgoing focusing function. Then, the retrieved upgoing focusing function can be used to directly image the medium by correlating it with the standard wavefield-extrapolation operator. This imaging scheme can be seen as an artefact-free reverse-time migration scheme with two terms. The first term gives the conventional reverse-time migration image with wrong amplitude and artefacts due to internal multiple reflections. The second term gives a correction image which removes artefacts in the image generated by the first term. We illustrate the method with a two-dimensional synthetic example that illustrates the success of the method.

2.1 Introduction

Recently, a novel iterative method, named Marchenko redatuming, has been introduced to retrieve the Green's function with a virtual receiver located in the subsurface of a 3D inhomogeneous medium. This Green's function is obtained from the single-sided reflection response measured at the surface. The development of the single-sided Marchenko scheme has been inspired by [Rose \(2002\)](#), who demonstrates that solving the 1D Marchenko equation can be seen as focusing a wave field inside the 1D medium. [Broggini and Snieder \(2012\)](#) introduce this to the geophysical field. They find that the 1D focusing function can be combined with the measured, single-sided reflection response to give the 1D Green's function with a virtual receiver at the focal point inside the medium. [Wapenaar et al. \(2013\)](#) derive the theory for 3D media. [Slob et al. \(2014\)](#) use reciprocity relations to create coupled Marchenko equations that can be solved for the up- and downgoing parts of the focusing function. The extension to 3D is given by [Wapenaar et al. \(2014a\)](#), where the obtained focusing function is used for retrieving the Green's function. The retrieved up- and downgoing parts of the Green's function can be used for retrieving the image without artefacts due to internal multiple reflections at any focal point ([Wapenaar et al., 2014b](#)). [Singh et al. \(2015, 2017\)](#) extend the Marchenko redatuming scheme to account for free-surface related multiple reflections, such that the free-surface and internal multiple reflections are accounted for in one step. [Ravasi \(2017\)](#) modifies the scheme of [Singh et al. \(2017\)](#) for marine data and shows the performance in synthetic and field examples. [Meles et al. \(2018\)](#) propose a different time-focusing condition of the Marchenko redatuming scheme for the retrieval of virtual plane-wave response. The plane-wave scheme allows multiple-free imaging with a fraction of the computational cost of the regular Marchenko scheme. Although it is derived initially for acoustic wavefield, the Marchenko scheme has been extended to elastic media ([da Costa Filho et al., 2014](#); [Wapenaar and Slob, 2014](#)) and to dissipative media ([Slob, 2016](#)).

In this chapter, we present a revised Marchenko redatuming scheme by applying a modified truncation operator. We show that due to the modified truncation operator the seismic reflection data is redatumed using the first arrival of the downgoing Green's function, which is a standard wavefield extrapolator used for redatuming the sources. Based on this scheme, we derive a migration scheme to image the medium without artefacts arising from internal multiple reflections. We show that the first term of this scheme is equal to the conventional reverse-time migration (RTM) scheme and the second term gives the correction image which eliminates the artefacts in the conventional RTM image. Hence, the second term can also be used to correct an existing RTM image when the same dataset and macro model are available. We give a 2D synthetic example to illustrate the performance of the proposed method.

2.2 Theory

We indicate time as t and the position vector of a spatial coordinate as $\mathbf{x} = (x, y, z)$, where z denotes depth and (x, y) denote the horizontal coordinates. An acoustically transparent

acquisition boundary $\partial\mathbf{D}_0$ is defined at $z_0 = 0$. For convenience, the coordinates at $\partial\mathbf{D}_0$ are denoted as $\mathbf{x}_0 = (\mathbf{x}_H, z_0)$, with $\mathbf{x}_H = (x, y)$. Similarly, the position vector of a point at an arbitrary depth level $\partial\mathbf{D}_i$ is denoted as $\mathbf{x}_i = (\mathbf{x}_H, z_i)$, where z_i denotes the depth of $\partial\mathbf{D}_i$. We express the acoustic impulse reflection response as $R(\mathbf{x}'_0, \mathbf{x}_0, t)$, where \mathbf{x}_0 denotes the source position and \mathbf{x}'_0 denotes the receiver position, both located at the acquisition surface $\partial\mathbf{D}_0$. In practice when using field data, it means that first free-surface effects and source wavelet should be removed from the measured reflection response. The focusing function $f_1(\mathbf{x}_0, \mathbf{x}_i, t)$ is the solution of the homogeneous wave equation in a truncated medium and focuses at the focal point \mathbf{x}_i . We define the truncated domain as $z_0 < z < z_i$. Inside the truncated domain, the properties of the medium are equal to the properties of the physical medium. Outside the truncated domain, the truncated medium is reflection-free. The Green's function $G(\mathbf{x}_i, \mathbf{x}_0, t)$ is defined for an impulsive source that is excited at \mathbf{x}_0 and a receiver that is positioned at the focal point \mathbf{x}_i . The Green's function is defined in the same physical medium as the measured data. The focusing and Green's functions can be partitioned into up- and downgoing parts and for this we use pressure-normalized quantities (Wapenaar et al., 2014a).

We start with the 3D versions of one-way reciprocity theorems for pressure-normalized wave fields and use them for the depth levels z_0 and z_i . When the medium above the acquisition level z_0 is reflection-free, the Green's function representations are given by (Slob et al., 2014; Wapenaar et al., 2014a),

$$G^-(\mathbf{x}_i, \mathbf{x}'_0, t) = \int_{\partial\mathbf{D}_0} d\mathbf{x}_0 \int_0^{+\infty} R(\mathbf{x}'_0, \mathbf{x}_0, t') f_1^+(\mathbf{x}_0, \mathbf{x}_i, t - t') dt' - f_1^-(\mathbf{x}'_0, \mathbf{x}_i, t), \quad (2.1)$$

$$G^+(\mathbf{x}_i, \mathbf{x}'_0, -t) = -\int_{\partial\mathbf{D}_0} d\mathbf{x}_0 \int_{-\infty}^0 R(\mathbf{x}'_0, \mathbf{x}_0, -t') f_1^-(\mathbf{x}_0, \mathbf{x}_i, t - t') dt' + f_1^+(\mathbf{x}'_0, \mathbf{x}_i, t). \quad (2.2)$$

Superscripts $+$ and $-$ stand for downgoing and upgoing parts, respectively. We write the downgoing Green's function as the sum of a direct part and a coda:

$$G^+(\mathbf{x}_i, \mathbf{x}_0, t) = G_d^+(\mathbf{x}_i, \mathbf{x}_0, t) + G_m^+(\mathbf{x}_i, \mathbf{x}_0, t), \quad (2.3)$$

where G_d^+ indicates the direct part and G_m^+ the following coda. As explained in Wapenaar et al. (2014a), the Green's and focusing functions in equations 2.1 and 2.2 are separated in time except for the first event in f_1^+ and the last event in $G^+(-t)$ in equation 2.2 that coincide with each other. We rewrite equations 2.1 and 2.2 with the help of equation 2.3 as

$$f_1^-(\mathbf{x}'_0, \mathbf{x}_i, t) = \int_{\partial\mathbf{D}_0} d\mathbf{x}_0 \int_0^{+\infty} R(\mathbf{x}'_0, \mathbf{x}_0, t') f_1^+(\mathbf{x}_0, \mathbf{x}_i, t - t') dt', \quad \text{for } -t_d - \varepsilon < t < t_d + \varepsilon \quad (2.4)$$

$$f_1^+(\mathbf{x}'_0, \mathbf{x}_i, t) - G_d^+(\mathbf{x}_i, \mathbf{x}'_0, -t) = \int_{\partial\mathbf{D}_0} d\mathbf{x}_0 \int_{-\infty}^0 R(\mathbf{x}'_0, \mathbf{x}_0, -t') f_1^-(\mathbf{x}_0, \mathbf{x}_i, t - t') dt', \quad \text{for } -t_d - \varepsilon < t < t_d + \varepsilon \quad (2.5)$$

where t_d denotes the one-way travel time from a surface point \mathbf{x}'_0 to the focusing point \mathbf{x}_i , and ε is a positive value to account for the finite bandwidth. Note that the truncation interval is longer in equations 2.4 and 2.5 than in the regular Marchenko scheme ($-t_d + \varepsilon < t < t_d - \varepsilon$) given by Wapenaar et al. (2014a). The left extension of the truncation interval ensures that the time-reversed G_d^+ is present in equation 2.5, while it is excluded in the regular Marchenko scheme (Wapenaar et al., 2014a). The right extension of the truncation interval ensures that when the focusing point is at a reflector, the reflection of that reflector is the last event in f_1^- . For this focusing point, this reflection would be the first event in G^- in the scheme of Wapenaar et al. (2014a). We give equations 2.4 and 2.5 in operator form as

$$f_1^-(\mathbf{x}'_0, \mathbf{x}_i, t) = [\Theta \mathbf{R} f_1^+](\mathbf{x}'_0, \mathbf{x}_i, t), \quad (2.6)$$

$$f_1^+(\mathbf{x}'_0, \mathbf{x}_i, t) = [\Theta \mathbf{R}^* f_1^- + G_d^{+*}](\mathbf{x}'_0, \mathbf{x}_i, t), \quad (2.7)$$

where G_d^{+*} indicates the time-reversed version of G_d^+ , \mathbf{R} indicates an integral operator of the measured data R with any wavefield as in equation 2.4, \mathbf{R}^* a similar correlation integral operator as in equation 2.5, and Θ is a time window to exclude values outside the interval $(-t_d - \varepsilon, t_d + \varepsilon)$ as indicated by the time window in equations 2.4 and 2.5. Then, we substitute equation 2.7 into equation 2.6 to get the final equation for f_1^- as

$$[(\mathbf{I} - \Theta \mathbf{R} \Theta \mathbf{R}^*) f_1^-](\mathbf{x}'_0, \mathbf{x}_i, t) = [\Theta \mathbf{R} G_d^{+*}](\mathbf{x}'_0, \mathbf{x}_i, t). \quad (2.8)$$

We expand equation 2.8 as a Neumann series to give the equation as

$$f_1^-(\mathbf{x}'_0, \mathbf{x}_i, t) = [\Theta \mathbf{R} G_d^{+*}](\mathbf{x}'_0, \mathbf{x}_i, t) + \left[\sum_{m=1}^{\infty} (\Theta \mathbf{R} \Theta \mathbf{R}^*)^m \Theta \mathbf{R} G_d^{+*} \right](\mathbf{x}'_0, \mathbf{x}_i, t). \quad (2.9)$$

The first term in the right-hand side of equation 2.9 is the reflection response redatumed to the subsurface point \mathbf{x}_i by the redatuming operator G_d^+ . It is truncated to make sure the result is set to zero for $t > t_d + \varepsilon$. The second term in the right-hand side of equation 2.9 predicts and removes multiple reflections that occur in the reflection data in the time window. It thereby removes the transmission effects of the primary reflections between the acquisition plane and the depth level of the focusing point. When the focal point coincides with an actual subsurface reflector, its primary reflection will occur in f_1^- at time instant t_d . Otherwise, the value in f_1^- at that time instant will be zero. For each pair of points in the left-hand side of equation 2.9, we are interested only in the value of f_1^- at time instant t_d . By carrying out downward extrapolation at the receiver side, we create the image at the focal point. Correlating both sides of equation 2.9 with G_d^+ gives

$$\mathbf{I}(\mathbf{x}_i, \mathbf{x}_i, t) = [\mathbf{G}_d^{+*} \mathbf{R} \mathbf{G}_d^{+*} + \mathbf{G}_d^{+*} \sum_{m=1}^{\infty} (\Theta \mathbf{R} \Theta \mathbf{R}^*)^m \Theta \mathbf{R} \mathbf{G}_d^{+*}](\mathbf{x}_i, \mathbf{x}_i, t), \quad (2.10)$$

with $\mathbf{I}(\mathbf{x}_i, \mathbf{x}_i, t)$ defined as the space-time image function, and \mathbf{G}_d^{+*} indicates a correlation integral operator of G_d^+ with any wavefield. The possible primary reflection of interest in f_1^- at t_d occurs at $t=0$ after the downward extrapolation. For this reason, we do not need to keep the time window in the first term in equation 2.10. We can now understand that the

image function $\mathbf{I}(\mathbf{x}_i, \mathbf{x}_i, t)$ can be used for estimating the artefact-free image of the point \mathbf{x}_i at $t = 0$. The first term in the right-hand side of equation 2.10 can be understood as the conventional RTM scheme. It produces the conventional RTM image of the point \mathbf{x}_i at $t = 0$, in which artefacts due to internal multiple reflections can be present. Consequently, the second term in the right-hand side of equation 2.10 can be seen as an operator expression for eliminating transmission effects in the primary reflections and for removing artefacts contained in the conventional RTM image. It uses only the single-sided reflection response and simple time truncations together with the same information needed to construct a conventional RTM image. The scheme easily fits in routine RTM migration operations. We state that equation 2.10 presents an improved RTM scheme which can be used for retrieving the artefact-free image of the subsurface.

2.3 Example

The aim of the current method is to image the medium without artefacts arising from internal multiple reflections and without using more information than in standard migration schemes. To illustrate the method, we give a 2D synthetic example. Figure 2.1a shows the values for the acoustic velocity as a function of depth and horizontal position. Figure 2.1b is the smoothed velocity model which will be used to do the conventional and artefact-free RTM. The dipole source emits a Ricker wavelet with 20Hz centre frequency. We have computed the single-sided reflection responses with 601 sources and 601 pressure receivers on a fixed spread with a spacing of 10 m at the top of the model. Absorbing boundary conditions are applied around the model and the direct wave has been removed. One of the computed single-sided reflection responses convolved with the source wavelet is shown in Figure 2.2a. Note that internal multiple reflections occur at later arrival times. First arrivals of the downgoing Green's functions have been modelled based on the smoothed model shown in Figure 2.1b with sources at focal points and receivers at the acquisition surface. One of the computed first arrivals convolved with the source wavelet is shown in Figure 2.2b. The computed single-sided reflection responses and time-reversed first arrivals are used as inputs to solve equation 2.10 with $m = 1, \dots, 20$. The resulting artefact-free image of the target zone is shown in Figure 2.3a. Then, the procedure as described using the first term in the right-hand side of equation 2.10, is applied and leads to the conventional RTM image of the target zone shown in Figure 2.3b. Note that Figure 2.3b contains artefacts from internal multiple reflections because they are imaged as if they were primary reflections. However, the image in Figure 2.3a obtained with the new scheme is nearly perfect without ghost images due to internal multiple reflections. For both images, the smoothed velocity model shown in Figure 2.1b was used and the two figures can be compared as best-case scenarios.

In the derivation of the current method, we assumed the medium to be lossless. The method can be adapted to work with two-sided reflection and transmission data in dissipative media (Slob, 2016). We further assumed that the Green's functions and the focusing functions can be separated in time, that the source wavelet can be well recovered and deconvolved, and we

ignored evanescent waves (Wapenaar et al., 2013). These restrictions limit the application of the current method. For situations in which these assumptions are fulfilled, the 2D synthetic example illustrates that the current method has a good potential for applying it to field data. Applicability to field data requires properly sampled data, which condition can be fulfilled in 2D but is not fulfilled in 3D data acquisition and modifications will be necessary before the method can work on 3D data (Jia and Snieder, 2018).

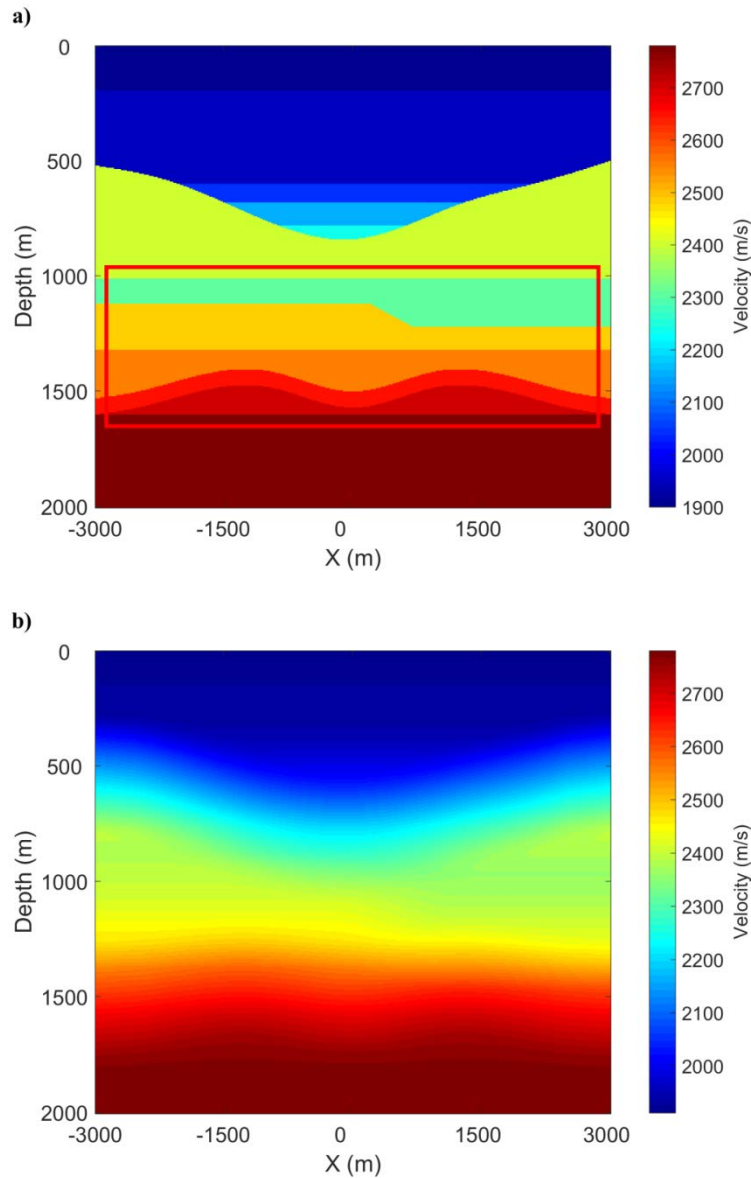


Figure 2.1: (a) Velocity model which will be used to model the reflection response, the red box gives the target zone which will be imaged. (b) The smoothed velocity model which will be used to model the first arrival of the downgoing Green's function.

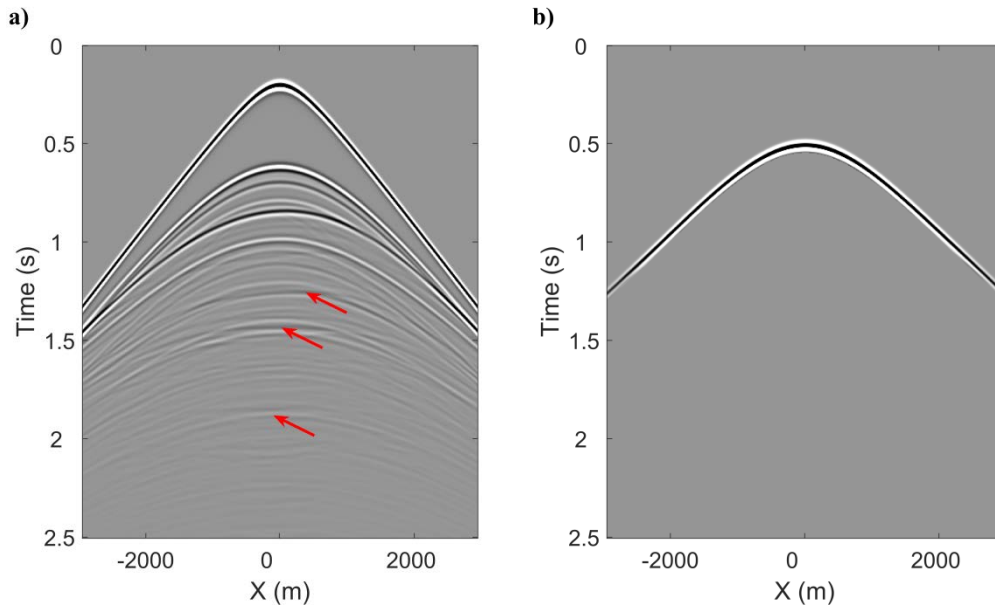


Figure 2.2: (a) The modeled reflection response with source and receivers at the acquisition surface. The red arrows indicate the internal multiple reflections. (b) The modeled first arrival of the downgoing Green's function with source at the focal point in the subsurface and receivers at the acquisition surface.

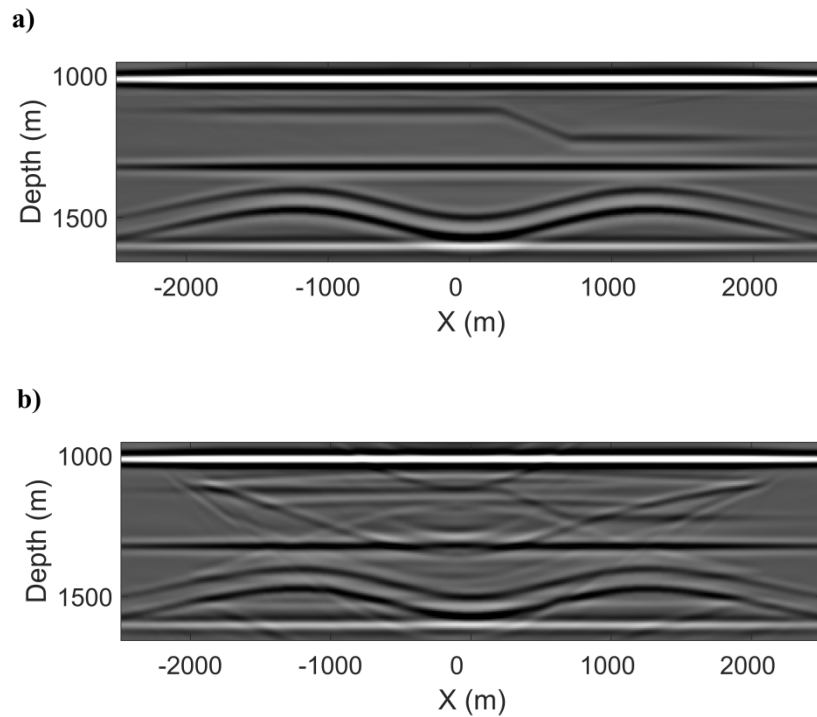


Figure 2.3: (a) The artefact-free image of the target zone retrieved by equation 2.10. (b) The image of the target zone retrieved by the first term in the right-hand side of equation 2.10.

2.4 Conclusions

We have shown that an artefact-free reverse-time migration (RTM) image can be constructed based on a revised Marchenko scheme. The revised Marchenko redatuming scheme is applied using a modified truncation operator and a time-reversed version of the standard wavefield-extrapolation operator as initial estimate. Based on this, we derived an artefact-free RTM scheme, which can be used to image the medium without artefacts arising from internal multiple reflections. The new migration scheme uses the same macro-velocity model as the conventional RTM scheme. The constructed image does not contain artefacts because the data acts as an operator to remove artefacts generated by the conventional RTM scheme in the imaging domain. When the velocity model is accurate, the image is nearly perfect as shown with a numerical example.

References

- Broggini, F., and R. Snieder, 2012, Connection of scattering principles: A visual and mathematical tour: *European Journal of Physics*, **33**, 593–613.
- da Costa Filho, C. A., M. Ravasi, A. Curtis, and G. A. Meles, 2014, Elastodynamic Green's function retrieval through single-sided Marchenko inverse scattering: *Physical Review E*, **90**, 063201.
- Jia, X., and R. Snieder, 2018, 3D Marchenko redatuming: SEG Technical Program Expanded Abstracts.
- Meles, G. A., K. Wapenaar, and J. Thorbecke, 2018, Virtual plane-wave imaging via Marchenko redatuming: *Geophysical Journal International*, **214**, 508-519.
- Ravasi, M., 2017, Rayleigh-Marchenko redatuming for target-oriented, true-amplitude imaging: *Geophysics*, **82**, no. 6, S439–S452.
- Rose, J. H., 2002, Single-sided autofocusing of sound in layered materials: *Inverse Problems*, **18**, 1923–1934.
- Singh, S., R. Snieder, J. Behura, J. van der Neut, K. Wapenaar, and E. Slob, 2015, Marchenko imaging: Imaging with primaries, internal multiples, and free-surface multiples: *Geophysics*, **80**, no. 5, S165–S174.
- Singh, S., R. Snieder, J. van der Neut, J. Thorbecke, E. Slob, and K. Wapenaar, 2017, Accounting for free-surface multiples in Marchenko imaging: *Geophysics*, **82**, no. 1, R19–R30.
- Slob, E., K. Wapenaar, F. Broggin, and R. Snieder, 2014, Seismic reflector imaging using internal multiples with Marchenko-type equations: *Geophysics*, **79**, no. 2, S63–S76.
- Slob, E., 2016, Green's function retrieval and Marchenko imaging in a dissipative acoustic medium: *Physical Review Letters*, **116**, 164301.

- Wapenaar, K., F. Broggini, E. Slob, and R. Snieder, 2013, Threedimensional single-sided Marchenko inverse scattering, data-driven focusing, Green's function retrieval, and their mutual relations: *Physical Review Letters*, **110**, 084301.
- Wapenaar, K., and E. Slob, 2014, On the Marchenko equation for multicomponent single-sided reflection data: *Geophysical Journal International*, **199**, 1367–1371.
- Wapenaar, K., J. Thorbecke, J. van der Neut, F. Broggini, E. Slob, and R. Snieder, 2014a, Green's function retrieval from reflection data, in absence of a receiver at the virtual source position: *Journal of the Acoustical Society of America*, **135**, 2847–2861.
- Wapenaar, K., J. Thorbecke, J. van der Neut, F. Broggini, E. Slob, and R. Snieder, 2014b, Marchenko imaging: *Geophysics*, **79**, no. 3, WA39–WA57.

3

Marchenko Multiple Elimination and Transmission compensated Marchenko Multiple Elimination

In this chapter, we present two schemes (MME and T-MME) for internal multiple reflection elimination in the two-way travel time domain. The MME scheme focuses only on internal multiple reflection elimination without touching primary reflections. The T-MME scheme removes internal multiple reflections, while the amplitudes of the retrieved primary reflections are compensated for two-way transmission losses. For both schemes, the measured dataset is its own filter. It consists of convolutions and correlations of the data with itself. A truncation in the time domain is applied after each convolution or correlation. The retrieved dataset by both schemes can be used as inputs to construct better velocity models than the one that would be obtained by working directly with the original data and to construct artefact-free subsurface images. 2D synthetic examples show the effectiveness of both methods. We study bandwidth limitations by analyzing the effects of the presence of a thin layer on the ability of the scheme to remove associated internal multiple reflections. Presence of refracted and scattered waves are known limitations of both methods and we study them as well. Our analysis shows that a thin layer seems to be treated as a reflector with more complicated response and internal multiple reflections related to the thin layer are properly removed. We find that the presence of refracted and scattered waves generate artefacts in the retrieved data.

3.1 Introduction

In standard migration images, strong artefacts can occur due to internal multiple reflections in marine (Hadidi and Verschuur, 1997; Van Borselen, 2002) and land seismic data (Kelamis et al., 2006). Several schemes have been proposed to predict and subtract internal multiple reflections from measured data before the imaging procedure, such as internal multiple elimination (IME) (Berkhout and Verschuur, 2005) and inverse scattering series (ISS) (Weglein et al., 1997). IME is a layer-stripping method and requires the identification of the multiple generators in the input data. The subtraction of the predicted internal multiple reflections has to be performed by a least-squares matching filter with a minimum-energy criterion. The minimum-energy criterion can unintentionally lead to reduction or elimination of primary reflections. The ISS-based method predicts internal multiple reflections without model information (Weglein et al., 1997; Ten Kroode et al., 2002; L er et al., 2016). A global or local matching filter is usually required to subtract the predicted internal multiple reflections from the measured data (Matson et al., 1999; Luo et al., 2011; de Melo et al., 2014).

Based on the Marchenko redatuming scheme and convolutional interferometry, an internal multiple reflection attenuation scheme has been proposed by Meles et al. (2015) to predict internal multiple reflections with approximate amplitude. Staring et al. (2018) derive a source-receiver Marchenko redatuming scheme for internal multiple reflection attenuation and the application to field dataset validates the success. The Marchenko redatuming scheme requires an estimate of the first arrival of the downgoing focusing function to be able to create a virtual receiver inside the medium. This estimation requires a smooth velocity model to be built before the method can be applied. Hence, both methods mentioned above require model information and adaptive subtraction for the implementation.

Van der Neut and Wapenaar (2016) show that by projecting the focusing functions for all focusing points at a particular depth level back to a receiver location at the acquisition surface, the requirement of the estimation of the unknown initial downgoing focusing function is eliminated in this scheme. An internal multiple reflection elimination scheme can be derived from the projected version with a macro velocity model required for estimating the truncation time. In this chapter, we propose two model-free multiple elimination schemes (MME and T-MME). The MME scheme is a modified version of van der Neut and Wapenaar (2016) for internal multiple reflection elimination only. The T-MME scheme removes all orders of internal multiple reflections, while the amplitudes of the retrieved primary reflections are compensated for two-way transmission losses. This chapter is organized as follows. In the first section, we start with the single-sided Green's function representations and show how the MME scheme can be derived from the regular Marchenko equations. In the second section, we start with the revised Marchenko equations and show how the T-MME scheme can be derived. 2D synthetic examples are given to validate the success of both schemes. A section about the limitations of the T-MME scheme investigates the effects of limited bandwidth with a thin layer model. Refracted and scattered waves are not accounted for in the theory and we also investigate the effects of their presence in the data. All

limitations of the T-MME scheme are shared with the MME scheme because both schemes are derived from the same basic theory.

3.2 Marchenko multiple elimination (MME)

3.2.1 Theory

To develop the theory, we indicate time as t and the position vector of a spatial coordinate as $\mathbf{x} = (x, y, z)$, where z denotes depth and (x, y) denote the horizontal coordinates. The acoustically transparent acquisition boundary $\partial\mathbf{D}_0$ is defined as $z_0 = 0$. For convenience, the coordinates at $\partial\mathbf{D}_0$ are denoted as $\mathbf{x}_0 = (\mathbf{x}_H, z_0)$, with $\mathbf{x}_H = (x, y)$. Similarly, the position vector of a point at an arbitrary depth level $\partial\mathbf{D}_i$ is denoted as $\mathbf{x}_i = (\mathbf{x}_H, z_i)$, where z_i denotes the depth of $\partial\mathbf{D}_i$. We express the acoustic impulse reflection response as $R(\mathbf{x}'_0, \mathbf{x}_0, t)$, where \mathbf{x}_0 denotes the source position and \mathbf{x}'_0 the receiver position. In practice, it means that the free-surface effects should be removed from the data and the source time signature must be known. The focusing function $f_1(\mathbf{x}_0, \mathbf{x}_i, t)$ is the solution of the homogeneous wave equation in a truncated medium and focuses at the focal point \mathbf{x}_i . We define the truncated medium between $z_0 < z < z_i$. Inside the truncated domain and on its boundaries, the properties of the medium are equal to the properties of the physical medium. Outside the truncated domain, the truncated medium is reflection-free. The Green's function $G(\mathbf{x}_i, \mathbf{x}_0, t)$ is defined for an impulsive source that is excited at \mathbf{x}_0 and for a receiver positioned at the focal point \mathbf{x}_i . The Green's function is defined in the same medium as the measured data. The focusing and Green's functions can be partitioned into up- and downgoing constituents and for this we use pressure-normalized quantities (Wapenaar et al., 2014a).

We start with the 3D versions of one-way reciprocity theorems for pressure-normalized wave fields and use them for the depth levels z_0 and z_i . When the medium above the acquisition level z_0 is reflection-free, the Green's function can be represented as (Slob et al., 2014; Wapenaar et al., 2014a)

$$G^-(\mathbf{x}_i, \mathbf{x}'_0, t) = \int_{\partial\mathbf{D}_0} d\mathbf{x}_0 \int_0^{+\infty} R(\mathbf{x}'_0, \mathbf{x}_0, t') f_1^+(\mathbf{x}_0, \mathbf{x}_i, t - t') dt' - f_1^-(\mathbf{x}'_0, \mathbf{x}_i, t), \quad (3.1)$$

$$G^+(\mathbf{x}_i, \mathbf{x}'_0, -t) = -\int_{\partial\mathbf{D}_0} d\mathbf{x}_0 \int_{-\infty}^0 R(\mathbf{x}'_0, \mathbf{x}_0, -t') f_1^-(\mathbf{x}_0, \mathbf{x}_i, t - t') dt' + f_1^+(\mathbf{x}'_0, \mathbf{x}_i, t). \quad (3.2)$$

Superscripts $+$ and $-$ stand for downgoing and upgoing fields, respectively. The downgoing component of the focusing function $f_1^+(\mathbf{x}_0, \mathbf{x}_i, t)$ is the inverse of the transmission response in the truncated medium. We can write both the focusing function and the transmission response as the sum of a direct part and a coda

$$f_1^+(\mathbf{x}_0, \mathbf{x}_i, t) = f_{1d}^+(\mathbf{x}_0, \mathbf{x}_i, t) + f_{1m}^+(\mathbf{x}_0, \mathbf{x}_i, t), \quad (3.3)$$

$$T(\mathbf{x}_i, \mathbf{x}_0, t) = T_d(\mathbf{x}_i, \mathbf{x}_0, t) + T_m(\mathbf{x}_i, \mathbf{x}_0, t), \quad (3.4)$$

where f_{1d}^+ and T_d indicate the direct part, whereas f_{1m}^+ and T_m indicate the following coda. Wapenaar et al. (2014b) show that

$$\int_{\partial D_i} d\mathbf{x}_i \int_0^{+\infty} T_d(\mathbf{x}_i, \mathbf{x}_0'', t') f_{1d}^+(\mathbf{x}_0, \mathbf{x}_i, t-t') dt' = \delta(\mathbf{x}_H'' - \mathbf{x}_H) \delta(t), \quad (3.5)$$

where $\delta(\mathbf{x}_H)$ is a spatially band-limited 2D delta function in space and $\delta(t)$ is a delta function in time. Equation 3.5 means that T_d is the inverse of f_{1d}^+ in the sense that it collapses f_{1d}^+ to a delta function in horizontal coordinates and time. Following van der Neut and Wapenaar (2016), we apply multidimensional convolution with T_d as shown in equation 3.5 to both sides of equations 3.1 and 3.2 to find

$$U^-(\mathbf{x}_0'', \mathbf{x}_0', t, t_2) + v^-(\mathbf{x}_0', \mathbf{x}_0'', t, t_2) = \int_{\partial D_0} d\mathbf{x}_0 \int_0^{+\infty} R(\mathbf{x}_0', \mathbf{x}_0, t') (\delta(t-t') \delta(\mathbf{x}_H'' - \mathbf{x}_H) + v_m^+(\mathbf{x}_0, \mathbf{x}_0'', t-t', t_2)) dt', \quad (3.6)$$

$$\delta(t) \delta(\mathbf{x}_H'' - \mathbf{x}_H') + v_m^+(\mathbf{x}_0', \mathbf{x}_0'', t, t_2) - U^+(\mathbf{x}_0'', \mathbf{x}_0', -t, t_2) = \int_{\partial D_0} d\mathbf{x}_0 \int_{-\infty}^0 R(\mathbf{x}_0', \mathbf{x}_0, -t') v^-(\mathbf{x}_0, \mathbf{x}_0'', t-t', t_2) dt', \quad (3.7)$$

with v^- and v_m^+ defined as

$$v^-(\mathbf{x}_0', \mathbf{x}_0'', t, t_2) = \int_{\partial D_i} d\mathbf{x}_i \int_0^{+\infty} T_d(\mathbf{x}_i, \mathbf{x}_0'', t') f_1^-(\mathbf{x}_0', \mathbf{x}_i, t-t') dt', \quad (3.8)$$

$$v_m^+(\mathbf{x}_0', \mathbf{x}_0'', t, t_2) = \int_{\partial D_i} d\mathbf{x}_i \int_0^{+\infty} T_d(\mathbf{x}_i, \mathbf{x}_0'', t') f_{1m}^+(\mathbf{x}_0', \mathbf{x}_i, t-t') dt', \quad (3.9)$$

where U^- and U^+ are G^- and G^+ projected to the acquisition surface, similar as shown in equations 3.8 and 3.9 for f_1^- and f_{1m}^+ , t_2 denotes the two-way travel time from a surface point \mathbf{x}_0' to the focusing level z_i and back to the surface point \mathbf{x}_0'' . Note that, because U^\pm and v^\pm are functions related to t_2 , we introduce t_2 as a parameter of U^\pm and v^\pm . Based on the fact that the convolved Green's and focusing functions in equations 3.6 and 3.7 are separated in time except for the first event in the convolved downgoing focusing function and last event in the convolved time-reversed downgoing Green's function in equation 3.7 (both of them are delta functions after the convolution) that coincide with each other. We rewrite equations 3.6 and 3.7 as

$$v^-(\mathbf{x}_0', \mathbf{x}_0'', t, t_2) = \int_{\partial D_0} d\mathbf{x}_0 \int_0^{+\infty} R(\mathbf{x}_0', \mathbf{x}_0, t') (\delta(t-t') \delta(\mathbf{x}_H'' - \mathbf{x}_H) + v_m^+(\mathbf{x}_0, \mathbf{x}_0'', t-t', t_2)) dt', \quad \text{for } \varepsilon < t < t_2 - \varepsilon \quad (3.10)$$

$$v_m^+(\mathbf{x}_0', \mathbf{x}_0'', t, t_2) = \int_{\partial D_0} d\mathbf{x}_0 \int_{-\infty}^0 R(\mathbf{x}_0', \mathbf{x}_0, -t') v^-(\mathbf{x}_0, \mathbf{x}_0'', t-t', t_2) dt', \quad \text{for } \varepsilon < t < t_2 - \varepsilon \quad (3.11)$$

where ε is a positive value to account for the finite bandwidth. Then we give equations 3.10 and 3.11 in the operator form as

$$v^-(\mathbf{x}_0', \mathbf{x}_0'', t, t_2) = (\Theta_\varepsilon^{t_2-\varepsilon} \mathbf{R} \delta + \Theta_\varepsilon^{t_2-\varepsilon} \mathbf{R} v_m^+)(\mathbf{x}_0', \mathbf{x}_0'', t, t_2), \quad (3.12)$$

$$v_m^+(\mathbf{x}_0', \mathbf{x}_0'', t, t_2) = (\Theta_\varepsilon^{t_2-\varepsilon} \mathbf{R}^* v^-)(\mathbf{x}_0', \mathbf{x}_0'', t, t_2), \quad (3.13)$$

where \mathbf{R} indicates a convolution integral operator of the measured data R with any wave field and \mathbf{R}^* a correlation integral operator. $\Theta_\varepsilon^{t_2-\varepsilon}$ is a time window to exclude values outside of the interval $(\varepsilon, t_2 - \varepsilon)$. Then we substitute equation 3.12 into equation 3.13 to give the final equation for v_m^+ as

$$(\mathbf{I} - \Theta_\varepsilon^{t_2-\varepsilon} \mathbf{R}^* \Theta_\varepsilon^{t_2-\varepsilon} \mathbf{R}) v_m^+(\mathbf{x}', \mathbf{x}'', t, t_2) = (\Theta_\varepsilon^{t_2-\varepsilon} \mathbf{R}^* \Theta_\varepsilon^{t_2-\varepsilon} \mathbf{R} \delta)(\mathbf{x}', \mathbf{x}'', t, t_2). \quad (3.14)$$

Following [Van der Neut and Wapenaar \(2016\)](#) we expand equation 3.14 as a Neumann series to give the equation as

$$v_m^+(\mathbf{x}', \mathbf{x}'', t, t_2) = \left[\sum_{k=1}^{\infty} (\Theta_\varepsilon^{t_2-\varepsilon} \mathbf{R}^* \Theta_\varepsilon^{t_2-\varepsilon} \mathbf{R})^k \delta \right] (\mathbf{x}', \mathbf{x}'', t, t_2). \quad (3.15)$$

We substitute equation 3.15 back into equation 3.6 to retrieve the projected U^- as

$$U^-(\mathbf{x}'', \mathbf{x}', t, t_2) = \Theta_{t_2-\varepsilon}^\infty R(\mathbf{x}'', \mathbf{x}', t) + \left[\sum_{k=1}^{\infty} \Theta_{t_2-\varepsilon}^\infty \mathbf{R} (\Theta_\varepsilon^{t_2-\varepsilon} \mathbf{R}^* \Theta_\varepsilon^{t_2-\varepsilon} \mathbf{R})^k \delta \right] (\mathbf{x}'', \mathbf{x}', t, t_2). \quad (3.16)$$

Equation 3.16 shows that U^- can be evaluated for a single pair of surface points at a single time instant, which means that the time window after the sum of repeated correlations and convolutions can be taken with constant values (ε and $t_2 - \varepsilon$) for each source-receiver pair instead of a curve line corresponding to a horizontal subsurface level as shown in [van der Neut and Wapenaar \(2016\)](#). Thus, the t_2 in equation 3.16 can be any desired time value within the time window of the measurement. It describes a fictitious focusing level in the subsurface. When the focusing level coincides with an actual subsurface reflector, the first event in U^- at time instant t_2 will be the primary reflection of that reflector with two-way travel time t_2 . Otherwise, the value in U^- at time instant t_2 will be zero. This means that U^- can be evaluated and its first event can be picked to represent a possible primary reflection event of the medium. We collect the value of U^- for each time instant t_2 and store it in a new function containing only primary reflections. We can write it as

$$R_t(\mathbf{x}'', \mathbf{x}', t = t_2) = R(\mathbf{x}'', \mathbf{x}', t_2) + \sum_{k=1}^{\infty} M_k(\mathbf{x}'', \mathbf{x}', t_2, t_2). \quad (3.17)$$

with

$$M_k(\mathbf{x}'', \mathbf{x}', t, t_2) = (\mathbf{R} \Theta_\varepsilon^{t_2-\varepsilon} \mathbf{R}^* \Theta_\varepsilon^{t_2-\varepsilon}) M_{k-1}(\mathbf{x}'', \mathbf{x}', t, t_2), \quad (3.18)$$

and

$$M_0 = R, \quad (3.19)$$

where R_t denotes the retrieved primary reflections and M_k with $k = 1, \dots, \infty$ give all orders of predicted internal multiple reflections. Equation 3.17 can be used to estimate R_t . As shown in equation 3.19, the processing can be performed with reflection response R as input only.

3.2.2 Examples

3.2.2.1 Horizontally layered example

In this subsection, we consider a model in which most reflectors are “invisible” to test the performance of the MME scheme. This model is a horizontally layered model with constant velocity (1000m/s) and constant layer thickness (100m); only the density in the different layers varies as shown in Figure 3.1. The values of density are given as: (1000, 2000, 300, 702, 412, 594, 457, 553, 481, 533, 494, 523, 501) kg/m^3 . The interesting point is that, because of the parameters of this model, the primary reflection of the third reflector cancels the first internal multiple reflection between the first two reflectors. The third reflector causes a new multiple, which is cancelled by the primary reflection from the fourth reflector, and so on. Hence, from the third reflector onward, the model is invisible in the reflection response. In this example, dipole sources and pressure receivers are positioned at the top of a model and a Ricker wavelet with 20Hz centre frequency is emitted by the sources. The spacing of the sources and receivers is 5m. The reflection response is modelled using a finite-difference scheme (Thorbecke and Draganov, 2011). Absorbing boundary conditions are applied around the model and the direct wave has been removed from the modelled data. One of the computed shot gathers convolved with the source wavelet is shown in Figure 3.2a. Note that indeed only the primary reflections from the first two reflectors are visible. Figure 3.2b shows the result retrieved by the MME scheme, which is also convolved with source wavelet. It is important to note that in the retrieved dataset primary reflections due to deeper reflectors are perfectly recovered because of the elimination of the corresponding internal multiple reflections. We pick the zero-offset and nonzero-offset (800m) traces from the original and retrieved datasets and show them in Figure 3.3. All traces have been normalized by the same factor. Displayed in Figure 3.3a are the zero-offset traces from the original shot gather (OR) and retrieved dataset (IR) shown in Figure 3.2. It can be seen that later arriving primary reflections have been successfully recovered. A similar conclusion can be derived from Figure 3.3b where the comparison of nonzero-offset traces is given.

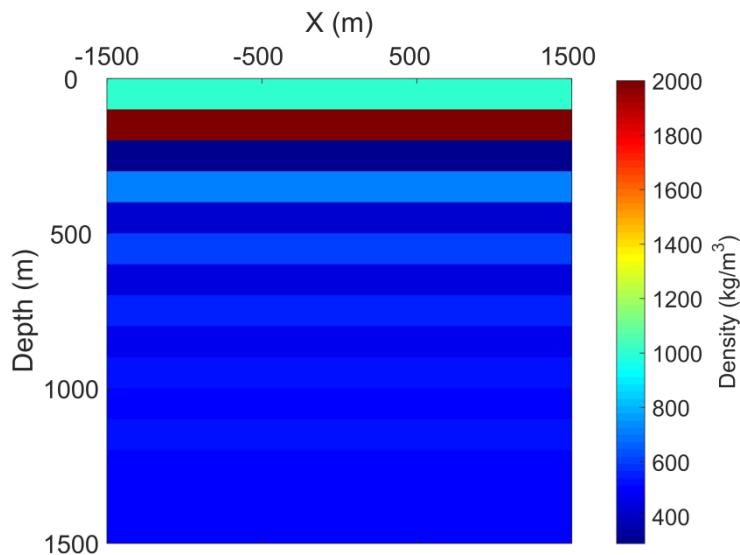


Figure 3.1: The density values of the “invisible” model.

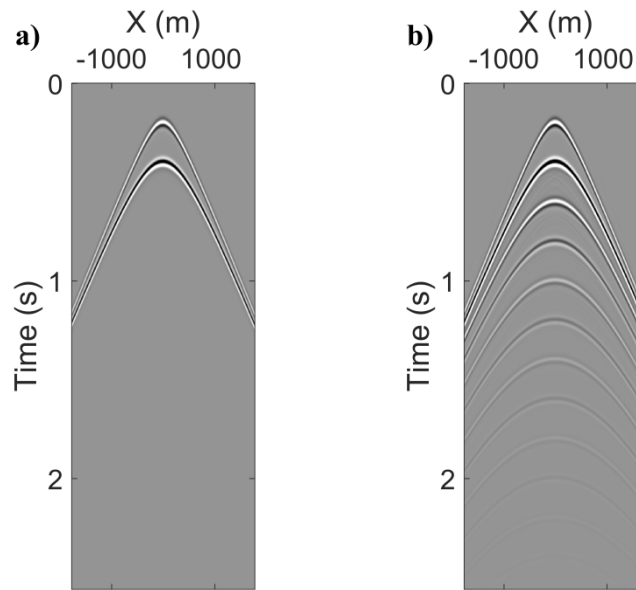


Figure 3.2: (a) The modelled shot gather and (b) the dataset retrieved by the MME scheme with $k = 1, \dots, 20$.

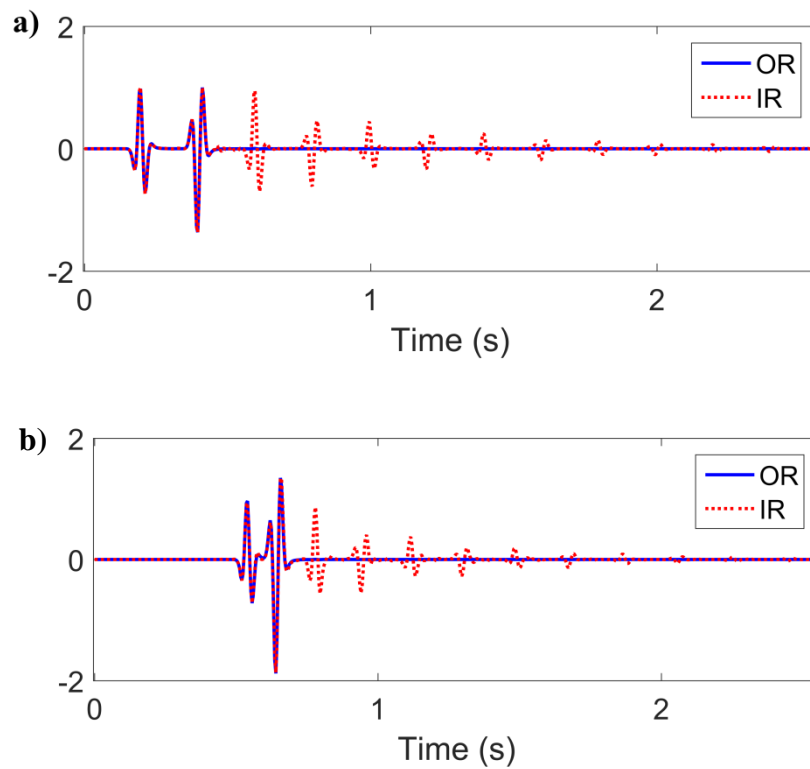
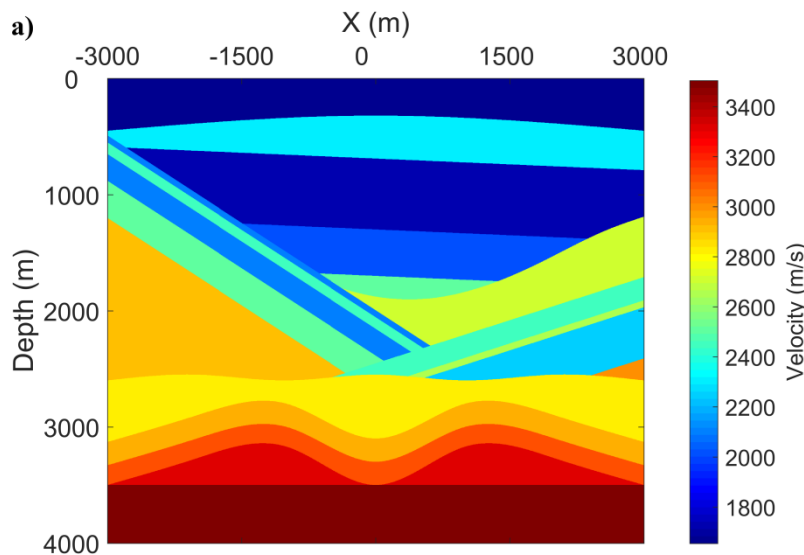


Figure 3.3: (a) The comparison of zero-offset traces from original and retrieved datasets shown in Figure 3.2, (b) the comparison of nonzero-offset (800m) traces from original and retrieved datasets shown in Figure 3.2.

3.2.2.2 Complex model example

Here, we use a complex 2D synthetic example to illustrate the MME method. Figure 3.4 shows the values for the acoustic velocity and density as functions of depth and horizontal position. We have computed the single-sided reflection responses with 601 dipole sources and 601 pressure receivers on a fixed spread with a spacing of 10 m at the top of the model. A Ricker wavelet with 20Hz centre frequency is emitted by the sources. Absorbing boundary conditions are applied around the model and the direct wave has been removed. One of the computed reflection responses convolved with the source wavelet is shown in Figure 3.5a. Note that internal multiple reflections are present and some of them are indicated by red arrows. The modelled reflection responses are used as inputs to solve equation 3.17 for R_l . Figure 3.5b shows the retrieved dataset with $k = 1, \dots, 20$. Note that internal multiple reflections present in Figure 3.5a have been eliminated in Figure 3.5b. Figure 3.6 gives the comparison of zero-offset and nonzero-offset (1000) traces from the original gather (Figure 3.5a) and eliminated gather (Figure 3.5b), the blue solid line (OR) in Figure 3.6 indicates the traces from the original gather and red dotted line (IR) indicates the traces from the eliminated gather (all traces have been normalized by the same factor). It shows that internal multiple reflections have been removed and primary reflections well preserved after this processing. We use the original and retrieved datasets as inputs to image the medium. The images retrieved by a one-way wave equation migration scheme are shown in Figures 3.7a and 3.7b. The image in Figure 3.7a contains artefacts arising from multiple scatterings because they are imaged as if they were primary reflections. However, the image in Figure 3.7b, which is obtained from the retrieved dataset, is nearly perfect without ghost images due to internal multiple reflections.



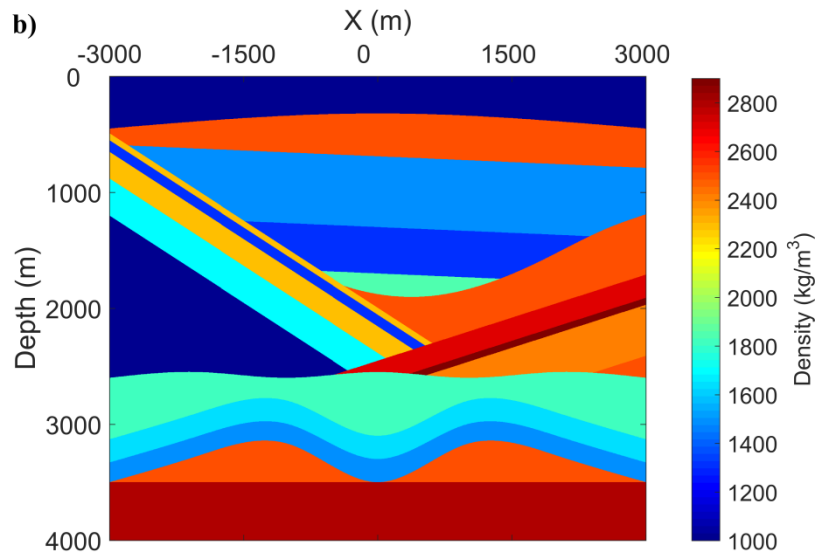


Figure 3.4: (a) The velocity and (b) density values of the complex model.

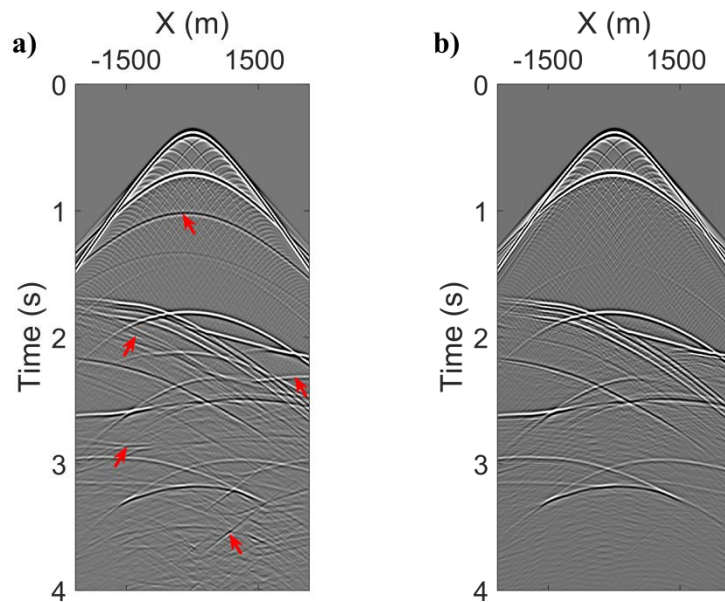


Figure 3.5: (a) Modelled shot gather and (b) the dataset retrieved by the MME scheme with $k = 1, \dots, 20$. Red arrows indicate internal multiple reflections.

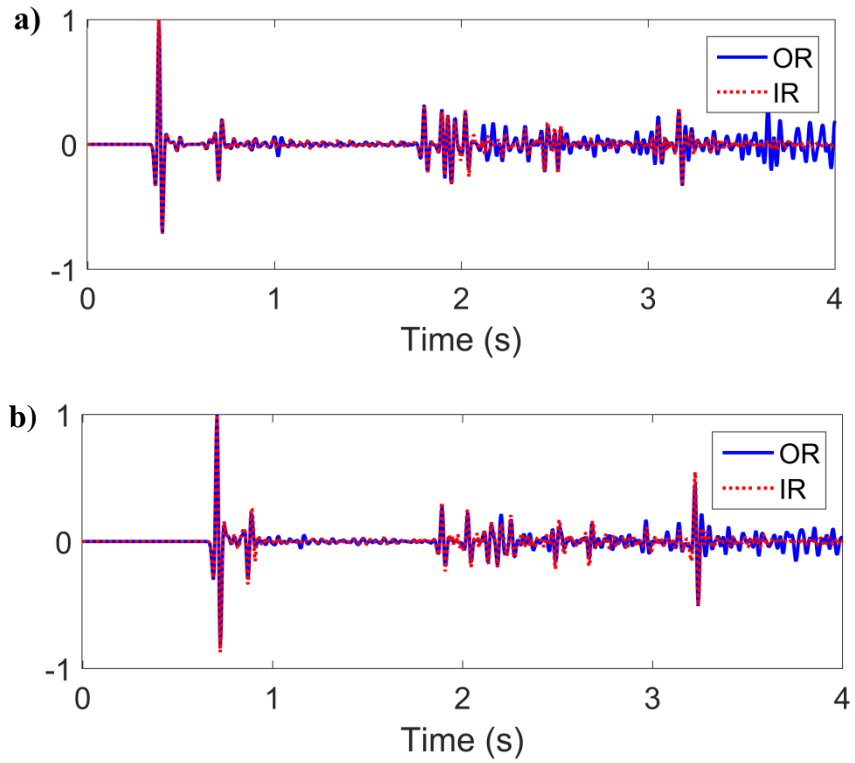
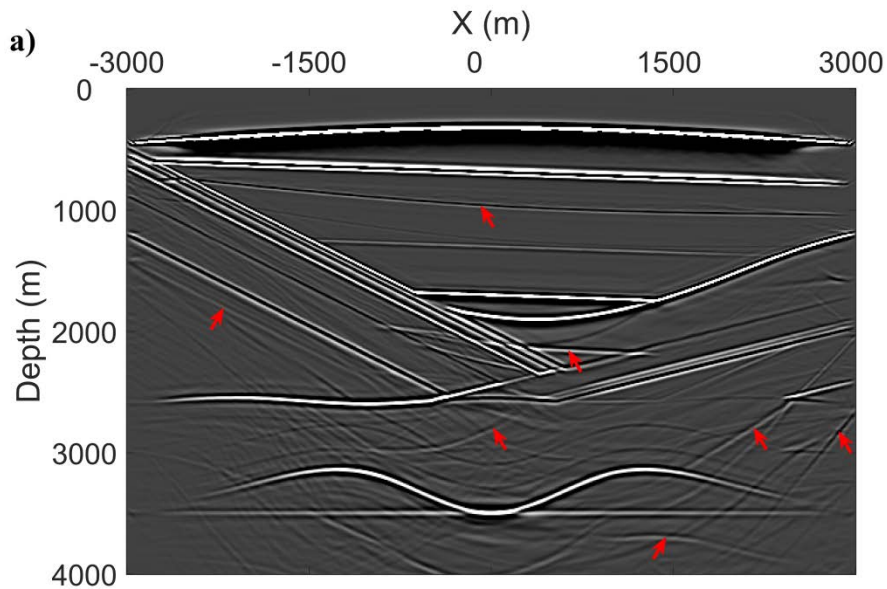


Figure 3.6: (a) The comparison of zero-offset traces from original and retrieved datasets shown in Figure 3.5, (b) the comparison of nonzero-offset (1000m) traces from original and retrieved datasets shown in Figure 3.5.



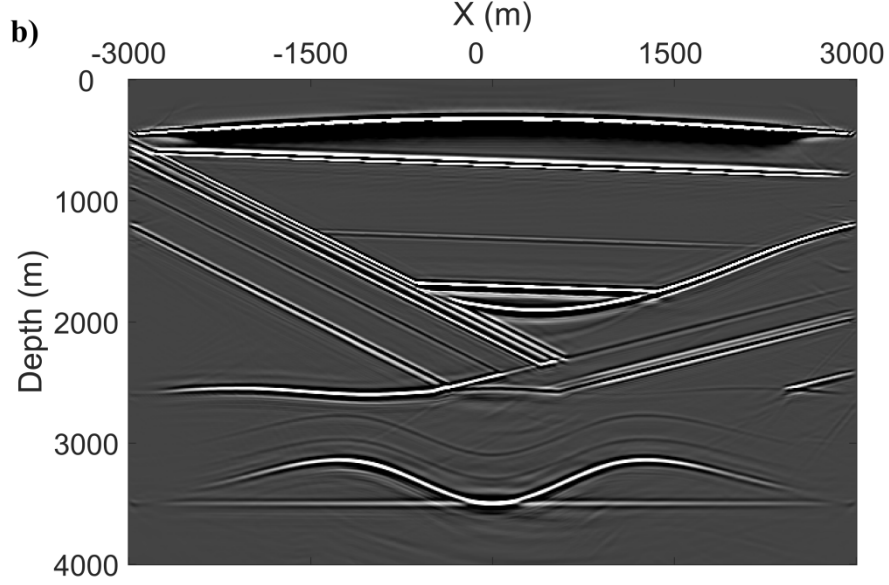


Figure 3.7: (a) The image retrieved from the modelled reflection responses and (b) the image retrieved from the resulting dataset of MME scheme. Red arrows indicate artefacts due to internal multiple reflections.

3.3 Transmission compensated Marchenko multiple elimination (T-MME)

3.3.1 Theory

In this subsection we derive the modified Marchenko equations from single-sided Green's function representations and, similar to the MME scheme, project the focusing wavefield from an arbitrary depth level back to the acquisition surface, such that the process takes place entirely in the data domain. Based on projected equations we show how the transmission compensated primary reflection from the focusing depth level is present as the last event in the projected focusing wavefield. We continue by presenting the scheme of iterative internal multiple reflection elimination such that only the primary reflections with compensation for transmission effects are retained in the retrieved dataset.

We start with the single-sided Green's function representations given in equations 3.1 and 3.2 and rewrite them with the help of equation 3.3 to yield

$$f_1^-(\mathbf{x}'_0, \mathbf{x}_i, t) = \int_{\partial D_0} d\mathbf{x}_0 \int_0^{+\infty} R(\mathbf{x}'_0, \mathbf{x}_0, t') f_1^+(\mathbf{x}_0, \mathbf{x}_i, t-t') dt', \quad \text{for } -t_d + \varepsilon < t < t_d + \varepsilon \quad (3.20)$$

$$f_{1m}^+(\mathbf{x}'_0, \mathbf{x}_i, t) = \int_{\partial D_0} d\mathbf{x}_0 \int_{-\infty}^0 R(\mathbf{x}'_0, \mathbf{x}_0, -t') f_1^-(\mathbf{x}_0, \mathbf{x}_i, t-t') dt', \quad \text{for } -t_d + \varepsilon < t < t_d + \varepsilon \quad (3.21)$$

The time truncation operator in equations 3.20 and 3.21 is asymmetric and different from the regular Marchenko scheme ($-t_d + \varepsilon < t < t_d - \varepsilon$). This can be justified as follows. As shown in Figure 3.8, the f_1^- and G^- will be the same as in the regular case when the focusing point

is far from a specific reflector. When the focusing point is close to the reflector (relative to the size of the wavelet), because of the resolution problem a choice has to be made. One should either regard the reflection of this reflector as belonging to f_1^- or G^- . In [Slob et al. \(2014\)](#) and [Wapenaar et al. \(2014a\)](#), the choice is made to put it in G^- and that means the reflection event is moved to f_1^- only when the focusing point is more than half a wavelet below the reflector. Here we choose the opposite: the reflection is put in f_1^- as soon as the focusing point is within half a wavelet above the reflector. The fact that this choice has to be, and can be, made is due to the finite frequency bandwidth of the wavelet.

Similar to equation 3.5, we convolve both sides of equations 3.20 and 3.21 with T_d to find

$$v^-(\mathbf{x}'_0, \mathbf{x}''_0, t, t_2) = \int_{\partial\mathbf{D}_0} d\mathbf{x}_0 \int_0^{+\infty} R(\mathbf{x}'_0, \mathbf{x}_0, t') (\delta(t-t') \delta(\mathbf{x}''_0 - \mathbf{x}_H) + v_m^+(\mathbf{x}_0, \mathbf{x}''_0, t-t', t_2)) dt',$$

for $\varepsilon < t < t_2 + \varepsilon$ (3.22)

$$v_m^+(\mathbf{x}'_0, \mathbf{x}''_0, t, t_2) = \int_{\partial\mathbf{D}_0} d\mathbf{x}_0 \int_{-\infty}^0 R(\mathbf{x}'_0, \mathbf{x}_0, -t') v^-(\mathbf{x}_0, \mathbf{x}''_0, t-t', t_2) dt',$$

for $\varepsilon < t < t_2 + \varepsilon$ (3.23)

with v^- and v_m^+ defined in equations 3.8 and 3.9. Note that, similar to the MME scheme, with this step the requirement of the estimation of the initial downgoing focusing function has been removed because f_{1d}^+ has collapsed to be a delta function after convolution with T_d . The physical explanation of v^- can be given as follows.

[Wapenaar et al. \(2014b\)](#) give the relationship between two types of focusing functions as

$$f_1^+(\mathbf{x}'_0, \mathbf{x}_i, t) = f_2^-(\mathbf{x}_i, \mathbf{x}'_0, t), \quad (3.24)$$

$$-f_1^-(\mathbf{x}'_0, \mathbf{x}_i, -t) = f_2^+(\mathbf{x}_i, \mathbf{x}'_0, t), \quad (3.25)$$

where f_2 is a focusing function with its focal point at the acquisition surface. The relationship between f_2^+ and f_2^- can be given as ([Wapenaar et al., 2014a](#))

$$f_2^+(\mathbf{x}_i, \mathbf{x}'_0, t) = \int_{\partial\mathbf{D}_i} d\mathbf{x}'_i \int_0^{+\infty} R^\cap(\mathbf{x}_i, \mathbf{x}'_i, t'') f_2^-(\mathbf{x}'_i, \mathbf{x}'_0, t-t'') dt'', \quad (3.26)$$

where $R^\cap(\mathbf{x}_i, \mathbf{x}'_i, t)$ is the reflection response of the truncated medium from below, with sources and receivers at $\partial\mathbf{D}_i$. Then, we rewrite equation 3.8 with the help of equations 3.24, 3.25 and 3.26 as

$$v^-(\mathbf{x}'_0, \mathbf{x}''_0, t, t_2) = - \int_{\partial\mathbf{D}_i} d\mathbf{x}_i \int_0^{+\infty} T_d(\mathbf{x}_i, \mathbf{x}''_0, t') \int_{\partial\mathbf{D}_i} d\mathbf{x}'_i \int_0^{+\infty} R^\cap(\mathbf{x}_i, \mathbf{x}'_i, t'') T^{inv}(\mathbf{x}'_i, \mathbf{x}'_0, -t+t'-t'') dt'' dt', \quad (3.27)$$

where T^{inv} is the inverse of T and note that f_1^+ is the inverse of T as given by [Wapenaar et al. \(2014b\)](#). The last event in v^- is constructed by taking the first event in R^\cap and the direct event in T^{inv} , hence the last event in v^- can be given as

$$v_{last}^-(\mathbf{x}'_0, \mathbf{x}''_0, t, t_2) = - \int_{\partial \mathbf{D}_i} d\mathbf{x}_i \int_0^{+\infty} T_d(\mathbf{x}_i, \mathbf{x}''_0, t') \int_{\partial \mathbf{D}_i} d\mathbf{x}'_i \int_0^{+\infty} R_{first}^\cap(\mathbf{x}_i, \mathbf{x}'_i, t'') T_d^{inv}(\mathbf{x}'_i, \mathbf{x}'_0, -t + t' - t'') dt'' dt', \quad (3.28)$$

where R_{first}^\cap indicates the first event in R^\cap , v_{last}^- indicates the last event in v^- and T_d^{inv} indicates the direct event in T^{inv} .

Figure 3.9 gives the ray path of v_{last}^- . This is the reflection response with compensation for the transmission effects. Note that the amplitudes in T_d and T_d^{inv} only fully cancel each other when the medium is horizontally layered. It follows that the last event in v^- is the transmission loss compensated primary reflection of the reflector above $\partial \mathbf{D}_i$ when its two-way travel time is t_2 . Note that the reflection coefficient contained in R^\cap is opposite to the reflection coefficient in R , which compensates for the minus sign in equations 3.27 and 3.28. This means that v^- can be evaluated and its value at t_2 can be taken to represent a possible primary reflection event of the medium without transmission losses. Note that in the regular Marchenko scheme with symmetric time truncation this event will be the first event without transmission effect compensation in the upgoing part of the projected Green's function ([van der Neut and Wapenaar, 2016](#)).

Next, we give equations 3.22 and 3.23 in operator form as

$$v^-(\mathbf{x}'_0, \mathbf{x}''_0, t, t_2) = (\Theta_\varepsilon^{t_2+\varepsilon} R + \Theta_\varepsilon^{t_2+\varepsilon} \mathbf{R} v_m^+)(\mathbf{x}'_0, \mathbf{x}''_0, t, t_2), \quad (3.29)$$

$$v_m^+(\mathbf{x}'_0, \mathbf{x}''_0, t, t_2) = (\Theta_\varepsilon^{t_2+\varepsilon} \mathbf{R}^* v^-)(\mathbf{x}'_0, \mathbf{x}''_0, t, t_2), \quad (3.30)$$

The time window $\Theta_\varepsilon^{t_2+\varepsilon}$ excludes values outside of the interval $(\varepsilon, t_2 + \varepsilon)$. We substitute equation 3.30 into equation 3.29 to get the final equation for v^- as

$$(I - \Theta_\varepsilon^{t_2+\varepsilon} \mathbf{R} \Theta_\varepsilon^{t_2+\varepsilon} \mathbf{R}^*) v^-(\mathbf{x}'_0, \mathbf{x}''_0, t, t_2) = \Theta_\varepsilon^{t_2+\varepsilon} R(\mathbf{x}'_0, \mathbf{x}''_0, t). \quad (3.31)$$

Similar to the MME scheme, we expand equation 3.31 as a Neumann series to give the equation as

$$v^-(\mathbf{x}'_0, \mathbf{x}''_0, t, t_2) = \Theta_\varepsilon^{t_2+\varepsilon} R(\mathbf{x}'_0, \mathbf{x}''_0, t) + \left[\sum_{k=1}^{\infty} (\Theta_\varepsilon^{t_2+\varepsilon} \mathbf{R} \Theta_\varepsilon^{t_2+\varepsilon} \mathbf{R}^*)^k \Theta_\varepsilon^{t_2+\varepsilon} R \right] (\mathbf{x}'_0, \mathbf{x}''_0, t, t_2). \quad (3.32)$$

Equation 3.32 is valid for each common shot gather with a single source at \mathbf{x}''_0 and all receivers at \mathbf{x}'_0 . The time window after the sum of repeated correlations and convolutions can also be taken with constant values (ε and $t_2 + \varepsilon$) for all traces. Similar to MME, the t_2 in equation 3.32 can be any desired time value within the time window of the measurement. We collect the value of v^- at each time instant t_2 and store it in a new function containing only transmission compensated primary reflections. We can write it as

$$R_r(\mathbf{x}'_0, \mathbf{x}''_0, t = t_2) = R(\mathbf{x}'_0, \mathbf{x}''_0, t_2) + \sum_{k=1}^{\infty} \bar{M}_k(\mathbf{x}'_0, \mathbf{x}''_0, t_2, t_2). \quad (3.33)$$

with

$$\bar{M}_k(\mathbf{x}'_0, \mathbf{x}''_0, t, t_2) = (\Theta_{\varepsilon}^{t_2+\varepsilon} \mathbf{R} \Theta_{\varepsilon}^{t_2+\varepsilon} \mathbf{R}^*) \bar{M}_{k-1}(\mathbf{x}'_0, \mathbf{x}''_0, t, t_2), \quad (3.34)$$

and

$$\bar{M}_0 = R, \quad (3.35)$$

where R_r denotes the transmission compensated primary reflections and \bar{M}_k with $k = 1, \dots, \infty$ predict internal multiple reflections and transmission losses in the primary reflections. Equation 3.33 can be evaluated to obtain R_r . The retrieved dataset R_r contains only transmission compensated primary reflections. Based on the retrieved dataset R_r , a better velocity model can be built and clearer image of the subsurface can be obtained. Also, better AVA/AVO analysis can be done.

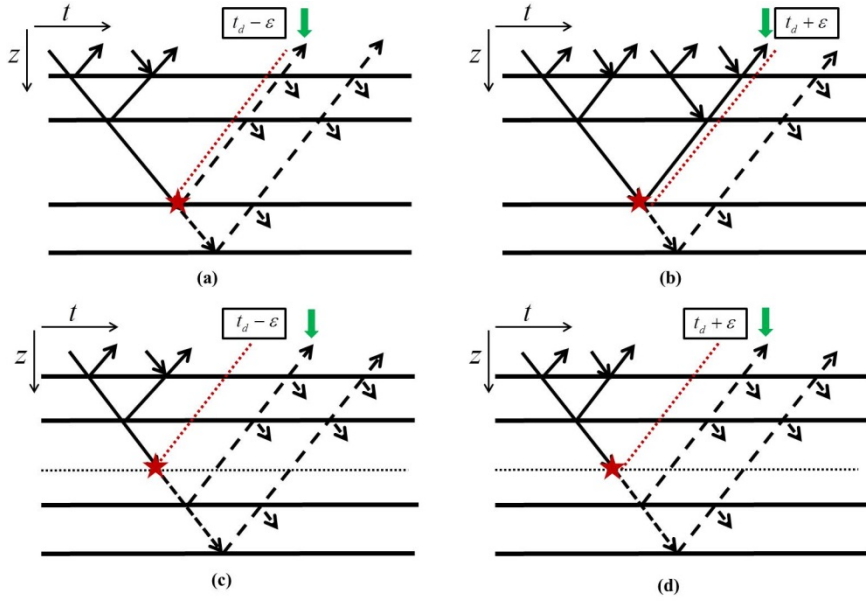


Figure 3.8: (a) 1D sketch of f_1 and G^- in equation 3.1 with the focusing point just above the third reflector with regular time truncation operator $(-t_d + \varepsilon, t_d - \varepsilon)$; (b) the f_1 and G^- in equation 3.1 with revised asymmetric time truncation operator $(-t_d + \varepsilon, t_d + \varepsilon)$; (c) 1D sketch of f_1 and G^- in equation 3.1 with the focusing point far from reflectors with regular time truncation operator $(-t_d + \varepsilon, t_d - \varepsilon)$; (d) the f_1 and G^- in equation 3.1 with revised asymmetric time truncation operator $(-t_d + \varepsilon, t_d + \varepsilon)$. The dotted horizontal line in (c) and (d) indicate the focusing level. In each plot the red star indicates the focusing point, the green arrow indicates the reflection event of the third reflector and the red dashed line indicates the right side of the regular or revised time truncation operator, the black dashed arrow-lines indicate G^- and black solid arrow-lines indicate f_1 .

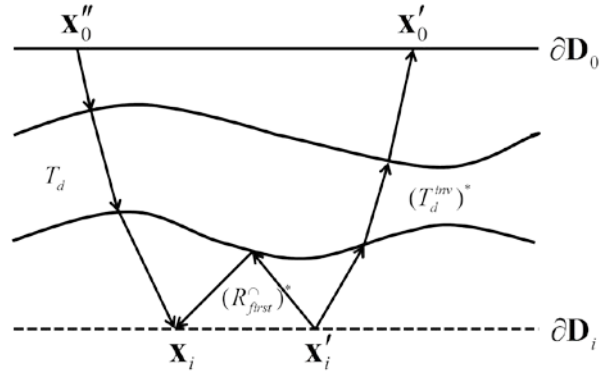


Figure 3.9: Ray path of v_{last}^- , (*) indicates the time reversed version. Note that the dashed line at ∂D_i denotes the depth level (not a reflector) along which the integration in equation 3.28 takes place.

3.3.2 Examples

In this subsection, the same synthetic examples as shown in section 3.2 are used to test the performance of the T-MME scheme.

3.3.2.1 Horizontally layered example

The same “invisible” model given in Figure 3.1 is used here. One of the computed shot gathers convolved with the source wavelet is shown in Figure 3.10a and the result obtained with T-MME scheme is shown in Figure 3.10b. Similarly, in the dataset retrieved by T-MME scheme primary reflections due to deeper reflectors are perfectly recovered because of the elimination of the corresponding internal multiple reflections. Figure 3.10c gives the modelled primary reflections without transmission loss, which is convolved with the source wavelet and will be used as a reference to illustrate the success of the T-MME scheme for transmission loss compensation in primary reflections. We pick the zero-offset and nonzero-offset (800m) traces from the modelled primary reflections and retrieved dataset and show them in Figure 3.11. All traces have been normalized by the same factor. Displayed in Figure 3.11a are the zero-offset traces from the modelled primary reflections (MD) shown in Figure 3.10c and retrieved dataset (IT) shown in Figure 3.10b. Note that the retrieved data by T-MME scheme match well with the modelled primary reflections without transmission loss (quantitatively, around four percent errors occur in the amplitude of the retrieved primary reflections). A similar conclusion can be derived from Figure 3.11b where the comparison of nonzero-offset (800m) traces is given.

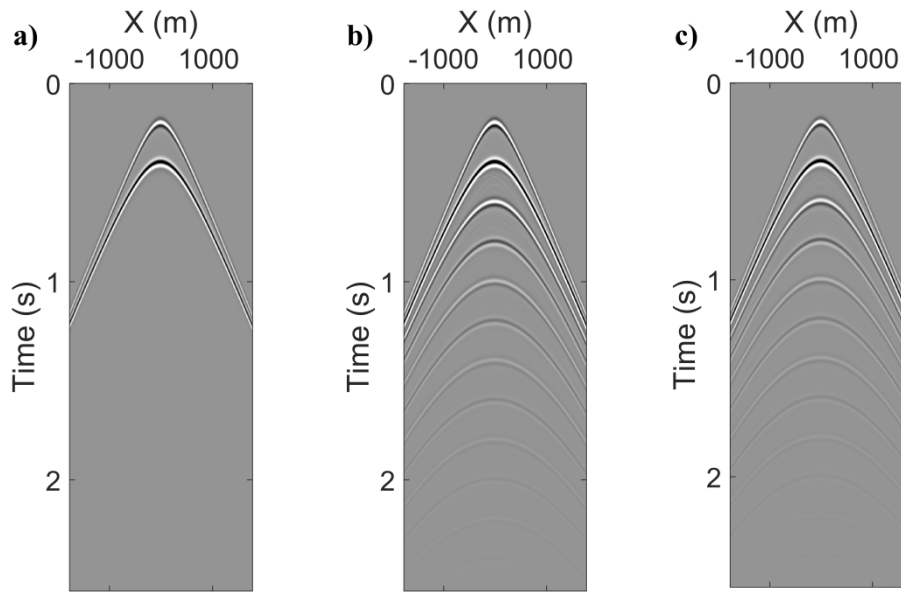


Figure 3.10: (a) The modelled shot gather, (b) the dataset retrieved by the T-MME scheme with $k = 1, \dots, 20$ and (c) the modelled primary reflections without transmission losses.

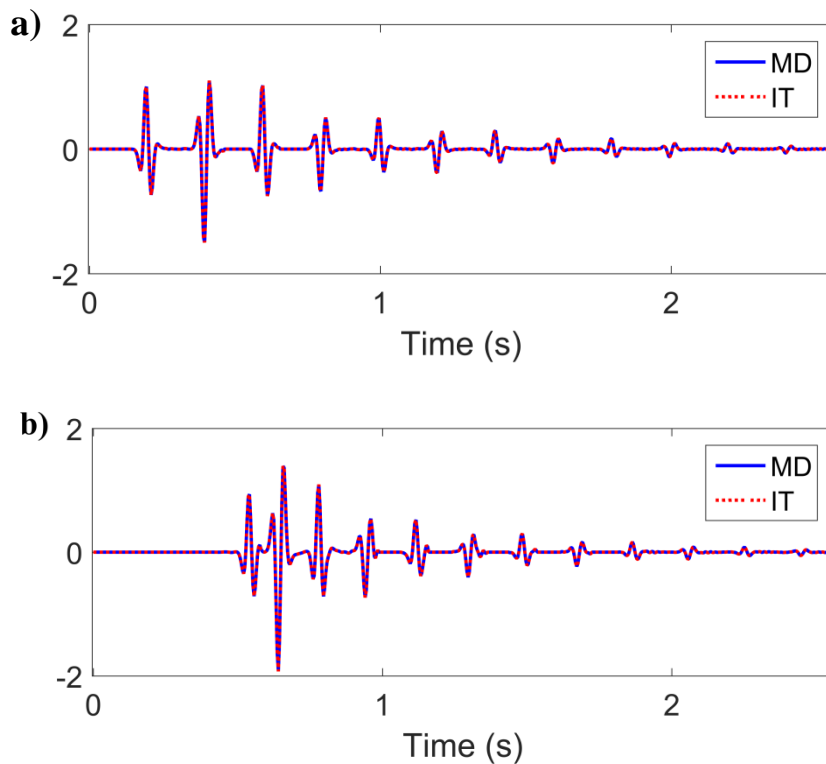


Figure 3.11: (a) The comparison of zero-offset traces from modelled primary reflections and retrieved dataset shown in Figures 3.10b and 3.10c, (b) the comparison of nonzero-offset (800m) traces from modelled primary reflections and retrieved dataset shown in Figures 3.10b and 3.10c.

3.3.2.2 Complex example

The same complex model given in Figure 3.4 is used here. One of the computed shot gathers convolved with the source wavelet is shown in Figure 3.12a. Internal multiple reflections are present at later arrival times and some of them are indicated by red arrows. The computed reflection responses are used as inputs to solve equation 3.33. The resulting dataset convolved with the source wavelet is shown in Figure 3.12b. The retrieved dataset is nearly multiple-free. Detailed comparisons of amplitudes using zero-offset and nonzero-offset traces are given in Figure 3.13. All traces have been normalized by the same normalization factor. It can be seen in Figure 3.13a that the T-MME scheme eliminates internal multiple reflections and compensates for transmission losses in primary reflections. A similar conclusion can be derived from Figure 3.13b where the comparison of nonzero-offset (1000) traces is given.

We use the computed and retrieved datasets to image the medium. The images obtained using a one-way wave equation migration scheme are shown in Figure 3.14. We can see that, in the image retrieved from the computed reflection responses, artefacts arising from internal multiple reflections are present. The image retrieved from the resulting dataset of T-MME clearly show the primary reflectors without strong artefacts due to internal multiple reflections.

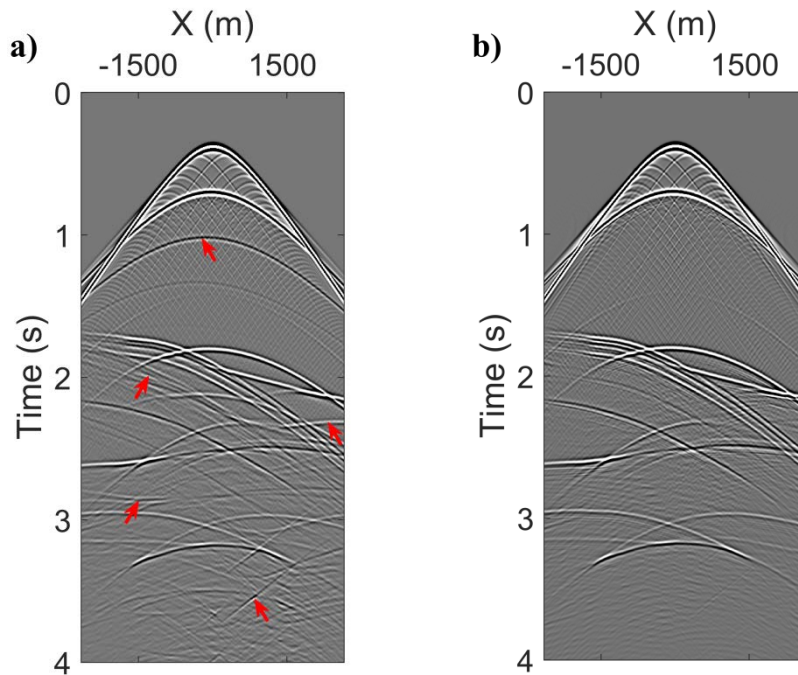


Figure 3.12: (a) Modelled shot gather and (b) the dataset retrieved by the T-MME scheme with $k = 1, \dots, 20$. Red arrows indicate the internal multiple reflections.

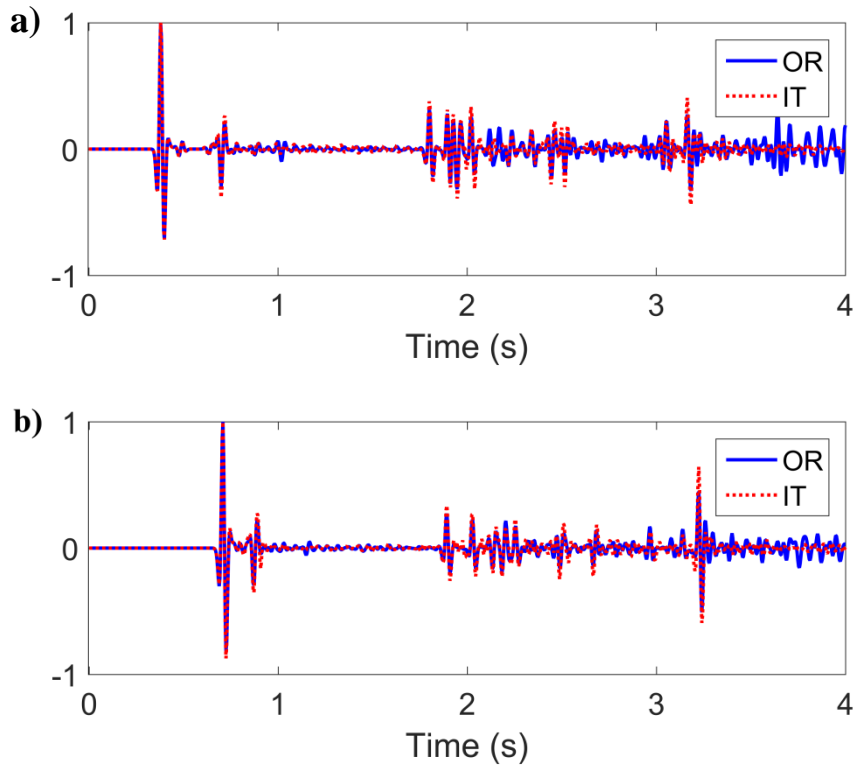
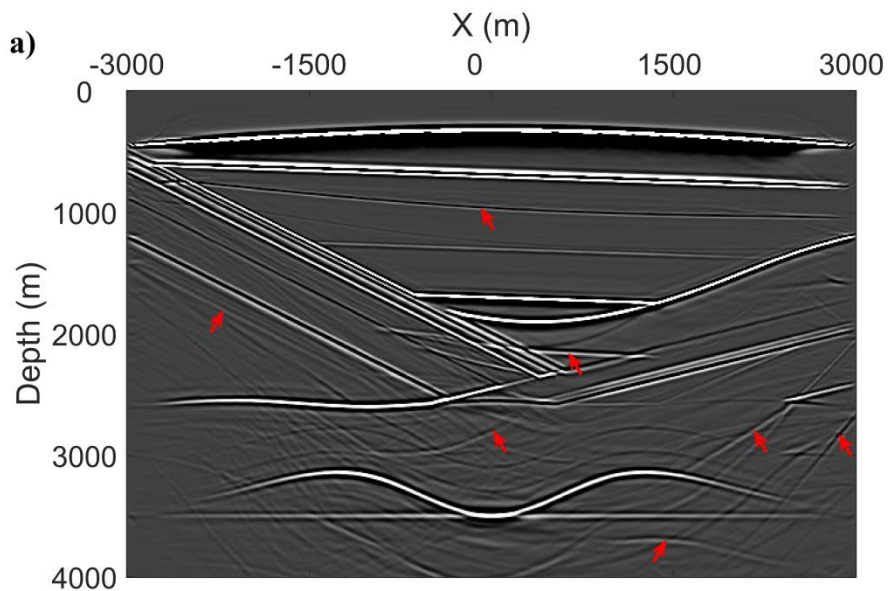


Figure 3.13: (a) The comparison of zero-offset traces from original and retrieved datasets shown in Figure 3.12, (b) the comparison of nonzero-offset (1000m) traces from original and retrieved datasets shown in Figure 3.12. OR indicates traces from Figure 3.12a and IT indicates traces from Figure 3.12b.



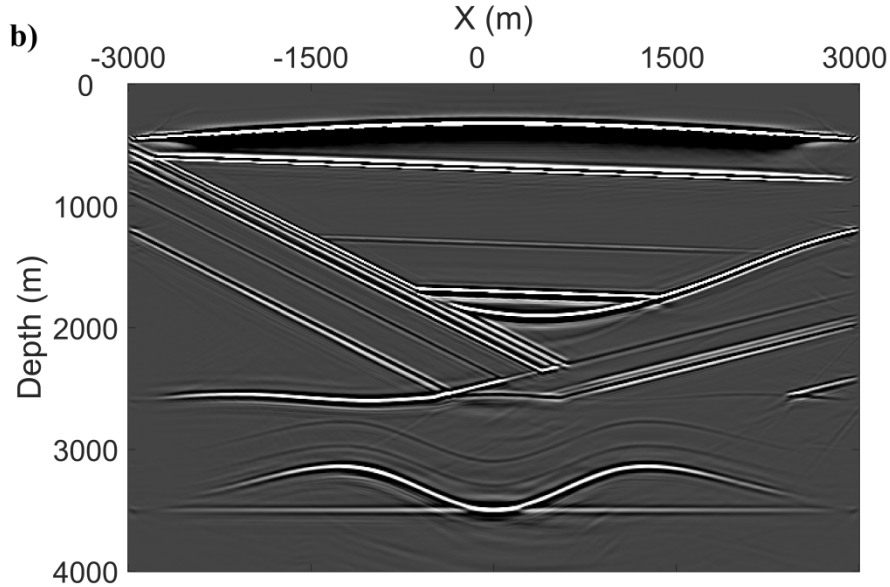


Figure 3.14: (a) The image retrieved from the computed reflection responses and (b) the image retrieved from the resulting dataset of T-MME. Red arrows indicate artefacts due to internal multiple reflections.

3.4 Limitation analysis

In the derivation of both methods, we assumed a lossless medium. These methods can be adapted to work with two-sided reflection and transmission data in dissipative media (Slob, 2016). We further assumed that the Green's functions and the focusing functions can be separated in time, that the source time signature can be well recovered and deconvolved and we ignored evanescent waves (Wapenaar et al., 2013). In this section, the effect of limited bandwidth is analysed with a thin layer model. We also investigate the effects of refracted and scattered waves in the data, which are not accounted for by the underlying theory. Because the MME and T-MME schemes share the same basic theory, they suffer from the same limitations. In this section, we test the performance of T-MME scheme to explore the limitations. In the following examples, the dipole source emits a Ricker wavelet with 20 Hz centre frequency and the single-sided reflection responses with 401 sources and 401 pressure receivers with a spacing of 10 m at the top of the models have been computed. Absorbing boundary conditions are applied around the model and the direct wave has been removed.

3.4.1 Thin layer example

In this subsection, we compute synthetic data in a simple horizontally layered thin layer model to test the performance of the T-MME scheme. Figure 3.15 shows the values for the acoustic velocity and density of this model. The thickness of the thin layer is 30 meters (the wavelength at the centre frequency of the source time signature is 90 meters). One of the computed single-sided reflection responses convolved with the source wavelet is shown in

Figure 3.16a. Note that internal multiple reflections occur in the computed response. The computed reflection responses are used as inputs to solve equation 3.33 for $R_r(\mathbf{x}'_0, \mathbf{x}''_0, t)$ with $k = 1, \dots, 20$ and one of the retrieved datasets convolved with the source wavelet is shown in Figure 3.16b. The comparison of zero-offset traces from datasets shown in Figures 3.16a and 3.16b is given in Figure 3.17. Please note that the mismatch happens in Figure 3.17. In the discussion section we will analyse this mismatch in detail.

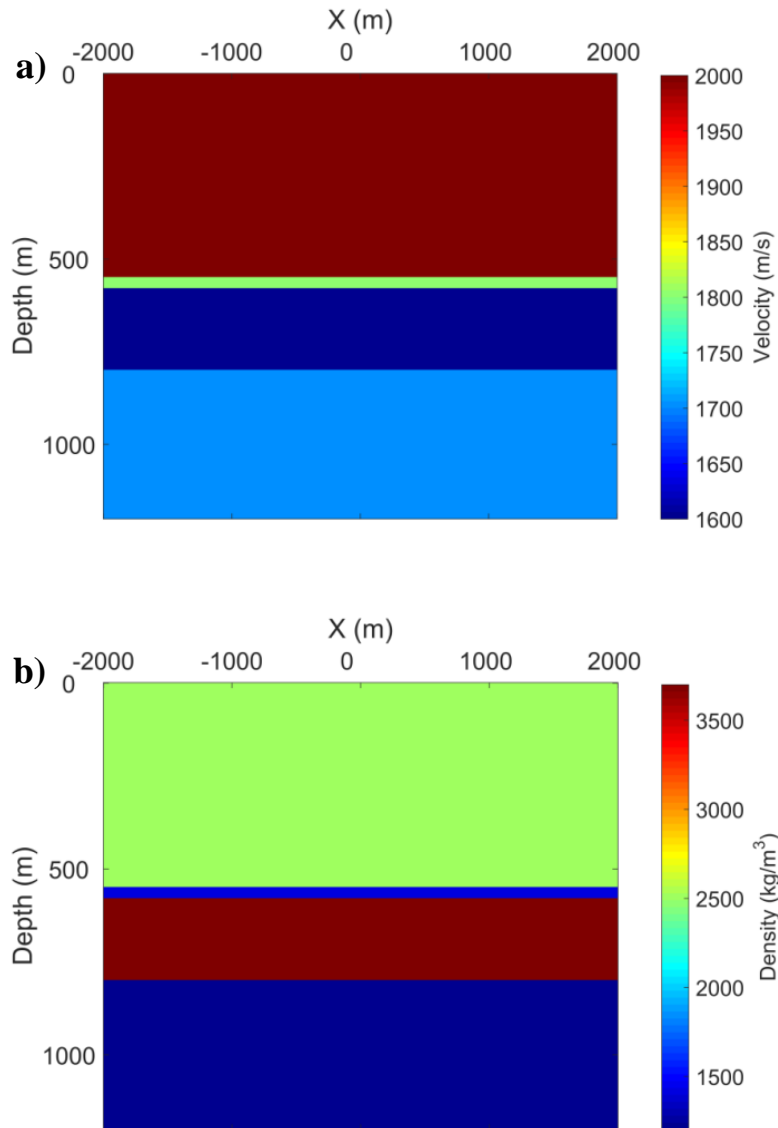


Figure 3.15: (a) The velocity and (b) density values of the model.

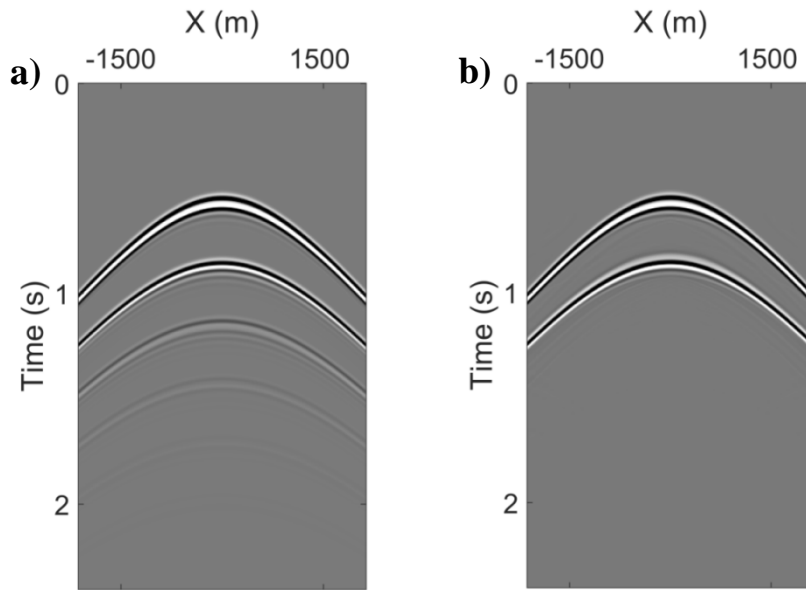


Figure 3.16: (a) The modelled reflection response and (b) the retrieved dataset by the T-MME scheme.

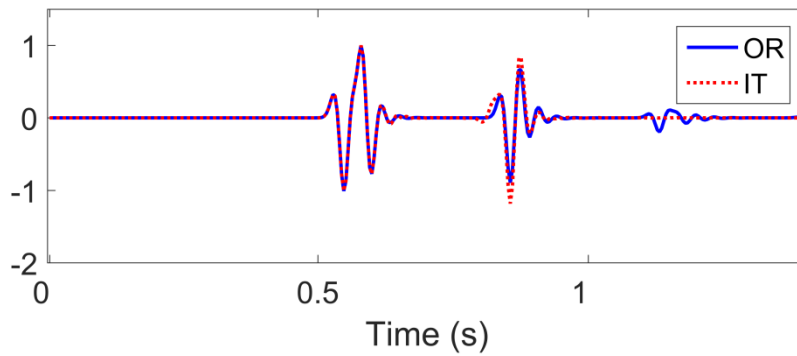


Figure 3.17: The comparison of zero-offset traces from original and retrieved datasets, the blue solid line (OR) indicates the zero-offset trace from original gather and red dotted line (IT) indicates the zero-offset trace from retrieved dataset (both traces have been normalized by the same normalization factor).

3.4.2 Refracted wave example

In this subsection, we compute synthetic data in a horizontally layered model with a high velocity layer that generates refracted waves, to test the performance of the T-MME scheme. Figure 3.18 shows the values for the acoustic velocity of this model (constant density 1200kg/m^3). One of the computed single-sided reflection responses convolved with the source wavelet is shown in Figure 3.19a. Note that internal multiple reflections occur in the computed response and the red arrows indicate the refracted wave. The computed reflection responses are used as inputs to solve equation 3.33 for $R_r(\mathbf{x}'_0, \mathbf{x}''_0, t)$ with $k = 1, \dots, 20$ and the retrieved dataset convolved with the source wavelet is shown in Figure 3.19b. Note that internal multiple reflections visible in Figure 3.19a have disappeared, whereas the refracted

wave has been well preserved and new events (artefacts), which are not present in Figure 3.19a, have clearly appeared in Figure 3.19b. The T-MME scheme did not process the refracted waves correctly and constructed ghost events.

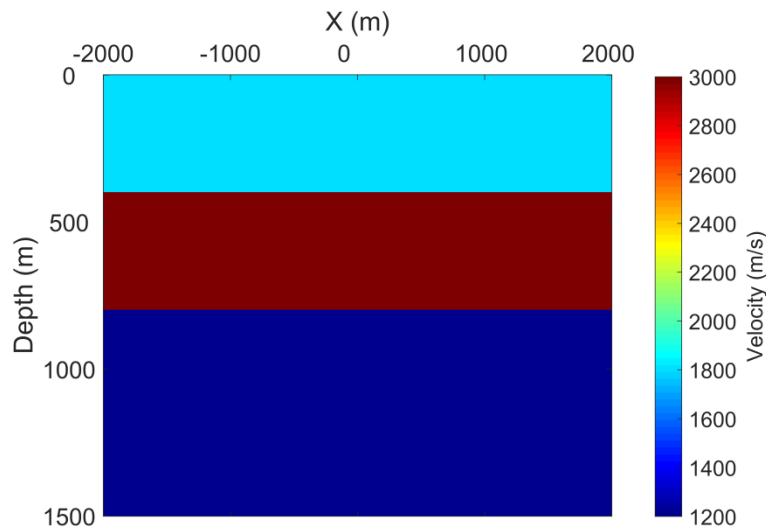


Figure 3.18: Velocity values of the model.

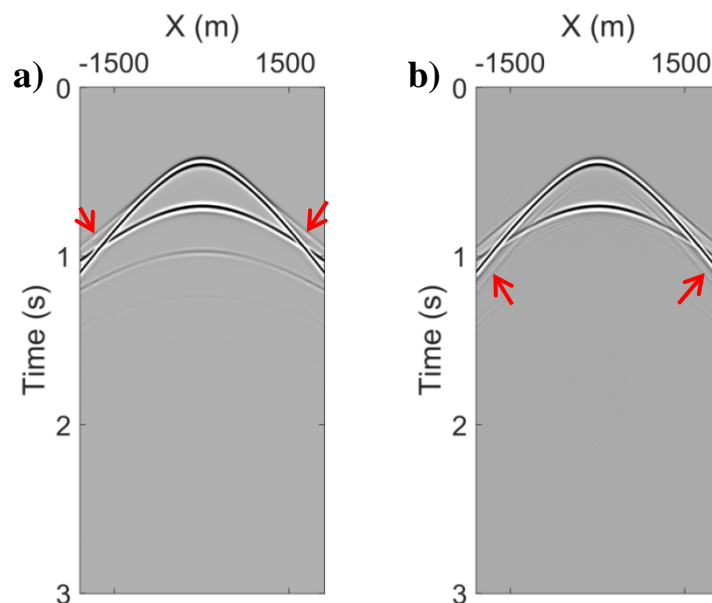


Figure 3.19: (a) The modelled reflection response and (b) the retrieved dataset by the T-MME scheme. Red arrows in (a) indicate refracted waves and red arrows in (b) indicate generated artefactual events.

3.4.3 Scattered wave example

In this subsection, we compute the synthetic data in a model that contains a point scatter to test the performance of the current scheme when scattered waves are present. Figure 3.20 shows the values for the acoustic velocity and density of the model. The yellow star indicates the

position of the scattering point. One of the computed single-sided reflection responses convolved with the source wavelet is shown in Figure 3.21a. Note that scattered waves occur as indicated by red arrows. The computed reflection responses are used as inputs to solve equation 3.33 for $R_r(\mathbf{x}'_0, \mathbf{x}''_0, t)$ with $k = 1, \dots, 20$ and one of the retrieved datasets convolved with the source wavelet is shown in Figure 3.21b. It can be seen that the internal multiple reflection indicated by the yellow arrow in Figure 3.21a has been partially suppressed, whereas the multiple scattered waves are still present in Figure 3.21b.

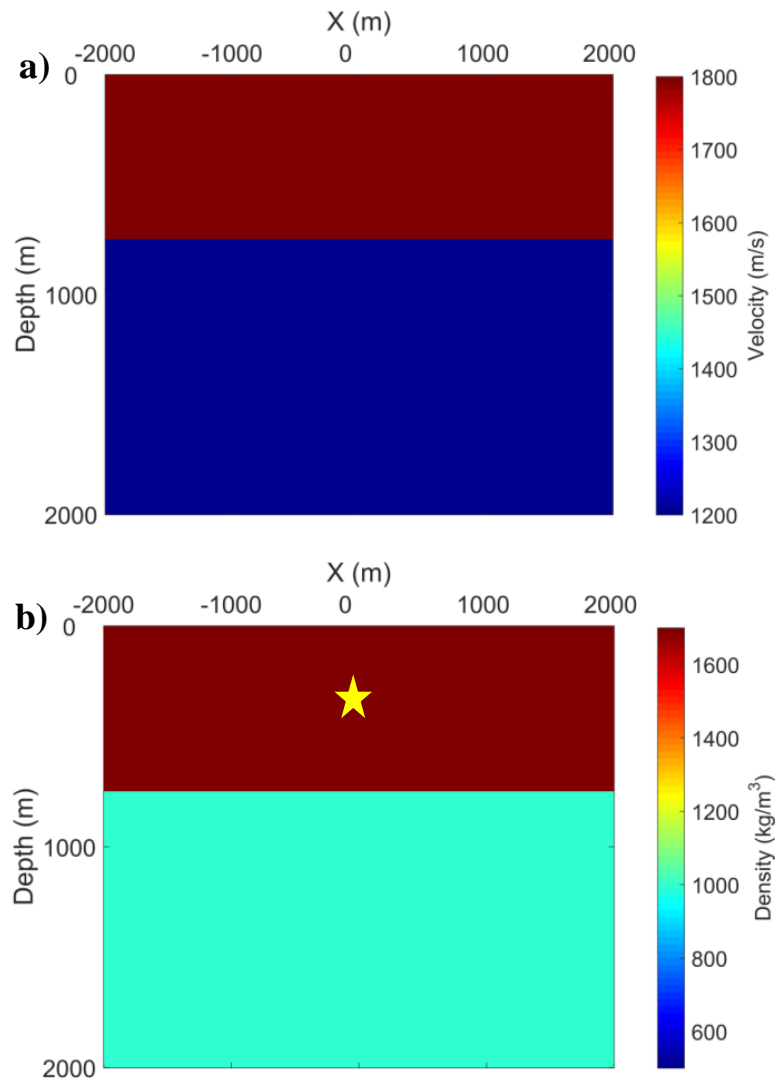


Figure 3.20: (a) The velocity and (b) density values of the model. Yellow star indicates the position of the point scatter.

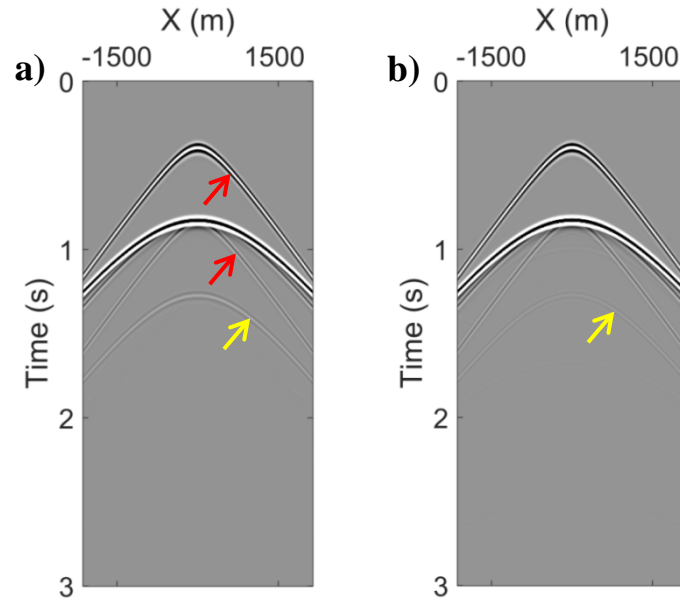


Figure 3.21: (a) The modelled reflection response and (b) the retrieved dataset by the T-MME scheme. Red arrows indicate scattered waves and yellow arrows indicate internal multiple reflections.

3.5 Discussion

In the subsection of the thin layer example, Figure 3.17 shows that the thin layer is treated as a single reflector with more complicated behaviour. For this reason, the primary reflection of the lower boundary in the thin layer is not touched for transmission losses compensation and internal multiple reflections inside it are kept by the T-MME scheme. That is why the primary reflection from the second reflector (it is the third reflector, but we observe the thin layer as a single reflector with complicated behaviour) still has the imprint of the thin layer as shown in Figure 3.17. However, the amplitude of the primary reflection from the second reflector has been improved because of the compensation of transmission losses and the internal multiple reflections of this reflector and the thin layer have been successfully removed. This example shows that the effect of limited bandwidth on thin layer responses cannot be accounted for by the T-MME scheme, but the associated internal multiple reflections between other reflectors and the thin layer are properly eliminated.

In the subsection of the refracted wave example, the refracted wave indicated by red arrows in Figure 3.19a is well preserved in Figure 3.19b after the processing because the underlying theory of the T-MME scheme does not account for it. The underlying theory assumes that all events are reflection events and associated internal multiple reflections are predicted and subtracted. Unfortunately, the multiple reflections related to refracted waves do not exist in the data and this leads to new events in Figure 3.19b with the same move-out as primary reflections at far-offsets but that disappear at near zero-offsets. Using the event indicated by the red arrows in Figure 3.19b as an example, this event disappears at near zero-offsets where the refracted wave is not present in the data and no false multiple reflections are predicted.

We observe that the presence of refracted waves in the data cannot be well accounted for during the processing and artificial events are generated in the retrieved dataset.

In the subsection of the scattered wave example, the scattered waves indicated by red arrows are preserved in Figure 3.21b after the processing. The internal multiple reflection indicated by the yellow arrow in Figure 3.21a has been partially suppressed after the processing as is shown in Figure 3.21b. The partial suppression is caused by the fact that, in order to completely remove the internal multiple reflection, the data should be recorded for larger offsets than used in this example.

Except for the assumptions listed in the first paragraph of the limitation analysis section, some extra limitations would affect the application of the T-MME scheme in a field dataset, such as: incomplete deconvolution of the source wavelet and the presence of noise in the dataset. In both cases, the predicted internal multiple reflections and transmission losses do not have the correct amplitude and phase, thus internal multiple reflections cannot be completely removed and transmission losses cannot be completely compensated for.

3.6 Conclusions

We have derived two schemes for internal multiple reflection elimination without model information or adaptive subtraction. The MME scheme focuses only on internal multiple reflection elimination without touching the primary reflections, while the T-MME scheme removes all orders of internal multiple reflections and compensates for transmission losses in primary reflections. The layered and complex synthetic examples validate the success of both schemes. The following examples explore the limitations of the T-MME scheme and show that scattered waves, refracted waves and thin layer effects are partially beyond the capability of the T-MME scheme. All limitations of the T-MME scheme are shared with MME scheme. We expect that both methods can be used in seismic reflection imaging and monitoring of structures and processes in the Earth's interior. These methods open a new way to investigate how independent information about the internal structure of a medium is contained in measured acoustic reflection data. It also allows to investigate how this information can be retrieved without having information about the medium, and how it can be used to produce an accurate image.

References

- Berkhout, A. J., and D. J. Verschuur, 2005, Removal of internal multiples with the common focus-point (CFP) approach. Part 1: Explanation of the theory: *Geophysics*, **70**, no. 3, V45–V60.
- de Melo, F. X., M. Idris, Z. J. Wu, and C. Kostov, 2014, Cascaded internal multiple attenuation with inverse scattering series: 84th Annual Meeting, SEG, Expanded Abstracts, 4113–4117.

- Hadidi, M. T., and D. J. Verschuur, 1997, Removal of internal multiples: Field data examples: 59th Annual Meeting, EAGE, Extended Abstracts.
- Kelamis, P. G., W. Zhu, K. O. Rufai, and Y. Luo, 2006, Land multiple attenuation: The future is bright: 76th Annual Meeting, SEG, Expanded Abstracts, 2699–2703.
- Löer, K., A. Curtis, and G. A. Meles, 2016, Relating source-receiver interferometry to an inverse-scattering series to derive a new method to estimate internal multiples: *Geophysics*, **81**, no. 3, Q27–Q40.
- Luo, Y., P. G. Kelamis, S. Huo, G. Sindi, S. Hsu, and A. B. Weglein, 2011, Elimination of land internal multiples based on the inverse scattering series: *The Leading Edge*, **30**, 884–889.
- Matson, K., D. Corrigan, A. Weglein, C. Young, and P. Carvalho, 1999, Inverse scattering internal multiple attenuation: Results from complex synthetic and field data examples: 89th Annual Meeting, SEG, Expanded Abstracts, 1060–1063.
- Meles, G., K. Löer, M. Ravais, A. Curtis, and C. A. da Costa Filho, 2015, Internal multiple prediction and removal using Marchenko autofocusing and seismic interferometry: *Geophysics*, **80**, no. 1, A7–A11.
- Slob, E., K. Wapenaar, F. Broggini, and R. Snieder, 2014, Seismic reflector imaging using internal multiples with Marchenko-type equations: *Geophysics*, **79**, no. 2, S63–S76.
- Slob, E., 2016, Green's function retrieval and Marchenko imaging in a dissipative acoustic medium: *Physical Review Letters*, **116**, 164301.
- Staring, M., R. Pereira, H. Douma, J. van der Neut, and K. Wapenaar, 2018, Source-receiver Marchenko redatuming on field data using an adaptive double-focusing method: *Geophysics*, **83**, no. 6, S570–S590.
- Ten Kroode, P. E., 2002, Prediction of internal multiples: *Wave Motion*, **35**, 315–338.
- Thorbecke, J. W., and D. Draganov, 2011, Finite-difference modeling experiments for seismic interferometry: *Geophysics*, **76**, no. 6, H1–H18.
- Van Borselen, R. G., 2002, Fast-track, data-driven interbed multiple removal: A North Sea data example: 64th Annual Meeting, EAGE, Extended Abstracts.
- van der Neut, J., and K. Wapenaar, 2016, Adaptive overburden elimination with the multidimensional Marchenko equation: *Geophysics*, **81**, no. 5, T265–T284.
- Wapenaar, K., F. Broggini, E. Slob, and R. Snieder, 2013, Three-dimensional single-sided Marchenko inverse scattering, data-driven focusing, Green's function retrieval, and their mutual relations: *Physical Review Letters*, **110**, 084301.
- Wapenaar, K., J. Thorbecke, J. van der Neut, F. Broggini, E. Slob, and R. Snieder, 2014a, Green's function retrieval from reflection data, in absence of a receiver at the virtual source position: *Journal of the Acoustical Society of America*, **135**, 2847–2861.
- Wapenaar, K., J. Thorbecke, J. van der Neut, F. Broggini, E. Slob, and R. Snieder, 2014b, Marchenko imaging: *Geophysics*, **79**, no. 3, WA39–WA57.

Weglein, A. B., F. A. Gasparotto, P. M. Carvalho, and R. H. Stolt, 1997, An inverse scattering series method for attenuating multiples in seismic reflection data: *Geophysics*, **62**, 1975–1989.

4

Extension of MME and T-MME schemes to account for free-surface related multiple reflections

We extend the MME and T-MME schemes to account for free-surface related multiple reflections. Thus, the extended MME and T-MME schemes can remove free-surface and internal multiple reflections in one step, while the amplitudes of retrieved primary reflections by the extended T-MME scheme is compensated for transmission losses. Both extended schemes do not require model information or adaptive subtraction. They consist only of the reflection response as a correlation and convolution operator that acts on an intermediate wavefield from which we compute and capture the primary reflections. For each time instant we keep one value for each source-receiver pair and store it in a new dataset. A conventional migration scheme can then be used to compute an artefact-free image of the medium. We evaluated the success of both methods with 2D synthetic examples.

4.1 Introduction

Except for internal multiple reflections, the free-surface related multiple reflections also cause major ghost reflectors in the migration image. Several schemes have been developed to eliminate the free-surface related multiple reflections. The surface-related multiple elimination (SRME) scheme of [Verschuur et al. \(1992\)](#) is a good example. SRME consists of two steps: free-surface related multiple reflection prediction and subtraction. In the first step, free-surface related multiple reflections are predicted by convolution of the traces in the measured data. Because the source wavelet is not known exactly, the predicted events differ from actual events in the measured data. Hence, adaptive subtraction is required to subtract the predicted free-surface related multiple reflections from the measured data in the second step. Unfortunately, adaptive subtraction has two major problems. One is that only an overall amplitude correction is carried out. The other is that the energy is minimized which leads to removal of primary reflections when primary and free-surface related multiple reflections overlap in time, which happens quite often in field data. The estimation of primaries by sparse inversion (EPSI) ([van Groenestijn and Verschuur, 2009](#)) replaces the two-step processing of SRME, prediction and adaptive subtraction, by a full-waveform inversion process. Both the SRME and EPSI have achieved success for synthetic and field datasets ([Lopez and Verschuur, 2015](#)) and been widely accepted as robust tools for free-surface related multiple reflection attenuation in industry. Our aim is to find a way to remove free-surface and internal multiple reflections from the measured dataset in one step without model information or adaptive filtering.

In this chapter, we extend the MME and T-MME schemes to account for free-surface related multiple reflections. For both extended schemes, only the single-sided reflection response is required as input and the output contains only primary reflections (the output of extended MME scheme contains only physical primary reflections and the output of extended T-MME scheme contains only transmission compensated primary reflections). The chapter is organized as follows. In the first part, we show how the extended MME scheme can be derived by starting with the revised Marchenko equations presented by [Singh et al. \(2017\)](#). In the second part, we show how the extended T-MME scheme can be derived from the revised Marchenko equations presented by [Singh et al. \(2017\)](#) with a modified truncation operator. Synthetic examples follow to show how well both schemes eliminate the free-surface and internal multiple reflections from the computed single-sided reflection response, and also transmission compensation by the T-MME scheme. The limitations of both schemes are discussed and we end with conclusions.

4.2 Extended MME scheme

4.2.1 Theory

We indicate time as t and the position vector of a spatial location as $\mathbf{x} = (x, y, z)$, where z denotes depth and (x, y) denote the horizontal coordinates. The pressure free surface $\partial\mathbf{D}_0$ is defined as $z_0 = 0$. For convenience, the coordinates at $\partial\mathbf{D}_0$ are denoted as $\mathbf{x}_0 = (\mathbf{x}_H, z_0)$, with $\mathbf{x}_H = (x, y)$. Similarly, the position vector of a point at an arbitrary depth level $\partial\mathbf{D}_i$ is denoted as $\mathbf{x}_i = (\mathbf{x}_H, z_i)$, where z_i denotes the depth level of $\partial\mathbf{D}_i$. The vertical axis points down and we have $z_0 < z_i$. We express the acoustic impulse reflection response as $R(\mathbf{x}'_0, \mathbf{x}_0, t)$, where \mathbf{x}_0 denotes the source position and \mathbf{x}'_0 denotes the receiver position, both located at the free surface $\partial\mathbf{D}_0$. The Green's function $G(\mathbf{x}_i, \mathbf{x}_0, t)$ is defined for an impulsive source that is excited at \mathbf{x}_0 and a receiver is positioned at the focal point \mathbf{x}_i . The Green's function is defined in the same physical medium as the measured single-sided reflection response. We define the truncated medium as $z_0 < z < z_i$ in the same way as [Wapenaar et al. \(2014\)](#). Inside the truncated domain, the properties of the medium are equal to the properties of the physical medium. Outside the truncated domain, the truncated medium is reflection-free. The focusing wave field $f_1(\mathbf{x}_0, \mathbf{x}_i, t)$ is the solution of the homogeneous wave equation in the truncated medium and focuses at the focal point \mathbf{x}_i at $t = 0$. The focusing and Green's functions can be partitioned into up- and downgoing constituents and for this we use pressure-normalized quantities.

We start with the 3D versions of the Green's function representations in the presence of a free surface at the acquisition level z_0 ([Singh et al., 2017](#)),

$$G^-(\mathbf{x}_i, \mathbf{x}'_0, t) = \int_{\partial\mathbf{D}_0} d\mathbf{x}_0 \int_0^{+\infty} [R(\mathbf{x}'_0, \mathbf{x}_0, t') f_1^+(\mathbf{x}_0, \mathbf{x}_i, t - t') - rR(\mathbf{x}'_0, \mathbf{x}_0, t') f_1^-(\mathbf{x}_0, \mathbf{x}_i, t - t')] dt' - f_1^-(\mathbf{x}'_0, \mathbf{x}_i, t), \quad (4.1)$$

$$G^+(\mathbf{x}_i, \mathbf{x}'_0, -t) = - \int_{\partial\mathbf{D}_0} d\mathbf{x}_0 \int_{-\infty}^0 [R(\mathbf{x}'_0, \mathbf{x}_0, -t') f_1^-(\mathbf{x}_0, \mathbf{x}_i, t - t') - rR(\mathbf{x}'_0, \mathbf{x}_0, -t') f_1^+(\mathbf{x}_0, \mathbf{x}_i, t - t')] dt' + f_1^+(\mathbf{x}'_0, \mathbf{x}_i, t). \quad (4.2)$$

Superscripts $+$ and $-$ indicate downgoing and upgoing fields, respectively. The reflection coefficient of the free surface is denoted r . Note that the measured dataset R in this chapter is different from it in chapters 2 and 3 because of presence of free-surface related multiple reflections. Similar to equation 3.5, we convolve both sides of equations 4.1 and 4.2 with T_d to project focusing functions back to acquisition surface. The equations can be given as

$$U^-(\mathbf{x}''_0, \mathbf{x}'_0, t, t_2) = R(\mathbf{x}'_0, \mathbf{x}''_0, t) + \int_{\partial\mathbf{D}_0} d\mathbf{x}_0 \int_0^{+\infty} [R(\mathbf{x}'_0, \mathbf{x}_0, t') v_m^+(\mathbf{x}_0, \mathbf{x}''_0, t - t', t_2) - rR(\mathbf{x}'_0, \mathbf{x}_0, t') v^-(\mathbf{x}_0, \mathbf{x}''_0, t - t', t_2)] dt' - v^-(\mathbf{x}'_0, \mathbf{x}''_0, t, t_2), \quad (4.3)$$

$$\begin{aligned}
 U^+(\mathbf{x}_0'', \mathbf{x}_0', -t, t_2) &= rR(\mathbf{x}_0', \mathbf{x}_0'', -t) - \int_{\partial \mathbf{D}_0} d\mathbf{x}_0 \int_{-\infty}^0 [R(\mathbf{x}_0', \mathbf{x}_0, -t')v^-(\mathbf{x}_0, \mathbf{x}_0'', t-t', t_2) \\
 &\quad - rR(\mathbf{x}_0', \mathbf{x}_0, -t')v_m^+(\mathbf{x}_0, \mathbf{x}_0'', t-t', t_2)]dt' + \delta(t)\delta(\mathbf{x}_H'' - \mathbf{x}_H') + v_m^+(\mathbf{x}_0', \mathbf{x}_0'', t, t_2),
 \end{aligned} \tag{4.4}$$

with U^\mp defined as

$$U^\mp(\mathbf{x}_0'', \mathbf{x}_0', \pm t, t_2) = \int_{\partial \mathbf{D}_i} d\mathbf{x}_i \int_0^{+\infty} T_d^+(\mathbf{x}_i, \mathbf{x}_0'', t')G^\mp(\mathbf{x}_i, \mathbf{x}_0', \pm(t-t'))dt', \tag{4.5}$$

and v^- and v_m^+ are projected versions of f_1^- and f_{1m}^+ as shown in equations 3.8 and 3.9, t_2 denotes the minimum two-way travel time from a surface point \mathbf{x}_0' to the focusing level z_i and back to the surface point \mathbf{x}_0'' , $\delta(\mathbf{x}_H)$ is a spatially band-limited 2D delta function in space and $\delta(t)$ is a delta function in time (T_d is the inverse of f_{1d}^+ in the sense that it collapses f_{1d}^+ to a delta function in horizontal coordinates and time). Because the projected Green's and focusing functions in equations 4.3 and 4.4 are assumed to be separated in time except for one time instant (van der Neut and Wapenaar, 2016), we limit the time window in which we evaluate equations 4.3 and 4.4 and end up with

$$\begin{aligned}
 v^-(\mathbf{x}_0', \mathbf{x}_0'', t, t_2) &= R(\mathbf{x}_0', \mathbf{x}_0'', t) + \int_{\partial \mathbf{D}_0} d\mathbf{x}_0 \int_0^{+\infty} [R(\mathbf{x}_0', \mathbf{x}_0, t')v_m^+(\mathbf{x}_0, \mathbf{x}_0'', t-t', t_2) \\
 &\quad - rR(\mathbf{x}_0', \mathbf{x}_0, t')v^-(\mathbf{x}_0, \mathbf{x}_0'', t-t', t_2)]dt',
 \end{aligned} \tag{4.6}$$

for $\varepsilon < t < t_2 - \varepsilon$

$$\begin{aligned}
 v_m^+(\mathbf{x}_0', \mathbf{x}_0'', t, t_2) &= \int_{\partial \mathbf{D}_0} d\mathbf{x}_0 \int_{-\infty}^0 [R(\mathbf{x}_0', \mathbf{x}_0, -t')v^-(\mathbf{x}_0, \mathbf{x}_0'', t-t', t_2) \\
 &\quad - rR(\mathbf{x}_0', \mathbf{x}_0, -t')v_m^+(\mathbf{x}_0, \mathbf{x}_0'', t-t', t_2)]dt',
 \end{aligned} \tag{4.7}$$

for $\varepsilon < t < t_2 - \varepsilon$

where ε is a small positive value. These two equations can be seen as the projected version of the revised Marchenko equations for single-sided reflection response with free-surface related multiple reflections presented by Singh et al. (2017). These two equations can be solved for v^- and v_m^+ using only the single-sided reflection response (the f_{1d}^+ collapses to a delta function in the projected version such that no model information is required). The obtained v^- and v_m^+ from equations 4.6 and 4.7 can be used to compute U^- from equation 4.3 as

$$\begin{aligned}
 U^-(\mathbf{x}_0'', \mathbf{x}_0', t, t_2) &= R(\mathbf{x}_0'', \mathbf{x}_0', t) + \int_{\partial \mathbf{D}_0} d\mathbf{x}_0 \int_0^{+\infty} [R(\mathbf{x}_0', \mathbf{x}_0, t')v_m^+(\mathbf{x}_0, \mathbf{x}_0'', t-t', t_2) \\
 &\quad - rR(\mathbf{x}_0', \mathbf{x}_0, t')v^-(\mathbf{x}_0, \mathbf{x}_0'', t-t', t_2)]dt',
 \end{aligned} \tag{4.8}$$

for $t_2 - \varepsilon \leq t < +\infty$

The explanation of U^- can be given as follows. When the focusing point is at, but just above, an actual reflector as shown in Figure 4.1a, the Green's function in equation 4.1 is the upgoing field at the surface generated by an impulsive source at the focusing point. The reflection from that reflector will be the first event in G^- . By convolving this Green's function with T_d^+ as given by equation 4.5, we have redatumed all focusing points at $\partial \mathbf{D}_i$

back to a location at the surface to obtain U^- . The first event in U^- indicated by red arrow in Figure 4.1b has two-way travel time t_2 and is the primary reflection of the reflector below our original focusing level. When the focusing point is far from a reflector, the value in U^- with two-way travel time t_2 (indicated by green arrow in Figure 4.1d) is zero and the first event in U^- (indicated by red arrow in Figure 4.1d) has longer two-way travel time than t_2 . Similar to MME and T-MME schemes in chapter 3, t_2 can be taken with constant values for each source-receiver pair instead of a curve line corresponding to a horizontal subsurface level. Thus, the t_2 in equation 4.8 can be any desired time value within the time window of the measurement. The t_2 describes a fictitious focusing level in the subsurface where we have focused to and projected back from. When the focusing level coincides with an actual subsurface reflector, the first event in U^- at time instant t_2 will be the primary reflection of that reflector with two-way travel time t_2 . Otherwise, the value in U^- at time instant t_2 will be zero. This means that U^- can be evaluated and its first event can be picked to represent a possible primary reflection event of the medium. We collect the value of U^- for each time instant t_2 and store it in a new function containing only primary reflections. We can write it as

$$R_t(\mathbf{x}_0'', \mathbf{x}_0', t = t_2) = U^-(\mathbf{x}_0'', \mathbf{x}_0', t_2, t_2). \quad (4.9)$$

where R_t denotes the retrieved primary reflections.

Equation 4.9 indicates that only primary reflections end up in R_t . Note that the free-surface and internal multiple reflections are removed in one step, where no model information or adaptive subtraction is required.

4.2.2 Example

The aim of the extended MME method is to retrieve the primary reflections by removing the free-surface and internal multiple reflections in one step given the measured single-sided reflection response at the pressure free surface. A 2D synthetic example is given to illustrate the method. Figures 4.2a and 4.2b show the values for the acoustic velocity and density as functions of depth and horizontal position. The dipole source emits a Ricker wavelet with 20Hz centre frequency. Absorbing boundary conditions are applied at two sides and bottom of the model, the top boundary of the model is set as free surface (the reflection coefficient of the free surface r is -1). We have computed the single-sided reflection responses with 601 sources and 601 particle-velocity receivers with a spacing of 10 m at the free-surface boundary. One of the computed single-sided reflection responses convolved with the source wavelet is shown in Figure 4.3a. Note that free-surface and internal multiple reflections occur, and the later primary reflections labelled by P7, P8 and P9 cannot be identified. The computed reflection responses are used as inputs to solve equations 4.6, 4.7 and 4.8 for U^- .

Then the procedure as described using equation 4.9 leads to the retrieved dataset shown in Figure 4.3b. Note that free-surface and internal multiple reflections visible in Figure 4.3a have disappeared, whereas the last three primary reflection events labelled by P7, P8 and P9, which cannot be distinguished from multiple reflections in Figure 4.3a, are clearly retrieved in Figure 4.3b. We pick the zero-offset traces from the datasets shown in Figures 4.3a and 4.3b and show them in Figure 4.4. It can be seen that free-surface and internal multiple reflections have been successfully removed and primary reflections labelled by P1,...,P6 in Figure 4.3 have been well retrieved. There is a mismatch of last three primary reflections labelled by P7, P8 and P9 in Figure 4.3 which is illustrated in Figure 4.4. This is caused by the fact that the last three primary reflections are overlapped with multiple reflections in the trace from the original shot gather. The red dotted line indicates the trace from the retrieved dataset and both traces have been normalised by the same normalization factor.

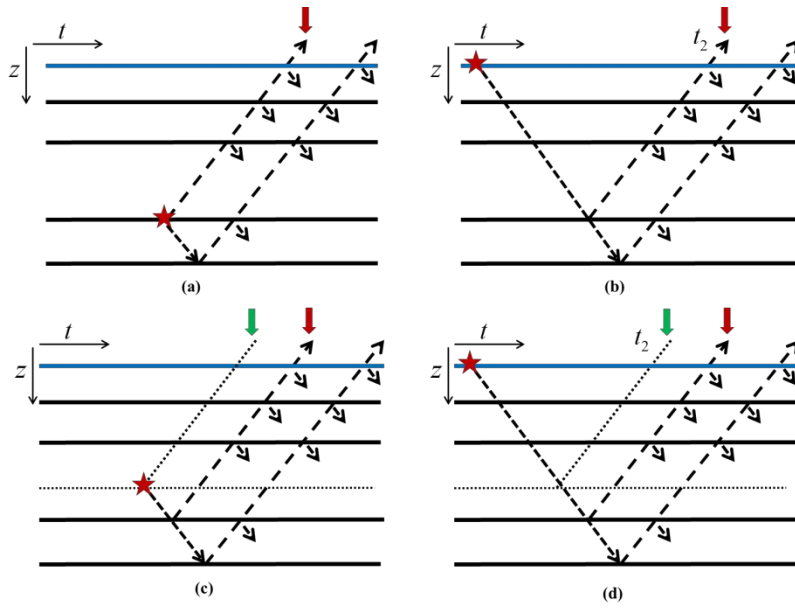


Figure 4.1: (a) 1D sketch of the reciprocal of G^- in equation 4.1 with the focusing point at, but just above the third reflector; (b) the corresponding U^- in equation 4.5; (c) 1D sketch of the reciprocal of G^- in equation 4.1 with the focusing point far from reflectors; (d) the corresponding U^- in equation 4.5. The dotted horizontal line in (c) and (d) indicate the focusing level. In each plot the red star indicates the focusing point (source), the red arrow indicates the first event and the green arrow indicates a zero-valued event at t_2 . The blue solid line indicates the pressure free surface.

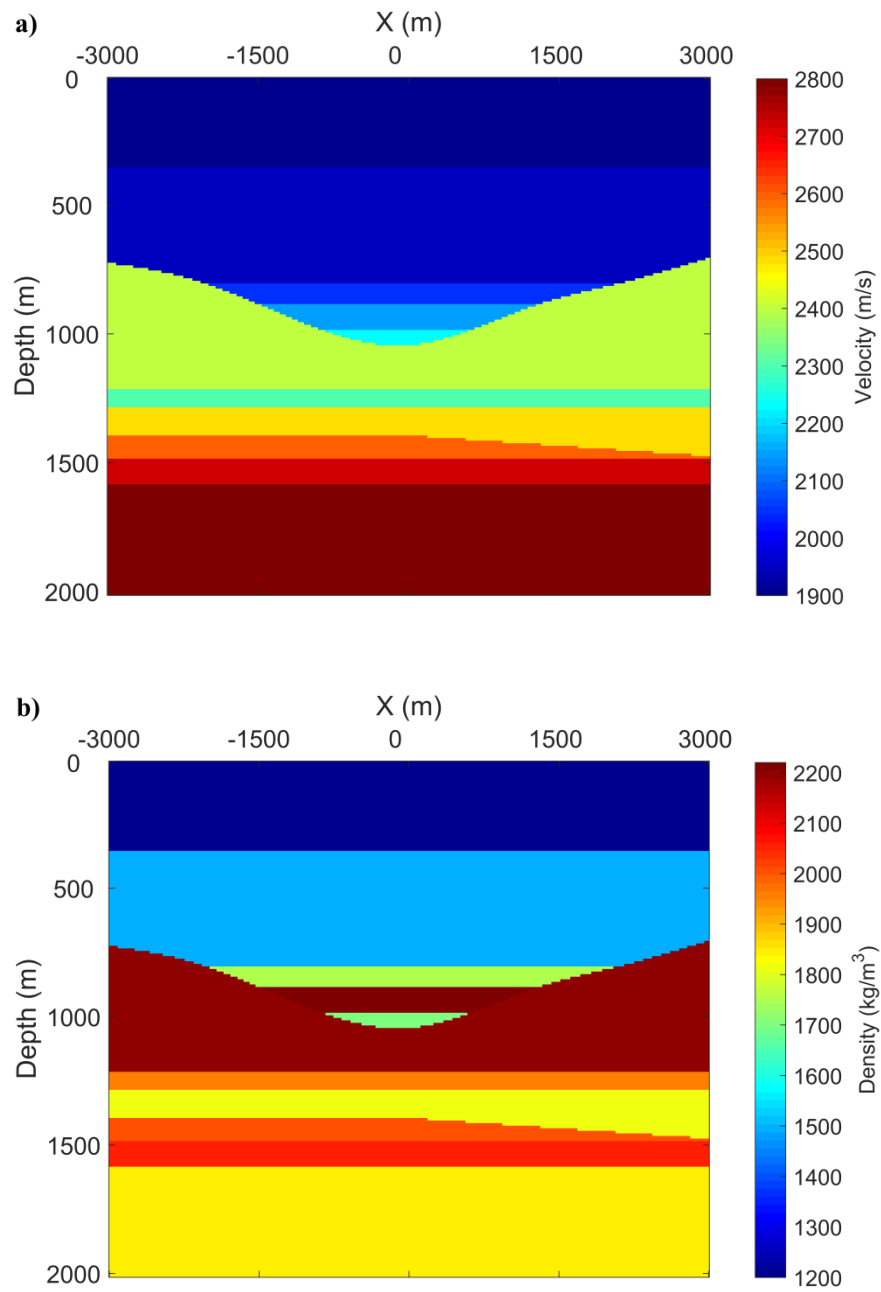


Figure 4.2: (a) The velocity and (b) density models that will be used to model the single-sided reflection response.

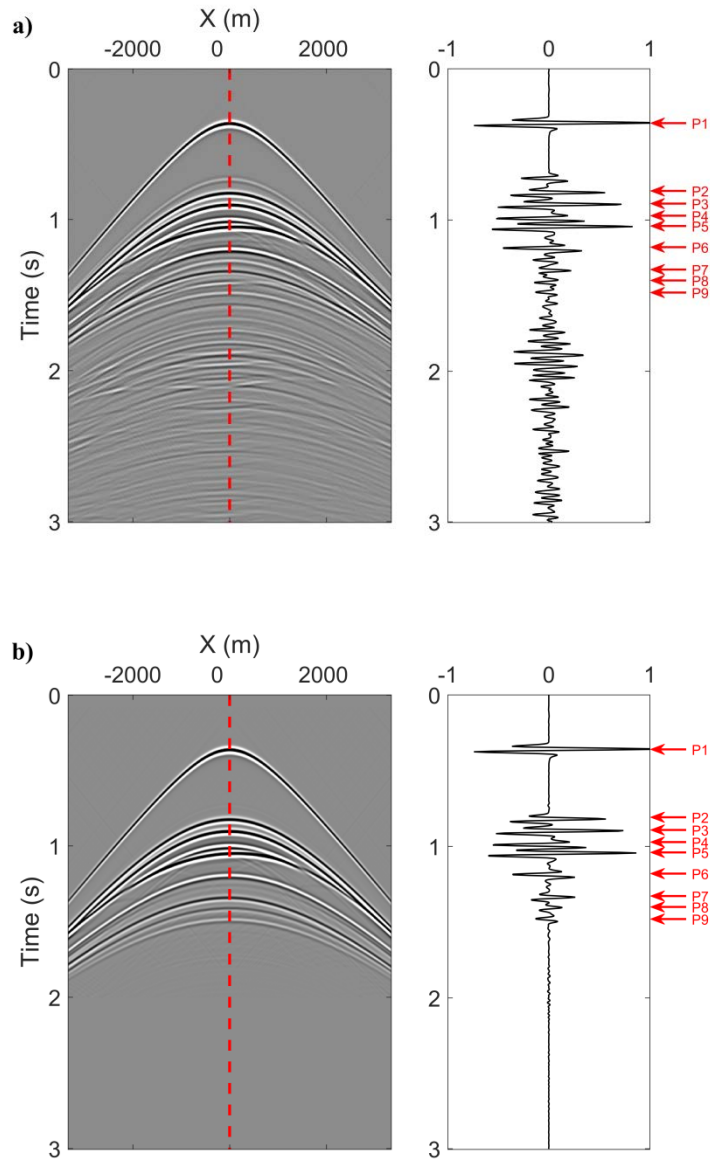


Figure 4.3: (a) The modelled reflection response and (b) the retrieved primary reflections. Red dashed lines indicate zero-offset traces plotted at the right side, P1,...,P9 label the primary reflections.

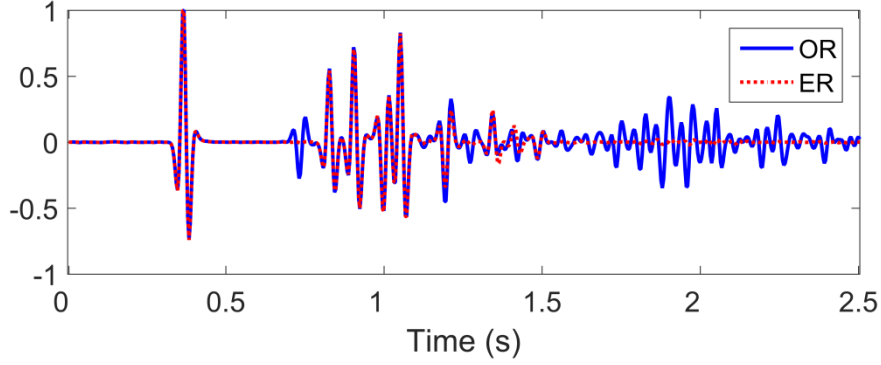


Figure 4.4: Comparison of zero-offset traces from Figure 4.3. The blue solid line (OR) comes from the original shot gather shown in Figure 4.3a and the red dotted line (ER) comes from the retrieved primary reflections shown in Figure 4.3b.

4.3 Extended T-MME scheme

4.3.1 Theory

We rewrite equations 4.6 and 4.7 with a modified truncation operator:

$$v^-(\mathbf{x}'_0, \mathbf{x}''_0, t, t_2) = R(\mathbf{x}'_0, \mathbf{x}''_0, t) + \int_{\partial D_0} d\mathbf{x}_0 \int_0^{+\infty} [R(\mathbf{x}'_0, \mathbf{x}_0, t') v_m^+(\mathbf{x}_0, \mathbf{x}''_0, t - t', t_2) - rR(\mathbf{x}'_0, \mathbf{x}_0, t') v^-(\mathbf{x}_0, \mathbf{x}''_0, t - t', t_2)] dt',$$

for $\varepsilon < t < t_2 + \varepsilon$ (4.10)

$$v_m^+(\mathbf{x}'_0, \mathbf{x}''_0, t, t_2) = \int_{\partial D_0} d\mathbf{x}_0 \int_{-\infty}^0 [R(\mathbf{x}'_0, \mathbf{x}_0, -t') v^-(\mathbf{x}_0, \mathbf{x}''_0, t - t', t_2) - rR(\mathbf{x}'_0, \mathbf{x}_0, -t') v_m^+(\mathbf{x}_0, \mathbf{x}''_0, t - t', t_2)] dt',$$

for $\varepsilon < t < t_2 + \varepsilon$ (4.11)

Note that equations 4.10 and 4.11 are different from equations 4.6 and 4.7 (the truncation operator in equations 4.10 and 4.11 is different from it in equations 4.6 and 4.7) to capture the desired result at t_2 in the projected focusing function, which ensures the compensation for transmission losses in the primary reflections that will now be found in the projected upgoing focusing function. This transmission compensated primary reflection will be found at t_2 in case t_2 happens to be the two-way travel time of a reflector, otherwise the value in the projected upgoing focusing function at t_2 will be zero. Therefore, we store the value of v^- for each time of t_2 in a new dataset. It can be written as

$$R_r(\mathbf{x}'_0, \mathbf{x}''_0, t = t_2) = v^-(\mathbf{x}'_0, \mathbf{x}''_0, t_2, t_2). \quad (4.12)$$

where R_r denotes the retrieved transmission compensated primary reflections.

Compared with the extended MME scheme, where free-surface and internal multiple reflections are eliminated in one step, the retrieved R_r from equation 4.12 is not only multiple-free, the transmission losses in the primary reflections are successfully compensated for. Still, no model information or adaptive filtering is required to run the scheme.

4.3.2 Example

In this section, two synthetic examples are given to validate the effectiveness of the extended T-MME scheme for multiple reflection elimination and transmission losses compensation. In these two examples, the reflection responses are modelled with absorbing boundary conditions applied at the two sides and the bottom of models, and the top surface is set as a pressure free surface, with the reflection coefficient of the free surface r given as -1. Dipole sources and particle-velocity receivers are positioned at the free surface of each model and the spacing is 10m. A Ricker wavelet with 20Hz centre frequency is emitted by the sources. The direct wave has been removed from the modelled reflection responses.

4.3.2.1 Horizontally layered model

Here, we consider a horizontally layered model to evaluate the scheme for removing multiple reflections and compensating for transmission losses in the primary reflections. Figure 4.5a and 4.5b show the acoustic velocity and density values of the model. We have modelled the reflection responses with 401 sources and 401 traces per shot gather, one of the modelled reflection responses convolved with the source wavelet is shown in Figure 4.6a. It can be seen that free-surface and internal multiple reflections are present as indicated by red arrows. The modelled reflection responses are used to solve equations 4.10 and 4.11 for v^- at each time instant t_2 . Then equation 4.12 is used to retrieve the transmission compensated primary reflections R_r . One of the retrieved datasets convolved with the source wavelet is shown in Figure 4.6b. Figure 4.6c shows the modelled primary reflections without transmission losses, which is convolved with the source wavelet and will be used as a reference to validate the success of our scheme for compensating for transmission losses in primary reflections. It can be seen that the free-surface and internal multiple reflections, present in Figure 4.6a, are absent in Figure 4.6b. We select the zero-offset traces from Figures 4.6a, 4.6b and 4.6c and show them in Figure 4.7. Figure 4.7a shows the comparison of zero-offset traces from Figures 4.6a and 4.6b. It can be seen that multiple reflections are removed, and the amplitudes of primary reflections are changed in the retrieved dataset. Figure 4.7b shows the comparison of zero-offset traces from Figures 4.6b and 4.6c. It can be seen that the retrieved primary reflections match well with the modelled primary reflections without transmission losses (quantitatively, a four percent error occurs in the amplitudes in the retrieved primary reflections). A similar conclusion can be drawn from Figure 4.8 where the comparison of nonzero-offset (800m) traces from Figures 4.6a, 4.6b and 4.6c is given. All traces in Figures 4.7 and 4.8 have been normalized by the same normalization factor.

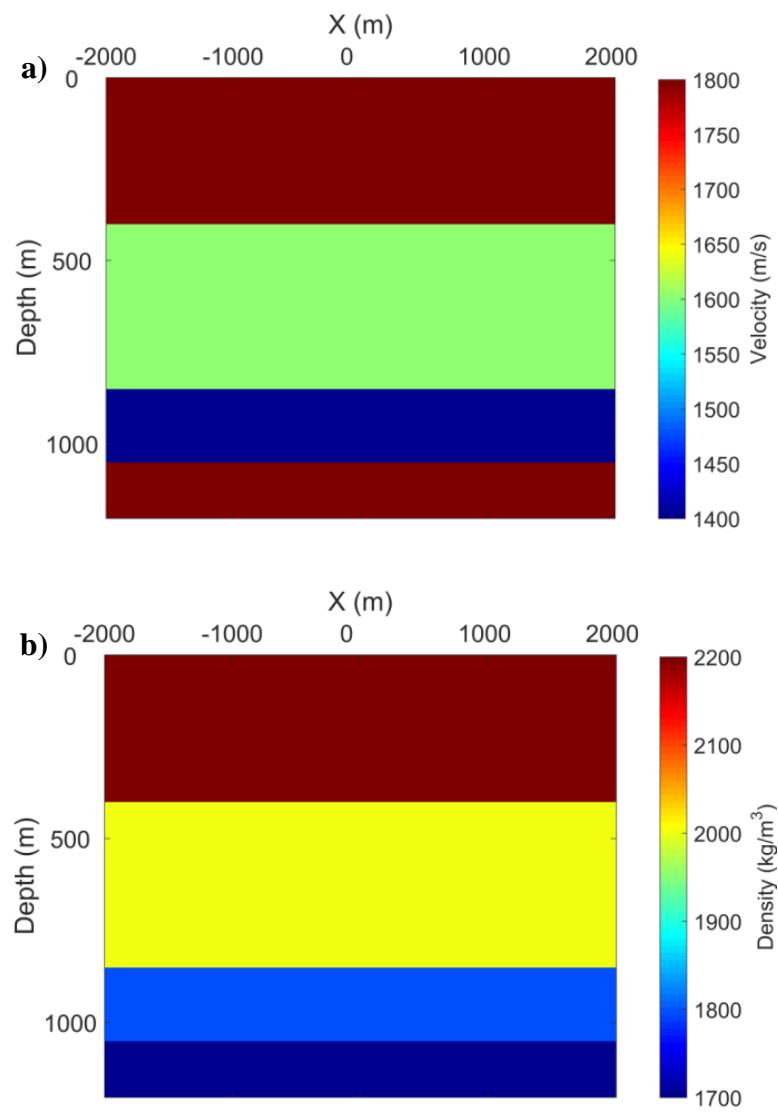


Figure 4.5: The (a) velocity and (b) density values of the horizontally layered model.

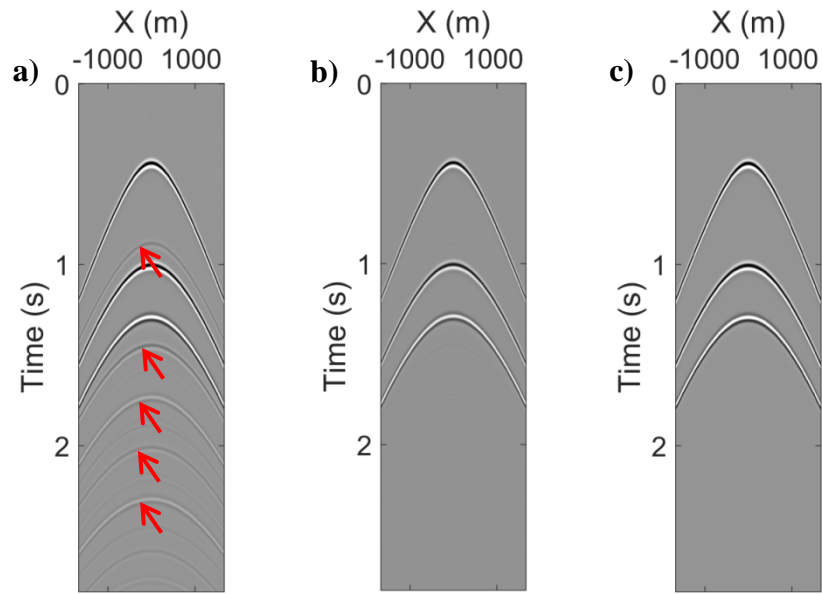


Figure 4.6: (a) The modelled reflection response, (b) the dataset retrieved by the extended T-MME scheme and (c) the modelled primary reflections without transmission losses. Red arrows indicate free-surface and internal multiple reflections.

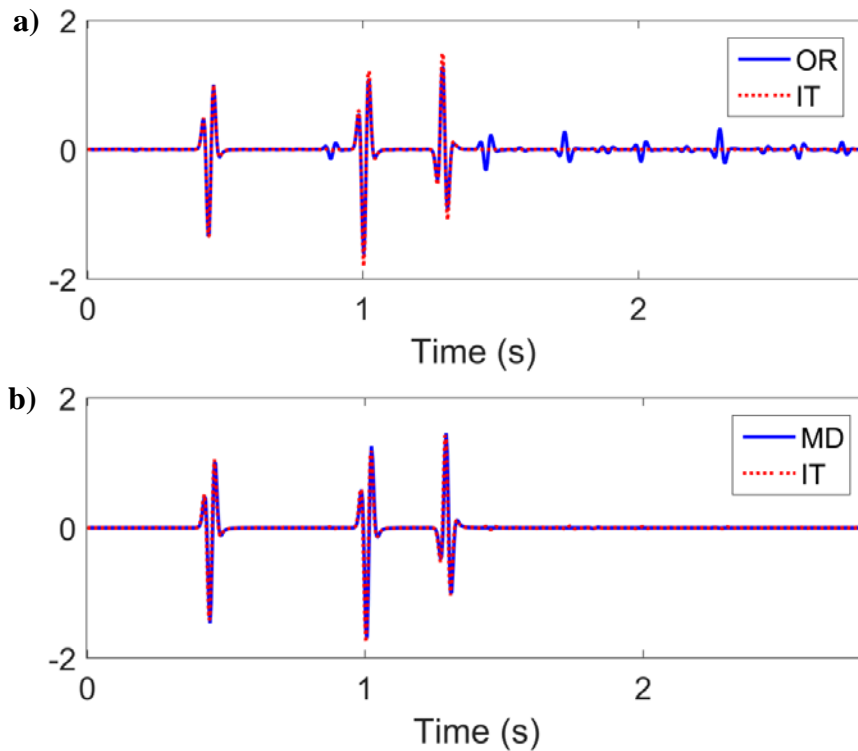


Figure 4.7: (a) The comparison of zero-offset traces from Figures 4.6a and 4.6b, (b) the comparison of zero-offset traces from Figures 4.6b and 4.6c. OR indicates zero-offset trace from Figure 4.6a, IT indicates trace from Figure 4.6b and MD indicates trace from Figure 4.6c.

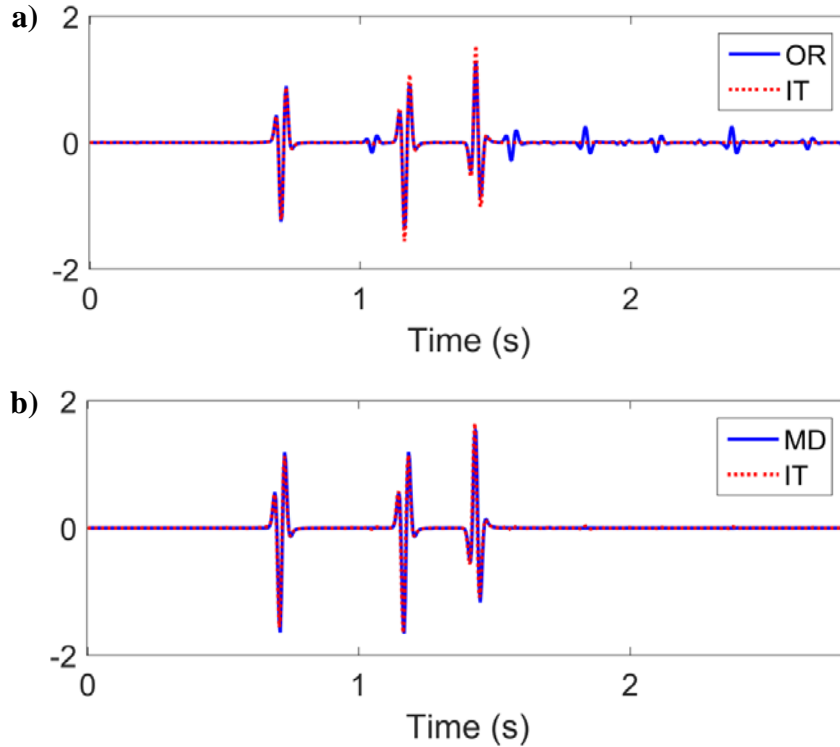


Figure 4.8: (a) The comparison of nonzero-offset (800m) traces from Figures 4.6a and 4.6b, (b) the comparison of nonzero-offset (800m) traces from Figures 4.6b and 4.6c. OR indicates trace from Figure 4.6a, IT indicates trace from Figure 4.6b and MD indicates trace from Figure 4.6c.

4.3.2.2 Complex model

We now apply our scheme to a complex 2D model to evaluate the performance. Figures 4.9a and 4.9b give the acoustic velocity and density values of the model. We have modelled the reflection responses with 601 sources and 601 traces per shot gather, two of the modelled reflection responses convolved with the source wavelet are given in Figures 4.10a and 4.10b. It can be seen that the two reflection responses contain many free-surface and internal multiple reflections which make it hard to identify later arrival primary reflections. The modelled reflection responses are used to solve equations 4.10 and 4.11 for v^- at each time instant t_2 . The procedure described in equation 4.12 leads to the retrieved primary reflections R_r with compensation for transmission losses. Two of the corresponding retrieved shot gathers convolved with the source wavelet are shown in Figures 4.10c and 4.10d. It can be seen that free-surface and internal multiple reflections visible in Figures 4.10a and 4.10b have been successfully removed and later arrival primary reflections, which are submerged in Figures 4.10a and 4.10b, have been recovered in Figures 4.10c and 4.10d. Note that the first free-surface multiple reflection overlap with the second primary reflection in Figures 4.10a and 4.10b. The amplitude of the second primary reflection in Figures 4.10c and 4.10d becomes weaker because of the elimination of the overlapping free-surface multiple reflection. In order to compare the amplitude of primary reflections before and after the

processing, we select zero-offset traces from Figures 4.10a and 4.10c and show them in Figure 4.11a. It can be seen that multiple reflections have been removed and amplitudes of primary reflections have been changed because of the compensation for transmission losses. A similar conclusion can be drawn from Figure 4.11b where the comparison of nonzero-offset (1000m) traces from Figures 4.10a and 4.10c is given. The traces in Figure 4.11 have been normalized by the same normalization factor. The transmission losses in the primary reflections are approximately compensated for because of the lateral heterogeneity of the complex medium model.

We use the modelled and retrieved datasets to compute images of the medium. The correct velocity model is used for both datasets. The images are obtained using a one-way wave equation migration scheme and shown in Figures 4.12a and 4.12b. The image shown in Figure 4.12a is from the modelled dataset. It contains artefacts arising from free-surface and internal multiple reflections. The image shown in Figure 4.12b is from the retrieved dataset. It is free from artefacts arising from free-surface and internal multiple reflections.

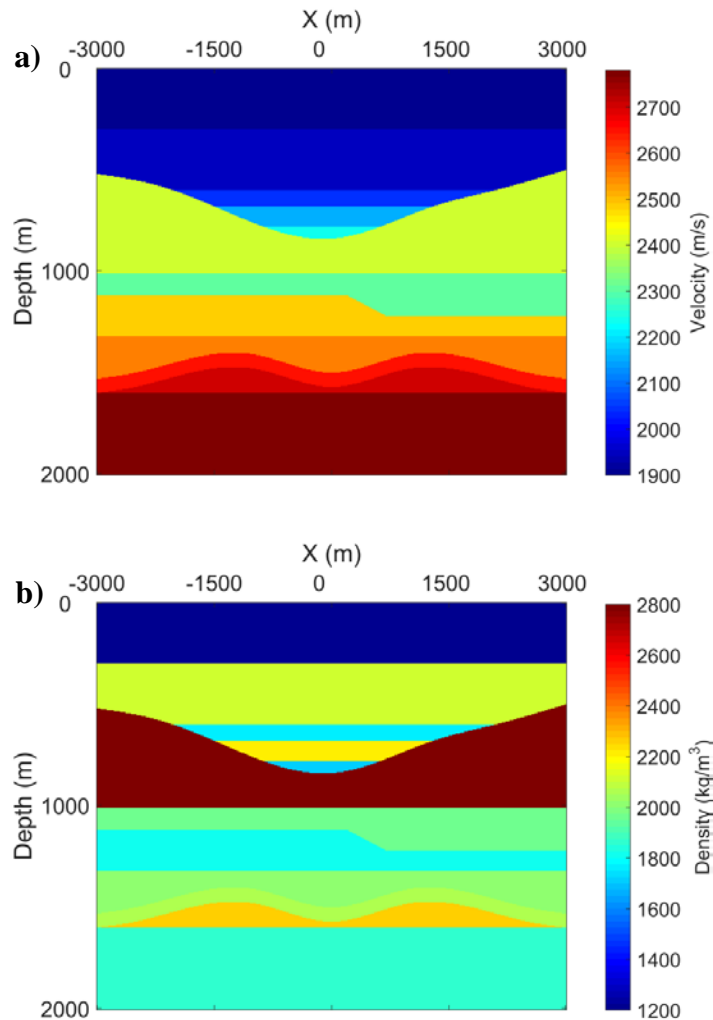


Figure 4.9: The (a) velocity and (b) density values of the complex model.

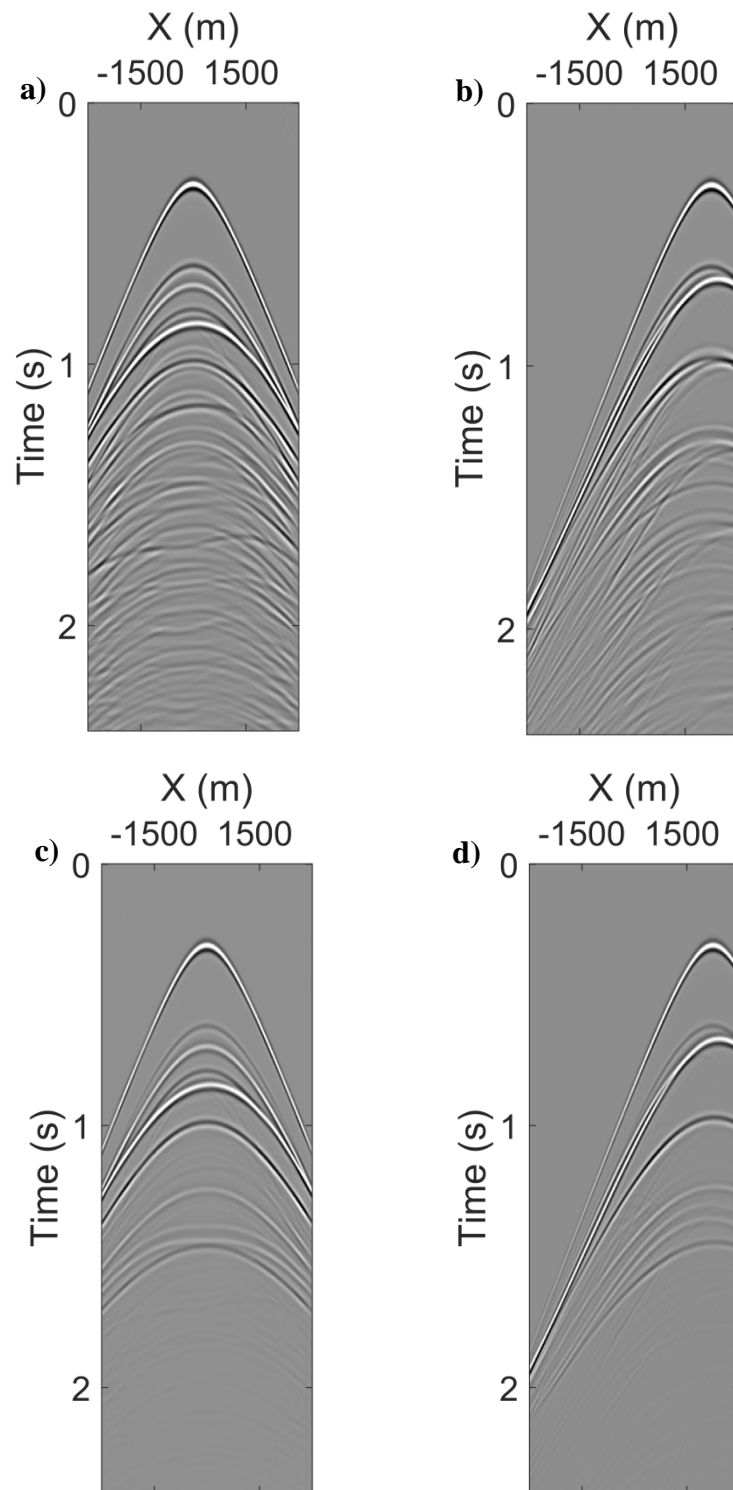


Figure 4.10: The (a) and (b) are two modelled reflection responses with sources at 0m and 1700m, (c) and (d) are the corresponding retrieved datasets by the extended T-MME scheme.

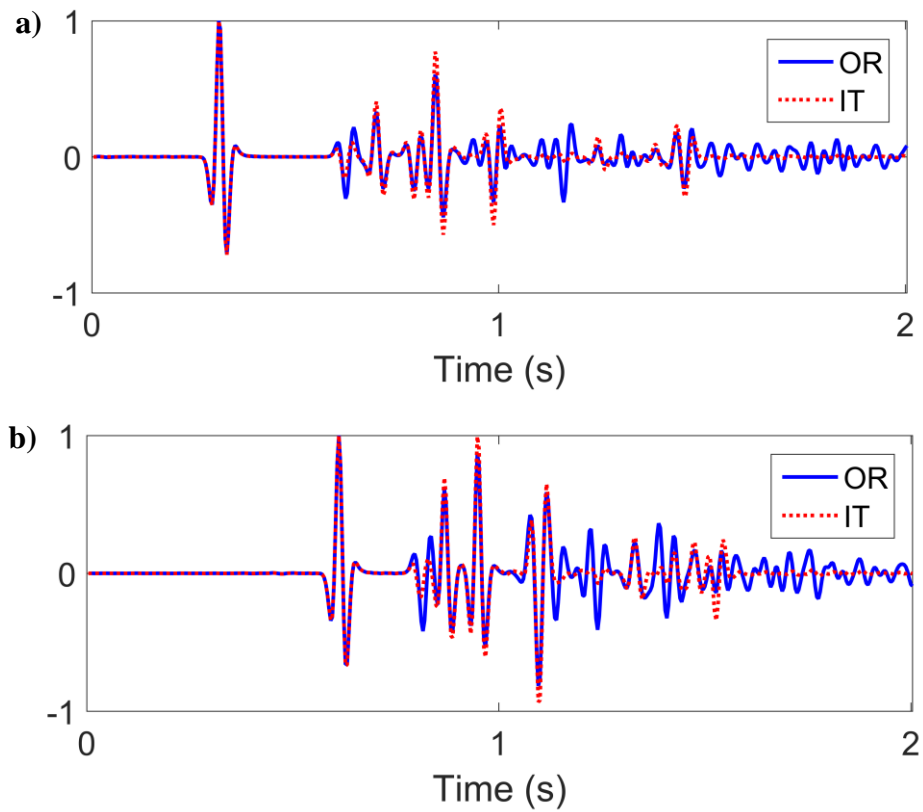
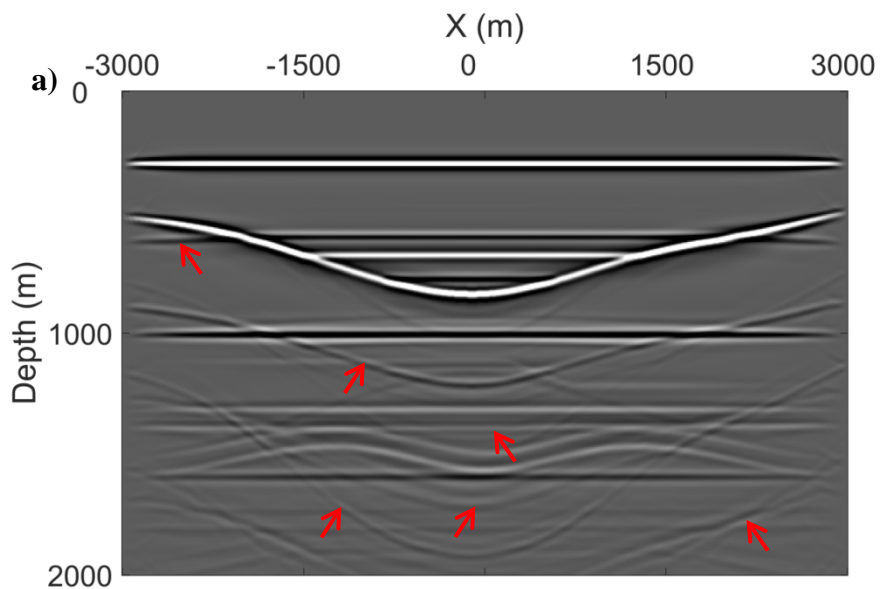


Figure 4.11: (a) The comparison of zero-offset traces from Figures 4.10a and 4.10c, (b) the comparison of nonzero-offset (1000m) traces from Figures 4.10a and 4.10c. OR indicates traces from Figure 4.10a, IT indicates traces from Figure 4.10c.



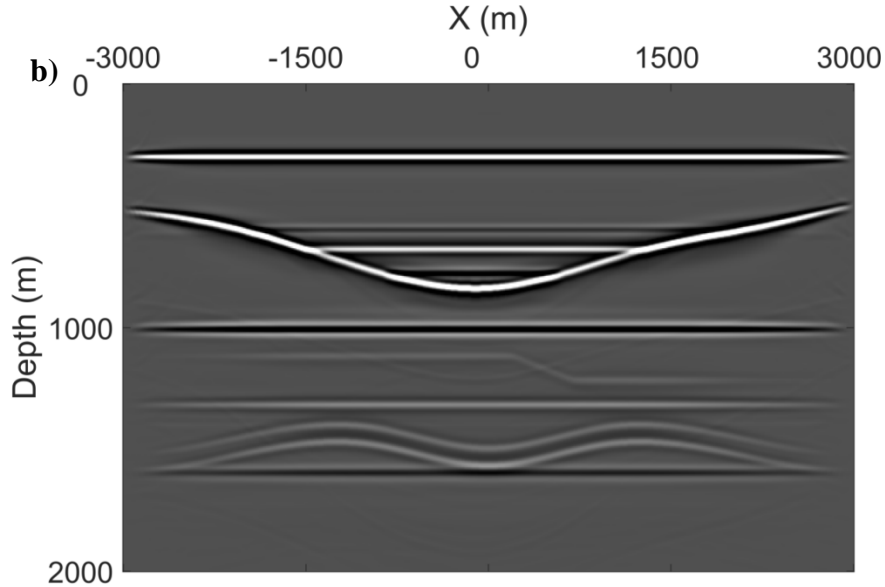


Figure 4.12: The (a) image retrieved from the modelled reflection responses and (b) the image retrieved from the resulting dataset of the extended T-MME scheme. Red arrows indicate artefacts arising from free-surface and internal multiple reflections.

4.4 Discussion

Equations 4.6 and 4.7 for the extended MME scheme and equations 4.10 and 4.11 for the extended T-MME scheme can be solved by the Neumann series expansion or unconditionally convergent methods, e.g., least square scheme or matrix inversion presented by [Dukalski and de Vos \(2018\)](#). The limitations of both schemes have been studied in detail for the convergence properties in [Dukalski and de Vos \(2018\)](#). Because that analysis was done in 1D, we have carried out some numerical experiments with very high impedance contrasts (leading to reflection coefficients up to 0.71) and found similar behaviour in 2D as reported in [Dukalski and de Vos \(2018\)](#). In the derivation of both methods, we assumed a lossless medium. The methods can be adapted to work with two-sided reflection and transmission data in dissipative media ([Slob, 2016](#)). We further assumed that the projected Green's functions and the focusing functions can be separated in time except for one time instant, that the source wavelet can be well recovered and the evanescent waves are absent ([Wapenaar et al., 2013](#)) as well as refractions. These restrictions limit the application of both methods, but not more than existing methods that require model information or adaptive filtering before the free-surface and internal multiple reflections are removed. For situations in which these assumptions are fulfilled, the proposed methods have nearly perfect performances as shown in 2D synthetic examples.

4.5 Conclusions

We have extended the MME and T-MME schemes to account for free-surface related multiple reflections, in which the single-sided reflection response is used to remove its own free-surface and internal multiple reflections. The reflection response is convolved and crosscorrelated with an intermediate wavefield that exists within a specific time window. From this intermediate wavefield the primary reflection is computed and stored in the new dataset. The 2D synthetic examples show that both methods effectively remove free-surface and internal multiple reflections in one step without any model information. The T-MME scheme also compensates for transmission losses in primary reflections.

References

- Dukalski, M., and K. de Vos, 2018, Marchenko inversion in a strong scattering regime including surface-related multiples: *Geophysical Journal International*, **212**, 760-776.
- Lopez, G. A., and D. J. Verschuur, 2015, Closed-loop surface-related multiple elimination and its application to simultaneous data reconstruction: *Geophysics*, **80**, no. 6, V189-V199.
- Singh, S., R. Snieder, J. van der Neut, J. Thorbecke, E. Slob, and K. Wapenaar, 2017, Accounting for free-surface multiples in Marchenko imaging: *Geophysics*, **82**, no. 1, R19-R30.
- Slob, E., 2016, Green's function retrieval and Marchenko imaging in a dissipative acoustic medium: *Physical Review Letters*, **116**, 164301.
- van der Neut, J., and K. Wapenaar, 2016, Adaptive overburden elimination with the multidimensional Marchenko equation: *Geophysics*, **81**, no. 5, T265-T284.
- van Groenestijn, G. J. A., and D. J. Verschuur, 2009, Estimating primaries by sparse inversion and application to near-offset data reconstruction: *Geophysics*, **74**, no. 3, A23-A28.
- Verschuur, D., A. Berkhout, and K. Wapenaar, 1992, Adaptive surface-related multiple elimination: *Geophysics*, **57**, 1166-1177.
- Wapenaar, K., F. Broggini, E. Slob, and R. Snieder, 2013, Three-dimensional single-sided Marchenko inverse scattering, data-driven focusing, Green's function retrieval, and their mutual relations: *Physical Review Letters*, **110**, 084301.
- Wapenaar, K., J. Thorbecke, J. van der Neut, F. Broggini, E. Slob, and R. Snieder, 2014, Marchenko imaging: *Geophysics*, **79**, no. 3, WA39-WA57.

5

Fast implementation of T-MME scheme

The primary reflections can be obtained from the single-sided acoustic reflection response in the two-way travel time domain by the MME and T-MME schemes. The substantial computational cost of both schemes can be reduced by an order of magnitude with a fast implementation. This is achieved by using the previously computed filter functions as initial estimate for every new truncation time value. Considering the similarity of MME and T-MME schemes, we give only the fast implementation of the T-MME and the extended T-MME schemes in detail in this chapter. 2D synthetic examples are given to illustrate the success.

5.1 Fast implementation of T-MME

5.1.1 Theory

We indicate time as t and a spatial location as $\mathbf{x} = (\mathbf{x}_H, z)$ with $\mathbf{x}_H = (x, y)$, where z denotes depth and \mathbf{x}_H denotes the vector containing the horizontal coordinates. The acoustically transparent surface $\partial\mathbf{D}_0$ is defined at $z_0 = 0$. We express the acoustic impulse reflection response as $R(\mathbf{x}'_0, \mathbf{x}_0, t)$, where \mathbf{x}'_0 denotes the receiver position and \mathbf{x}_0 denotes the source position at $\partial\mathbf{D}_0$. We start with the projected version of the modified Marchenko equations given in Chapter 3 (equations 3.22 and 3.23)

$$v^-(\mathbf{x}'_0, \mathbf{x}_0'', t, t_2) = R(\mathbf{x}'_0, \mathbf{x}_0'', t) + \int_{\partial\mathbf{D}_0} d\mathbf{x}_0 \int_0^{+\infty} R(\mathbf{x}'_0, \mathbf{x}_0, t') v_m^+(\mathbf{x}_0, \mathbf{x}_0'', t - t', t_2) dt',$$

for $\varepsilon < t < t_2 + \varepsilon$ (5.1)

$$v_m^+(\mathbf{x}'_0, \mathbf{x}_0'', t, t_2) = \int_{\partial\mathbf{D}_0} d\mathbf{x}_0 \int_{-\infty}^0 R(\mathbf{x}'_0, \mathbf{x}_0, -t') v^-(\mathbf{x}_0, \mathbf{x}_0'', t - t', t_2) dt',$$

for $\varepsilon < t < t_2 + \varepsilon$ (5.2)

where v_m^+ and v^- are projected versions of f_{1m}^+ and f_1^- as shown in equations 3.8 and 3.9, ε is a small positive value and t_2 denotes any desired time value within the time window of the measurement.

Here we choose to solve equations 5.1 and 5.2 iteratively as follows:

$$v_k^-(\mathbf{x}'_0, \mathbf{x}_0'', t, t_2) = R(\mathbf{x}'_0, \mathbf{x}_0'', t) + \int_{\partial\mathbf{D}_0} d\mathbf{x}_0 \int_0^{+\infty} R(\mathbf{x}'_0, \mathbf{x}_0, t') v_{m,k-1}^+(\mathbf{x}_0, \mathbf{x}_0'', t - t', t_2) dt',$$

for $\varepsilon < t < t_2 + \varepsilon$ (5.3)

$$v_{m,k}^+(\mathbf{x}'_0, \mathbf{x}_0'', t, t_2) = \int_{\partial\mathbf{D}_0} d\mathbf{x}_0 \int_{-\infty}^0 R(\mathbf{x}'_0, \mathbf{x}_0, -t') v_k^-(\mathbf{x}_0, \mathbf{x}_0'', t - t', t_2) dt',$$

for $\varepsilon < t < t_2 + \varepsilon$ (5.4)

where $k = 1, 2, \dots$ indicates the iteration number, and the choice

$$v_0^-(\mathbf{x}'_0, \mathbf{x}_0'', t, t_2) = 0, \quad (5.5)$$

$$v_{m,0}^+(\mathbf{x}'_0, \mathbf{x}_0'', t, t_2) = 0, \quad (5.6)$$

initialises the iterative scheme presented in equations 5.3 and 5.4. Thus, equations 5.1 and 5.2 can be solved iteratively for each value of t_2 with t_2 starting from zero to cover the whole recording time and incrementing t_2 with the time sampling dt of the dataset.

We make an interesting observation from Figure 5.1. In Figure 5.1a, the two-way travel time associated with the horizontal dotted line is the time instant t_2 . Suppose we have computed v^\pm for t_2 and we would like to compute it now for a later time instant $t_2 + dt$, such that the new depth level with two-way travel time $t_2 + dt$ is still above the third reflector. In that case

the projected focusing functions v^\pm do not change and we have $v^\pm(\mathbf{x}'_0, \mathbf{x}''_0, t, t_2 + dt) = v^\pm(\mathbf{x}'_0, \mathbf{x}''_0, t, t_2)$. In Figure 5.1b, the value of $t_2 + dt$ leads to inclusion of the third reflector. Even then, all previously obtained values remain unchanged and new values that need to be computed are associated only with the third reflector. These new values can occur in the entire time window $(\varepsilon < t < t_2 + dt + \varepsilon)$ of the projected focusing function. Thus, for a new time instant $t_2 + dt$, the initial estimate is given by

$$v_0^-(\mathbf{x}'_0, \mathbf{x}''_0, t, t_2 + dt) = v^-(\mathbf{x}'_0, \mathbf{x}''_0, t, t_2), \quad \text{for } \varepsilon < t < t_2 + dt + \varepsilon \quad (5.7)$$

$$v_{m,0}^+(\mathbf{x}'_0, \mathbf{x}''_0, t, t_2 + dt) = v_m^+(\mathbf{x}'_0, \mathbf{x}''_0, t, t_2). \quad \text{for } \varepsilon < t < t_2 + dt + \varepsilon \quad (5.8)$$

As long as each new depth level, with two-way travel time $t_2 + dt$, does not cross a new reflector, the iteration will terminate and we move to the next time instant. If the new depth level crosses a new reflector, $v_1^-(\mathbf{x}'_0, \mathbf{x}''_0, t, t_2 + dt)$ will be different from $v_0^-(\mathbf{x}'_0, \mathbf{x}''_0, t, t_2 + dt)$ and more iterations are required to properly account for the related events. Generally, fewer iterations are required than when the initial estimates given in equations 5.5 and 5.6 are used for solving the iterative scheme presented in equations 5.3 and 5.4. In 2D or 3D modelled data and in field data, every new time instant t_2 will possibly include a new (part of a) reflector. Still, fewer iterations are needed than with zero initial estimates, because all previously computed values will remain correct and only new ones related to the new reflector need to be computed. The retrieval of primary reflections $R_r(\mathbf{x}'_0, \mathbf{x}''_0, t = t_2) = v^-(\mathbf{x}'_0, \mathbf{x}''_0, t_2, t_2)$ with the new initial estimates will reduce the computational cost compared with solving the equation with zero initial estimates for each time instant.

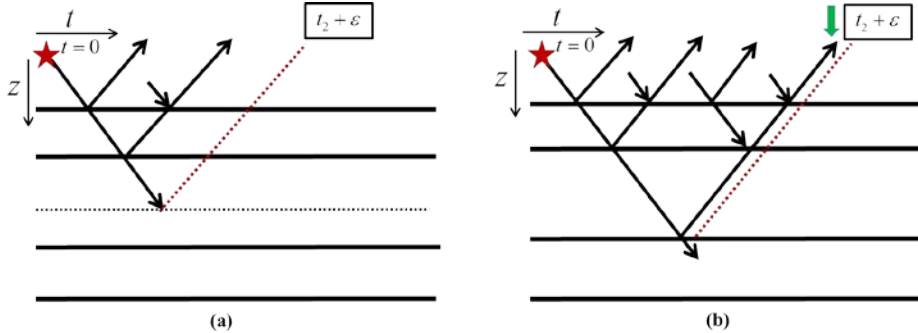


Figure 5.1: (a) 1D sketch of the projected focusing functions with focusing level far from reflectors; (b) 1D sketch of the projected focusing functions with focusing level coinciding with a reflector. The downgoing arrows indicate the projected downgoing focusing function v^+ and the upgoing arrows indicate the projected upgoing focusing function v^- . The dotted horizontal line in (a) indicates the focusing level. In each plot, the red star indicates the source point, the green arrow indicates the event with two-way travel time t_2 , and the red dotted line indicates the boundary inside the subsurface. Everything left of the red dotted line belongs to the projected focusing functions and everything right of the red dotted line belongs to the reflection data.

5.1.2 Example

We now apply the fast implementation to a complex 2D model to evaluate the performance. Dipole sources and pressure receivers are placed at the top of the model with a spacing of 10m and a Ricker wavelet, with 20Hz centre frequency, is emitted by sources. Absorbing boundary conditions are applied around the model and the direct wave has been removed. Figures 5.2a and 5.2b show the acoustic velocity and density values of the model. We have modelled the reflection responses with 601 sources and 601 traces per shot gather. One of the modelled reflection responses convolved with the source wavelet is given in Figure 5.3a. It can be seen that the reflection response contains many internal multiple reflections. The modelled reflection responses are used to solve equations 5.3 and 5.4 for v^- in the conventional and fast implementations respectively at each time instant t_2 . With zero initial estimates, the satisfied v^- is solved with $k_{\max} = 20$ whereas with the modified initial estimates we use $k_{\max} = 2$. The procedure described by $R_r(\mathbf{x}'_0, \mathbf{x}''_0, t = t_2) = v^-(\mathbf{x}'_0, \mathbf{x}''_0, t_2, t_2)$ leads to the retrieved primary reflection dataset with compensation for transmission losses. The resulting gather retrieved by the conventional implementation is shown in Figure 5.3b, and the resulting gather retrieved by the fast implementation is shown in Figure 5.3c. Both gathers are convolved with the source wavelet. It can be seen that internal multiple reflections visible in Figure 5.3a have been successfully removed in Figures 5.3b and 5.3c. Figure 5.3d shows the difference between the resulting gathers retrieved by the conventional and fast implementations. It validates the fact that the fast implementation can reduce the computational cost of the proposed scheme by an order of magnitude for retrieving the equivalent result ($k_{\max} = 20$ versus $k_{\max} = 2$). In order to compare the amplitudes of primary reflections before and after processing, we select zero-offset traces from Figures 5.3a, 5.3b and 5.3c and show them in Figures 5.4a and 5.4b. It can be seen that multiple reflections have been removed and amplitudes of primary reflections have been changed because of the compensation for transmission losses in both resulting gathers. A similar conclusion can be drawn from Figures 5.5a and 5.5b where the comparison of nonzero-offset (1000m) traces from Figures 5.3a, 5.3b and 5.3c is given. All traces in Figures 5.4 and 5.5 have been normalized by the same normalization factor. Note that, the transmission losses in the primary reflections are approximately compensated for because the lateral heterogeneity of the complex medium model prevents a full compensation.

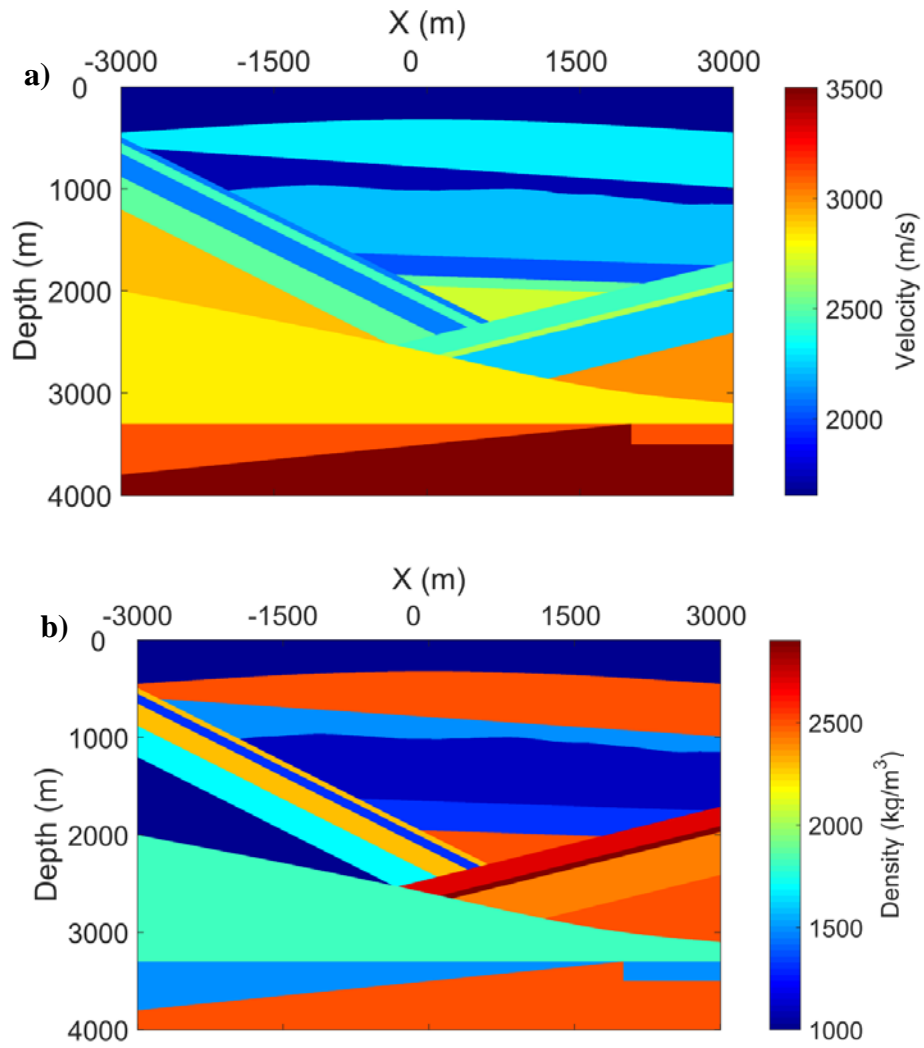


Figure 5.2: (a) The velocity and (b) density values of the model.

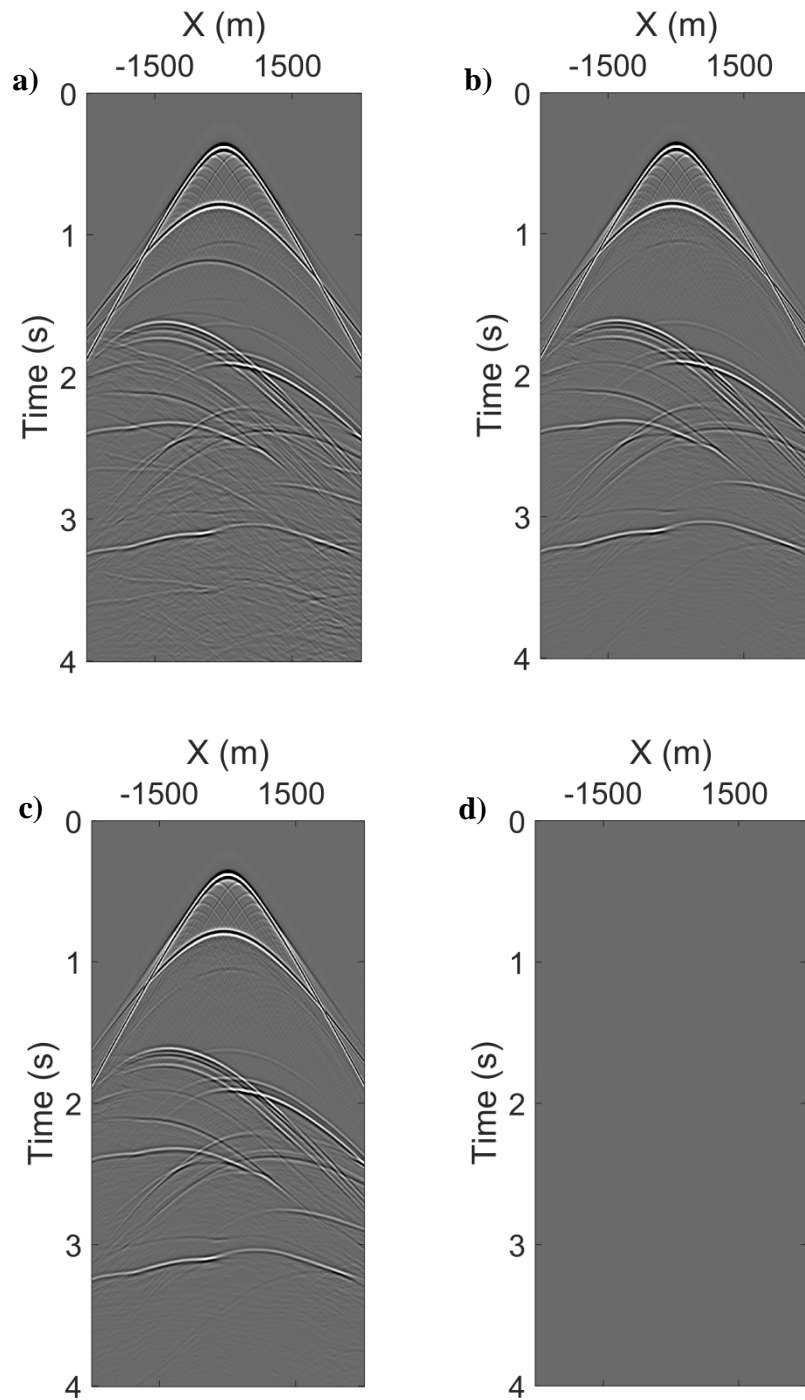


Figure 5.3: (a) The modelled reflection response, (b) the retrieved primary reflections by the conventional implementation and (c) the retrieved primary reflections by the fast implementation, (d) the difference between retrieved gathers by the conventional and fast implementations.

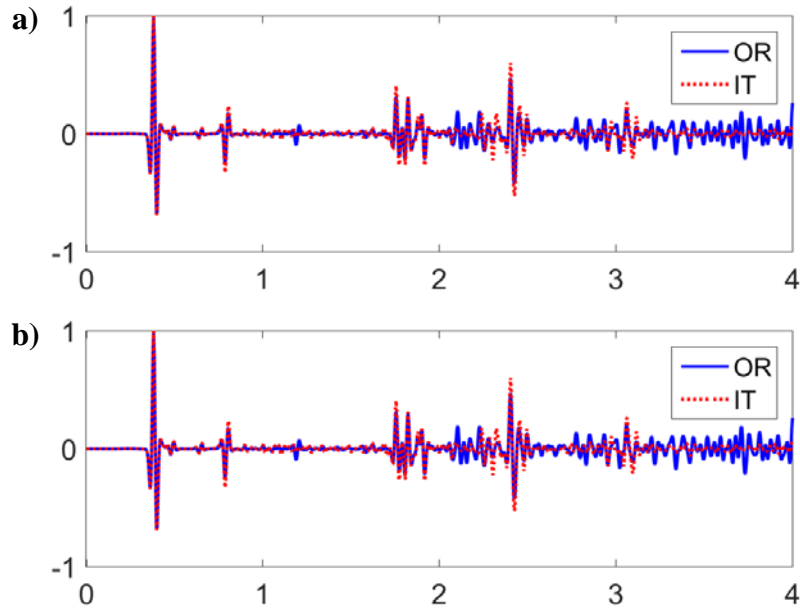


Figure 5.4: (a) The comparison of zero-offset traces from Figures 5.3a and 5.3b, (b) the comparison of zero-offset traces from Figures 5.3a and 5.3c. OR indicates trace from Figure 5.3a and IT indicates traces from Figures 5.3b and 5.3c.

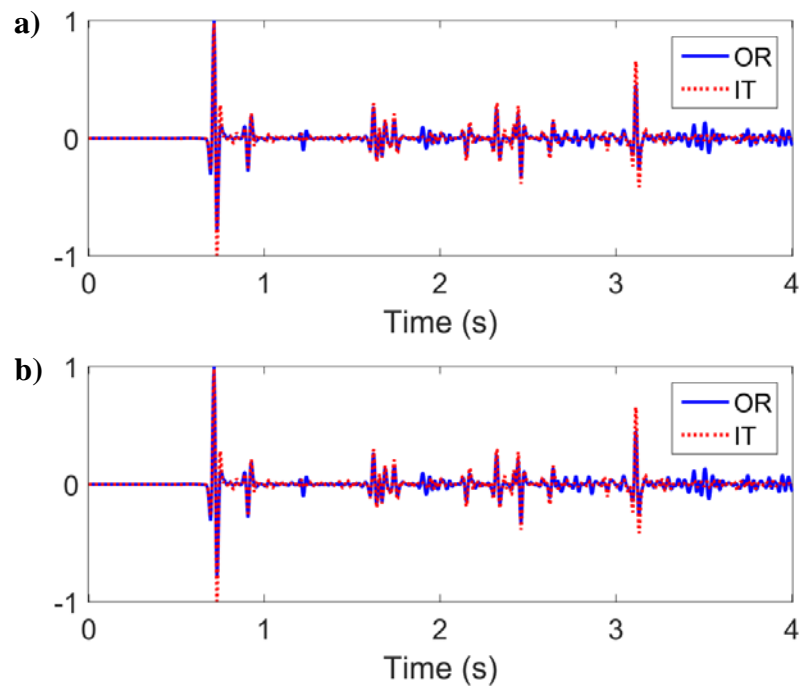


Figure 5.5: (a) The comparison of nonzero-offset (1000m) traces from Figures 5.3a and 5.3b, (b) the comparison of nonzero-offset (1000) traces from Figures 5.3a and 5.3c. OR indicates trace from Figure 5.3a and IT indicates traces from Figures 5.3b and 5.3c.

5.2 Fast implementation of extended T-MME

5.2.1 Theory

We indicate time as t and a spatial location as $\mathbf{x} = (\mathbf{x}_H, z)$ with $\mathbf{x}_H = (x, y)$, where z denotes depth and \mathbf{x}_H denotes the vector containing the horizontal coordinates. The pressure-free surface $\partial\mathbf{D}_0$ is defined at $z_0 = 0$. We express the acoustic impulse reflection response as $R(\mathbf{x}'_0, \mathbf{x}_0, t)$, where \mathbf{x}'_0 denotes the receiver position and \mathbf{x}_0 denotes the source position at the free surface $\partial\mathbf{D}_0$. We start with the projected version of the modified Marchenko equations from [Singh et al. \(2017\)](#) (equations 4.10 and 4.11)

$$v^-(\mathbf{x}'_0, \mathbf{x}''_0, t, t_2) = R(\mathbf{x}'_0, \mathbf{x}''_0, t) + \int_{\partial\mathbf{D}_0} d\mathbf{x}_0 \int_0^{+\infty} R(\mathbf{x}'_0, \mathbf{x}_0, t') [v_m^+(\mathbf{x}_0, \mathbf{x}''_0, t-t', t_2) - rv^-(\mathbf{x}_0, \mathbf{x}''_0, t-t', t_2)] dt',$$

for $\varepsilon < t < t_2 + \varepsilon$ (5.9)

$$v_m^+(\mathbf{x}'_0, \mathbf{x}''_0, t, t_2) = \int_{\partial\mathbf{D}_0} d\mathbf{x}_0 \int_{-\infty}^0 R(\mathbf{x}'_0, \mathbf{x}_0, -t') [v^-(\mathbf{x}_0, \mathbf{x}''_0, t-t', t_2) - rv_m^+(\mathbf{x}_0, \mathbf{x}''_0, t-t', t_2)] dt',$$

for $\varepsilon < t < t_2 + \varepsilon$ (5.10)

where v_m^+ and v^- are projected versions of f_{1m}^+ and f_1^- as shown in equations 3.8 and 3.9, ε is a small positive value and t_2 denotes any desired time value within the time window of the measurement, r indicates the reflection coefficient of the free surface. As explained in Chapter 4, the retrieval of transmission compensated primary reflections can be done by $R_r(\mathbf{x}'_0, \mathbf{x}''_0, t = t_2) = v^-(\mathbf{x}'_0, \mathbf{x}''_0, t_2, t_2)$. The retrieved new dataset R_r is free from free-surface and internal multiple reflections and contains only the corresponding transmission compensated primary reflections.

Here we also choose to solve equations 5.9 and 5.10 iteratively as follows:

$$v_k^-(\mathbf{x}'_0, \mathbf{x}''_0, t, t_2) = R(\mathbf{x}'_0, \mathbf{x}''_0, t) + \int_{\partial\mathbf{D}_0} d\mathbf{x}_0 \int_0^{+\infty} R(\mathbf{x}'_0, \mathbf{x}_0, t') [v_{m,k-1}^+(\mathbf{x}_0, \mathbf{x}''_0, t-t', t_2) - rv_{k-1}^-(\mathbf{x}_0, \mathbf{x}''_0, t-t', t_2)] dt',$$

for $\varepsilon < t < t_2 + \varepsilon$ (5.11)

$$v_{m,k}^+(\mathbf{x}'_0, \mathbf{x}''_0, t, t_2) = \int_{\partial\mathbf{D}_0} d\mathbf{x}_0 \int_{-\infty}^0 R(\mathbf{x}'_0, \mathbf{x}_0, -t') [v_k^-(\mathbf{x}_0, \mathbf{x}''_0, t-t', t_2) - rv_{m,k-1}^+(\mathbf{x}_0, \mathbf{x}''_0, t-t', t_2)] dt',$$

for $\varepsilon < t < t_2 + \varepsilon$ (5.12)

where $k = 1, 2, \dots$ indicates the iteration number, and the choice

$$v_0^-(\mathbf{x}'_0, \mathbf{x}''_0, t, t_2) = 0, \quad (5.13)$$

$$v_{m,0}^+(\mathbf{x}'_0, \mathbf{x}''_0, t, t_2) = 0, \quad (5.14)$$

initialises the iterative scheme presented in equations 5.11 and 5.12. Thus, equations 5.9 and 5.10 can also be solved iteratively for each value of t_2 with t_2 starting from zero to cover the

whole recording time and incrementing t_2 with the time sampling dt of the dataset. As shown in Figure 5.6, the initial estimates given in equations 5.13 and 5.14 can also be replaced by the solved projected focusing functions of previous time instant

$$v_0^-(\mathbf{x}'_0, \mathbf{x}''_0, t, t_2 + dt) = v^-(\mathbf{x}'_0, \mathbf{x}''_0, t, t_2), \quad \text{for } \varepsilon < t < t_2 + dt + \varepsilon \quad (5.15)$$

$$v_{m,0}^+(\mathbf{x}'_0, \mathbf{x}''_0, t, t_2 + dt) = v_m^+(\mathbf{x}'_0, \mathbf{x}''_0, t, t_2). \quad \text{for } \varepsilon < t < t_2 + dt + \varepsilon \quad (5.16)$$

Similarly, fewer iterations are required than when the initial estimates given in equations 5.13 and 5.14 are used for solving the iterative scheme presented in equations 5.11 and 5.12. Correspondingly, The retrieval of transmission compensated primary reflections with the new initial estimates will reduce the computational cost compared with solving the equations with zero initial estimates for each time instant.

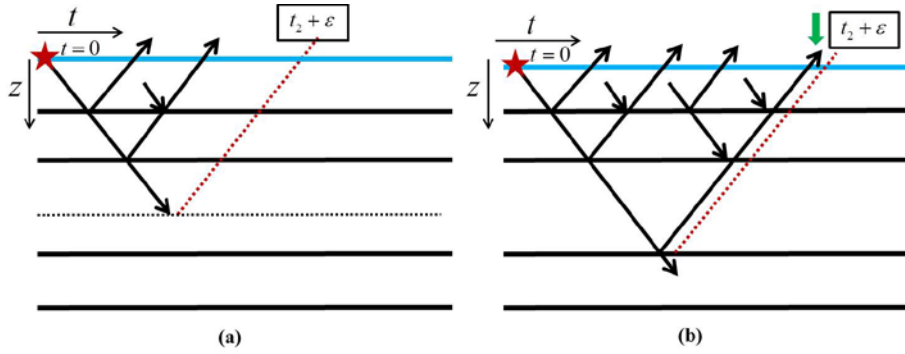


Figure 5.6: (a) 1D sketch of the projected focusing functions with focusing level far from reflectors; (b) 1D sketch of the projected focusing functions with focusing level coinciding with a reflector. The downgoing arrows indicate the projected downgoing focusing function v^+ and the upgoing arrows indicate the projected upgoing focusing function v^- . The dotted horizontal line in (a) indicates the focusing level. In each plot, the red star indicates the source point, the green arrow indicates the event with two-way travel time t_2 , and the red dotted line indicates the boundary inside the subsurface. Everything left of the red dotted line belongs to the projected focusing functions and everything right of the red dotted line belongs to the data. The blue solid line indicates the pressure-free surface. Where the red dotted line crosses the blue line is the time instant $t_2 + \varepsilon$ used for truncation.

5.2.2 Example

In this example, the reflection responses are modelled with absorbing boundary conditions applied at the two sides and the bottom of the model, and the top surface is set as a pressure-free surface, with the reflection coefficient of the free surface r given as -1 . Dipole sources and particle-velocity receivers are positioned at the free surface of the model and the spacing is 10m. A Ricker wavelet with 20Hz centre frequency is emitted by the sources. The direct wave has been removed from the modelled reflection responses. Figures 5.7a and 5.7b show the acoustic velocity and density values of the model. The reflection responses have been modelled with 601 sources and 601 traces per shot gather. One of the modelled dataset convolved with the source wavelet is given in Figure 5.8a. It can be seen that the reflection

responses contain many free-surface and internal multiple reflections. The modelled reflection responses are used to solve equations 5.11 and 5.12 for v^- in the conventional and fast implementations respectively at each time instant t_2 . With zero initial estimates, the satisfied v^- is solved with $k_{\max} = 20$ whereas with the modified initial estimates we use $k_{\max} = 2$. The resulting gather retrieved by the conventional implementation is shown in Figure 5.8b, and the resulting gather retrieved by the fast implementation is shown in Figure 5.8c. Both gathers are convolved with the source wavelet. Note that multiple reflections visible in Figure 5.8a have been successfully removed in Figures 5.8b and 5.8c. Figure 5.8d shows the difference between the resulting gathers retrieved by the conventional and fast implementations. It validates the fact that the fast implementation can reduce the computational cost of the proposed scheme by an order of magnitude for retrieving the equivalent result ($k_{\max} = 20$ versus $k_{\max} = 2$). Figures 5.9a and 5.9b give the comparison of zero-offset traces from Figures 5.8a, 5.8b and 5.8c. It can be seen that multiple reflections have been removed and amplitudes of primary reflections have been changed because of the compensation for transmission losses in both resulting gathers. A similar conclusion can be drawn from Figures 5.10a and 5.10b where the comparison of nonzero-offset (1000m) traces from Figures 5.8a, 5.8b and 5.8c is given. The traces in Figures 5.9 and 5.10 have been normalized by the same normalization factor. Still, the transmission losses in the primary reflections are approximately compensated for because the lateral heterogeneity of the complex medium model prevents a full compensation.

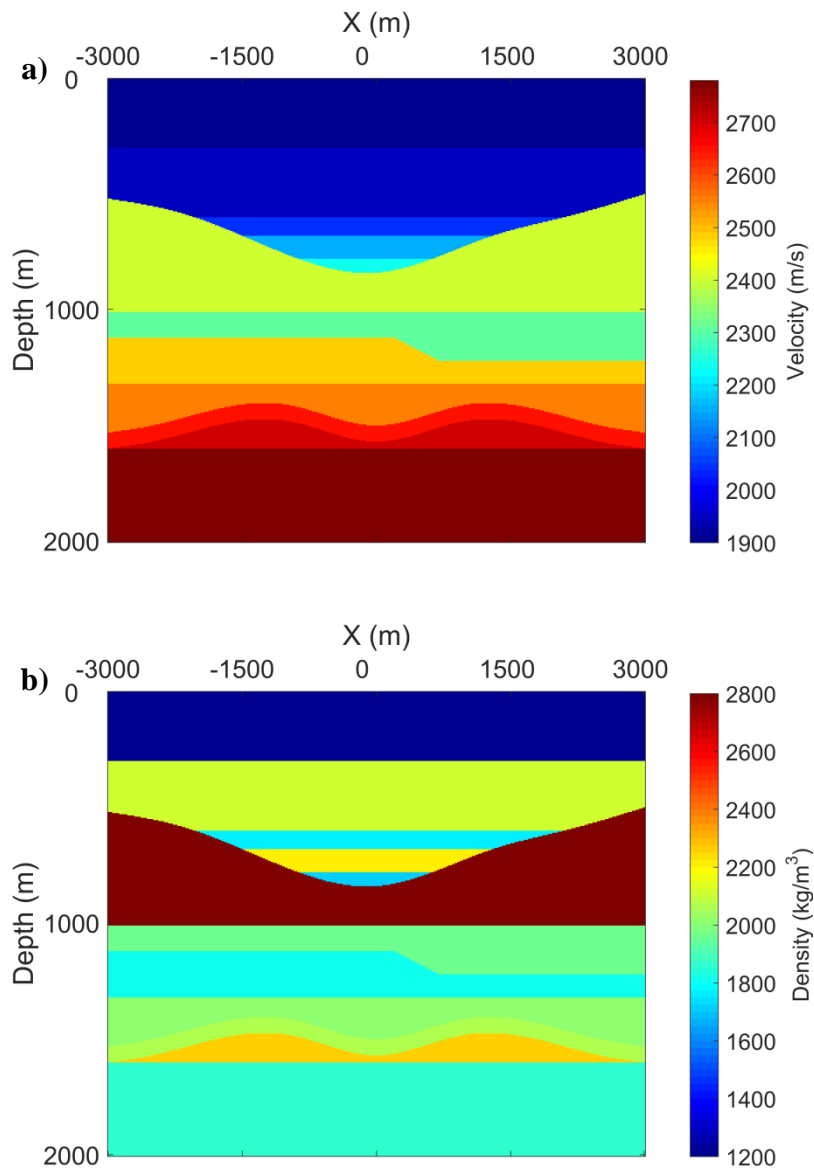


Figure 5.7: The (a) velocity and (b) density values of the complex medium model.

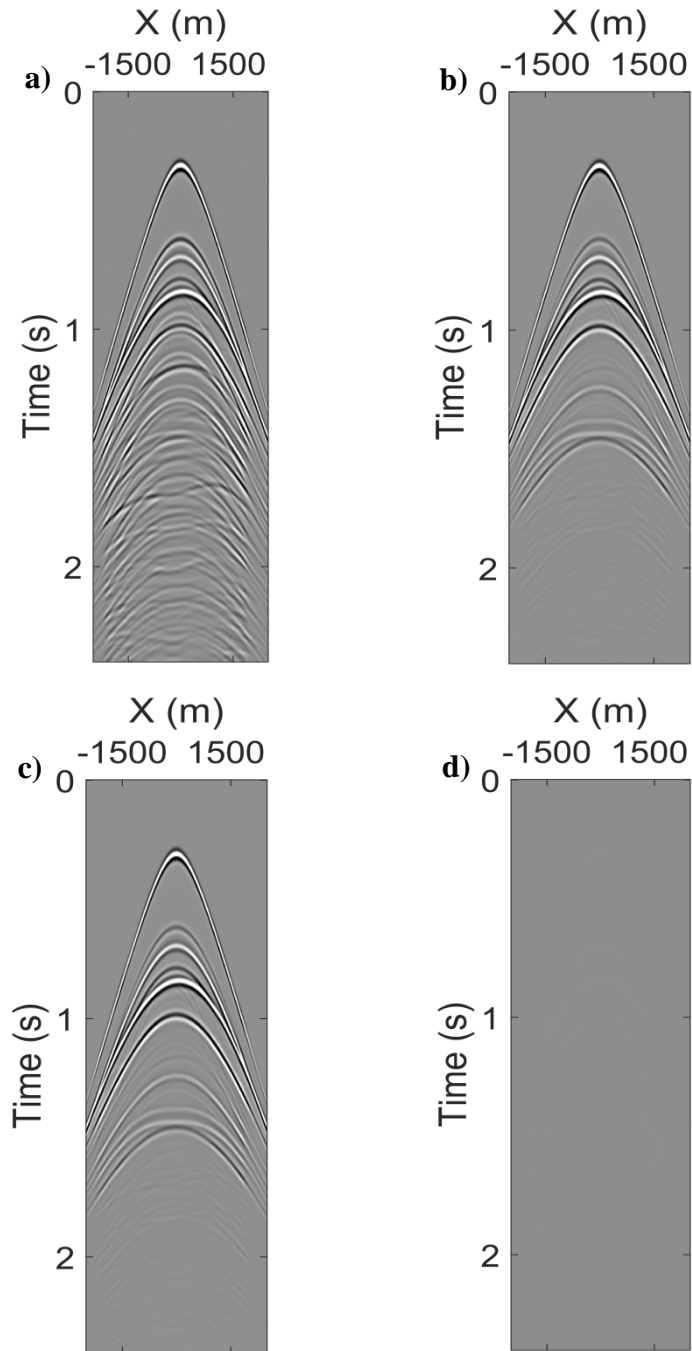


Figure 5.8: The modelled reflection response, (b) the corresponding retrieved dataset by the conventional implementation and (c) the retrieved dataset by the fast implementation, (d) the difference between retrieved gathers by the conventional and fast implementations.

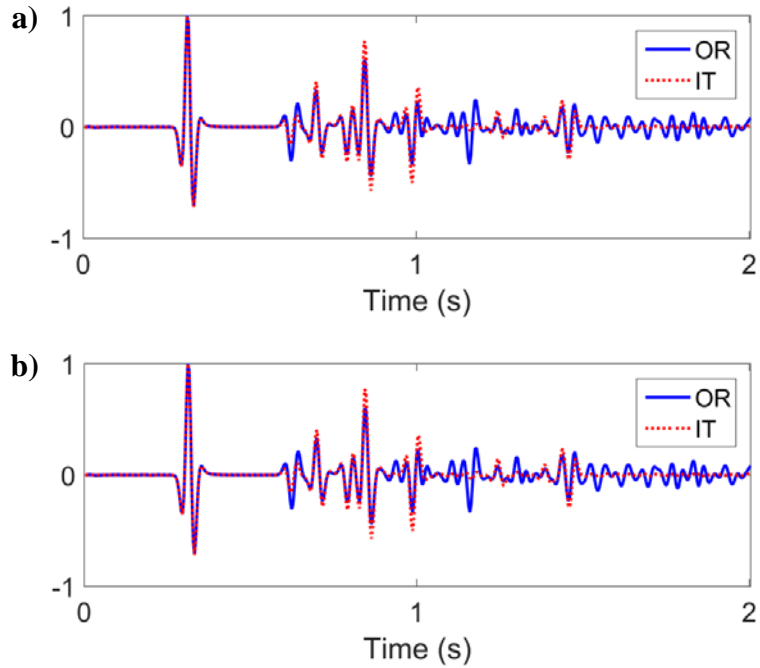


Figure 5.9: (a) The comparison of zero-offset traces from Figures 5.8a and 5.8b, (b) the comparison of zero-offset traces from Figures 5.8a and 5.8c. OR indicates trace from Figure 5.8a and IT indicates traces from Figures 5.8b and 5.8c.

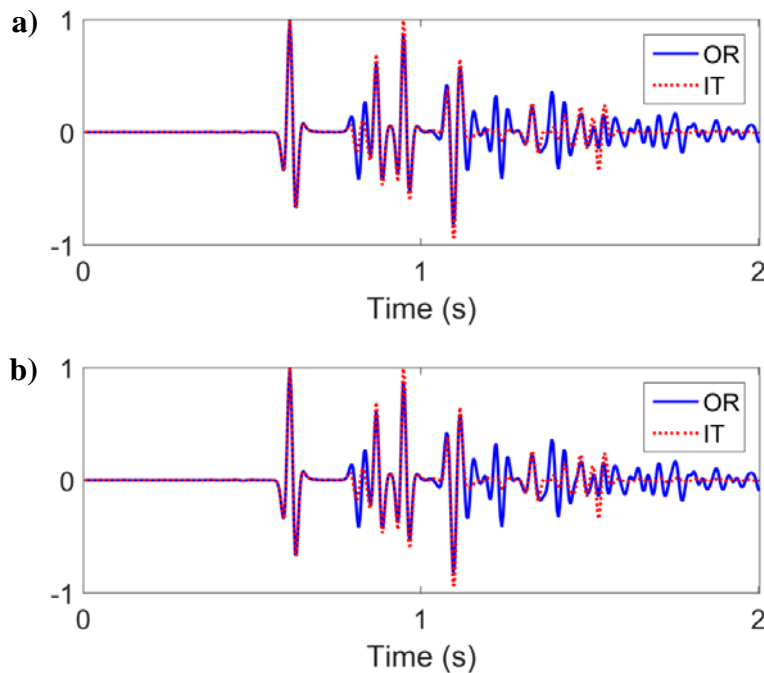


Figure 5.10: (a) The comparison of nonzero-offset (1000m) traces from Figures 5.8a and 5.8b, (b) the comparison of nonzero-offset (1000m) traces from Figures 5.8a and 5.8c. OR indicates trace from Figure 5.8a and IT indicates traces from Figures 5.8b and 5.8c.

5.3 Discussion

The fast implementation modifies the starting point, but not the operator of the equation to be solved. This means that the same limitations apply to the fast implementation as for the conventional implementation.

As explained in Chapters 3 and 4, the MME and extended MME schemes are derived from the same basic theory with T-MME and extended T-MME schemes with different truncation operators. Thus, the fast implementation proposed for T-MME and extended T-MME schemes in this Chapter also works for MME and extended MME schemes. Correspondingly, the computational cost of MME and extended MME schemes can also be reduced by an order of magnitude.

5.4 Conclusions

We have shown that, for the T-MME and the extended T-MME schemes, the projected focusing functions computed for a certain time instant can be used as an initial estimate for the next time instant. This reduces the computational cost of the schemes in our examples by an order of magnitude. No model information or adaptive subtraction is required. The complex synthetic examples illustrate the success of the fast implementation of both T-MME and extended T-MME schemes. The fast implementation also works for the MME and extended MME schemes. We think the fast algorithm can be of interest in exploration geophysics for retrieving datasets with only primary reflections, velocity model building, artefact-free migration, and inversion.

References

Singh, S., R. Snieder, J. van der Neut, J. Thorbecke, E. Slob, and K. Wapenaar, 2017, Accounting for free-surface multiples in Marchenko imaging: *Geophysics*, **82**, no. 1, R19–R30.

6

Laboratory and Field Examples

In this Chapter, we apply the MME and T-MME schemes to measured Laboratory and field datasets to test the performance. The main body can be split into two parts. In the first part, we apply the MME scheme to a measured Laboratory dataset to evaluate the success of the method. In the second part, both MME and T-MME schemes are applied to a deep-water field dataset from the Norwegian North Sea. The results suggest that the MME and T-MME schemes can be the appropriate choice, when high-quality pre-processing is performed successfully.

6.1 Laboratory Example

Here, a laboratory ultrasonic dataset acquired with a 3D geometry from a 3D physical model shown in Figure 6.1a is considered. The size of the model is $70 \times 600 \times 600$ mm. The model is composed of silicone gel and beeswax layers and is placed in a water tank. The acquisition is carried out along the horizontal line indicated in Figure 6.1a and the acquisition line is almost perpendicular to the main fault plane of the model. The ultrasonic signal with central frequency 1.1MHz is emitted and received by piezo-electric transducers 12 mm above the upper boundary of the model. The spacing of the transducers is 1.25 mm. A 2D cross-section of the model below the acquisition line is shown in Figures 6.1b (velocity) and 6.1c (density) (this 2D model is as close as possible to the real 2D slice of the physical model). The spatial dimensions have been scaled by the factor 20000. A more detailed description of the physical modelling tank and the 3D acquisition system can be found in [Koek et al. \(1995\)](#), [Blacquiere et al. \(1999\)](#) and [Wapenaar et al. \(2018\)](#). The measured data from the acquisition line is selected as a 2D experiment to test the performance of the MME scheme. There are 301 shot gathers in the selected 2D slice and each shot gather has 212 traces. Before further processing, the selected 2D data is interpolated to a receiver spacing of 0.625 mm to suppress spatial aliasing. The free surface multiple reflections fall well outside the measured time window. The 2D synthetic data computed from the model shown in Figures 6.1b and 6.1c is used as a reference to understand the performance of the MME scheme on the measured laboratory data.

6.1.1 Synthetic 2D dataset

We compute a 2D dataset from the model shown in Figures 6.1b and 6.1c with dipole sources and pressure receivers positioned at the top of the model to test the success of the MME scheme. There are 301 shot gathers in the computed 2D dataset and 424 traces per shot gather. The spacing of sources and receivers is 12.5 m. The sources emit a Ricker wavelet with 20 Hz central frequency. Absorbing boundary conditions are applied around the model such that there are no free surface multiple reflections present in the modelled dataset. The direct wave has been removed in the modelled dataset. Figures 6.2a and 6.2c show two of the modelled reflection responses (convolved with the source wavelet) with source positions indicated by the red stars (6000m and 8200m) in Figure 6.1b. Internal multiple reflections are indicated by red and green arrows in Figures 6.2a and 6.2c. They are so strong that later primary reflections are masked. We use the computed 2D reflection dataset as input to retrieve R_t , and two of the corresponding retrieved datasets convolved with the source wavelet are shown in Figures 6.2b and 6.2d. Note that internal multiple reflections, indicated by the red and green arrows in Figures 6.2a and 6.2c, are absent and primary reflections that were masked are recovered and visible in Figures 6.2b and 6.2d.

We use the velocity model shown in Figure 6.1b for migrating the computed and retrieved datasets. A one-way wave equation migration scheme is used here. The computed images of the target zone are shown in Figures 6.3a and 6.3b. The image shown in Figure 6.3a is from

the computed dataset and contains artefacts arising from internal multiple reflections, indicated by red arrows, because of the single-scattering assumption of the migration scheme. The image shown in Figure 6.3b, which is from the retrieved dataset, is free from these artefacts. Note that there are some gaps indicated by green arrows in Figures 6.3a and 6.3b, which are caused by the finite length of the acquisition.

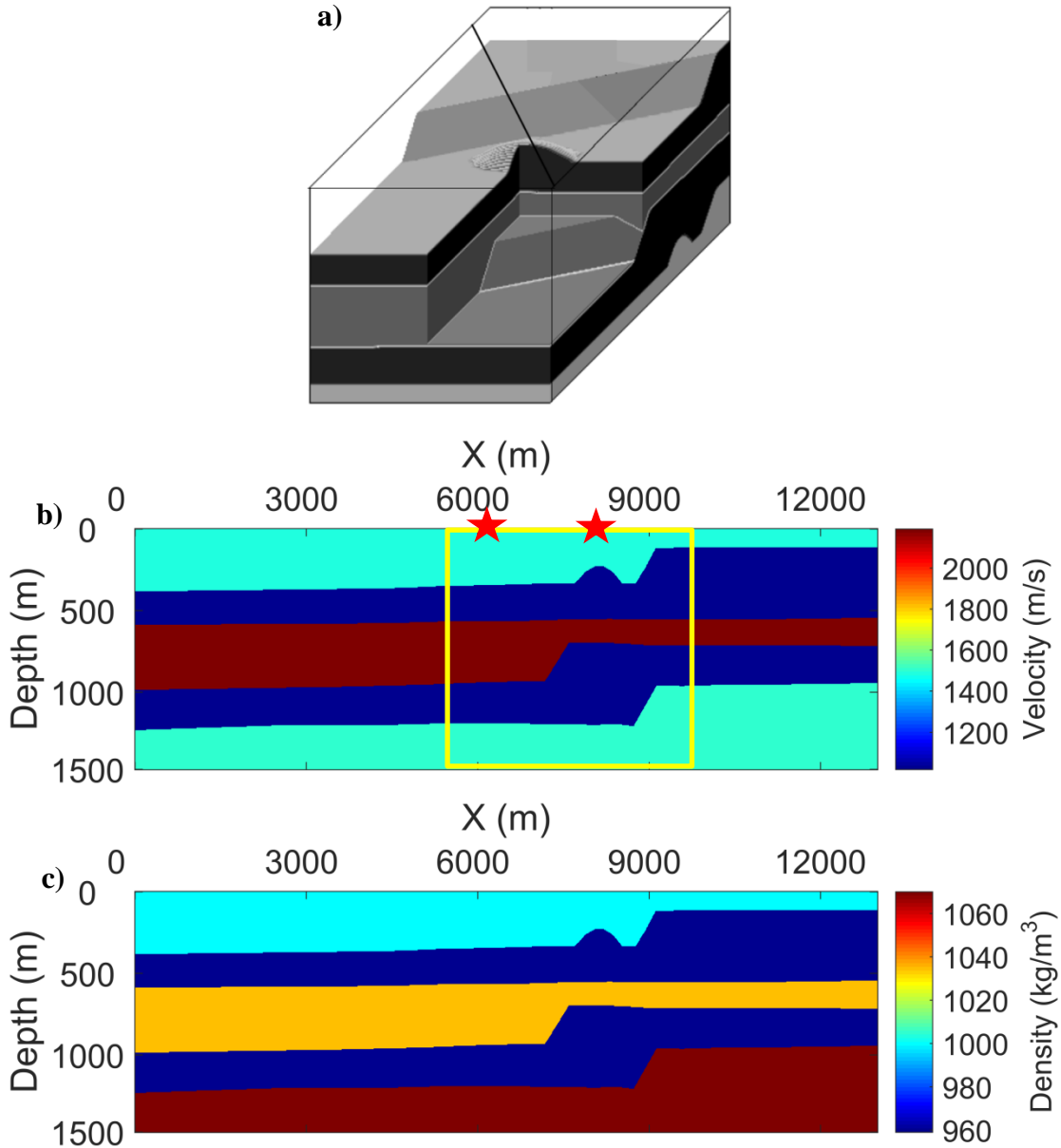


Figure 6.1: (a) The 3D physical model, (b) the velocity model of the scaled 2D cross section along the acquisition line, red stars indicate source positions of two reflection responses shown in Figure 6.2, the yellow box marks the target zone which is imaged, (c) the density model of the scaled 2D cross section along the acquisition line.

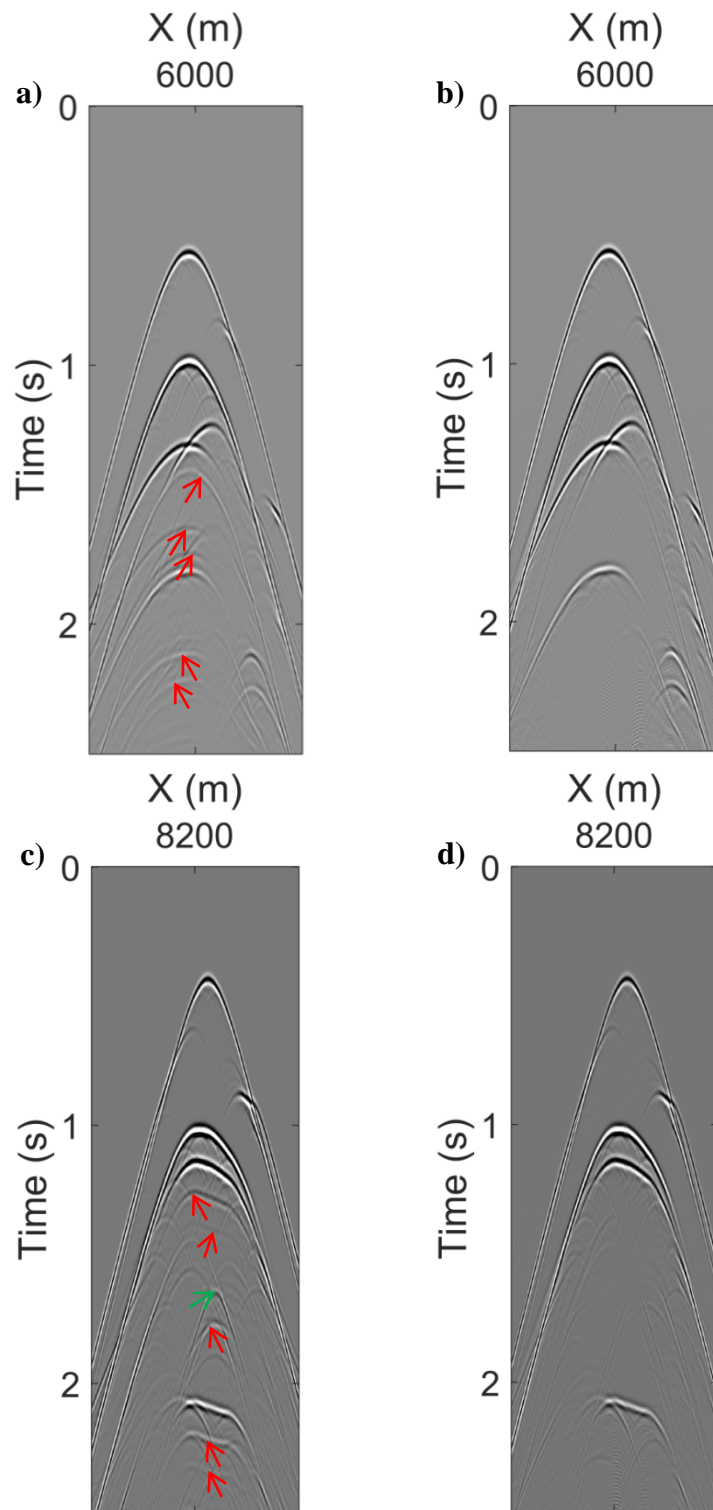


Figure 6.2: Two computed reflection responses with source positions at 6000 m (a) and 8200 m (c) as indicated by the red stars in Figure 6.1b, the corresponding retrieved datasets by the MME scheme with source positions at 6000 m (b) and at 8200 m (d). Red and green arrows in (a) and (c) indicate internal multiple reflections.

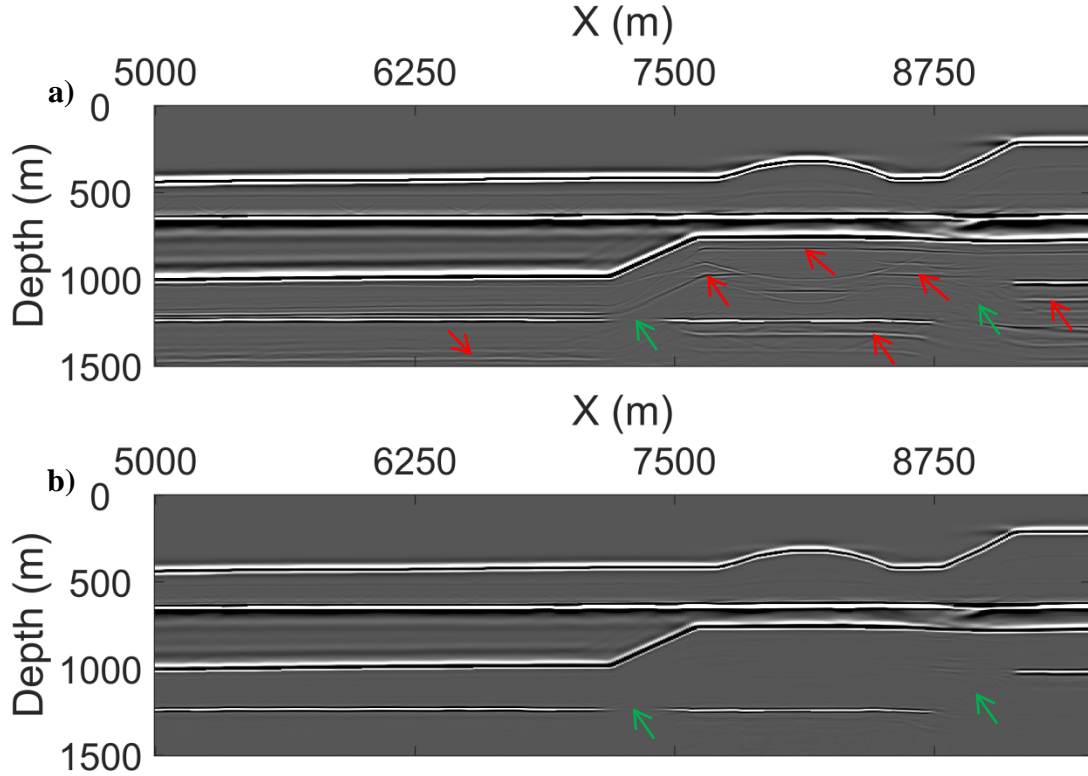


Figure 6.3: (a) The image retrieved from the computed dataset and (b) the image retrieved from the resulting dataset of the MME scheme. Red arrows in (a) indicate artefacts arising from internal multiple reflections, green arrows in (a) and (b) indicate gaps in the image.

6.1.2 Laboratory 2D dataset

The physical model shown in Figure 6.1 has well-defined and well-separated interfaces and the measured dataset appears to be fit enough for internal multiple elimination by the MME scheme. We apply the MME scheme to the selected acquisition line of the laboratory dataset to test its performance. The measured laboratory dataset has been pre-processed with following steps: (1) mute direct wave, (2) interpolate the missing near-offset data using parabolic Radon transform (Kabir and Verschuur, 1995), (3) multiply the dataset with \sqrt{t} time gain to correct from 3D to 2D propagation, (4) deconvolve source signature with predictive deconvolution and (5) interpolate receivers using sparse linear Radon transform (random noise was also attenuated in this step because of the denoising effect of the sparse Radon transform). Note that the ghosts and reflections from the free surface and both sides of the model fall well outside the measured time window. Thus, they are not present in the measured dataset. Two reflection responses with source positions indicated by red stars in Figure 6.1b are shown in Figures 6.4a and 6.4d. We use the selected line dataset as input to retrieve R_t , and the predicted internal multiple reflections are given in Figures 6.4b and 6.4e, and the corresponding retrieved datasets are shown in Figures 6.4c and 6.4f. Internal multiple reflections indicated by red, yellow and green arrows are analysed in the discussion section. We use the velocity model shown in Figure 6.1b for migrating the measured and retrieved line datasets. The same migration scheme is used here as in the synthetic dataset. The

migration images of the target zone are shown in Figures 6.5a and 6.5b. We can see that artefacts due to internal multiple reflections indicated by red arrows in Figure 6.5a are absent in Figure 6.5b, which is from the retrieved dataset. However, the artefact indicated by the green arrow in Figure 6.5a becomes stronger in Figure 6.5b. Gaps in Figures 6.5a and 6.5b are caused by the limited length of the acquisition similar to those in the modelled dataset.

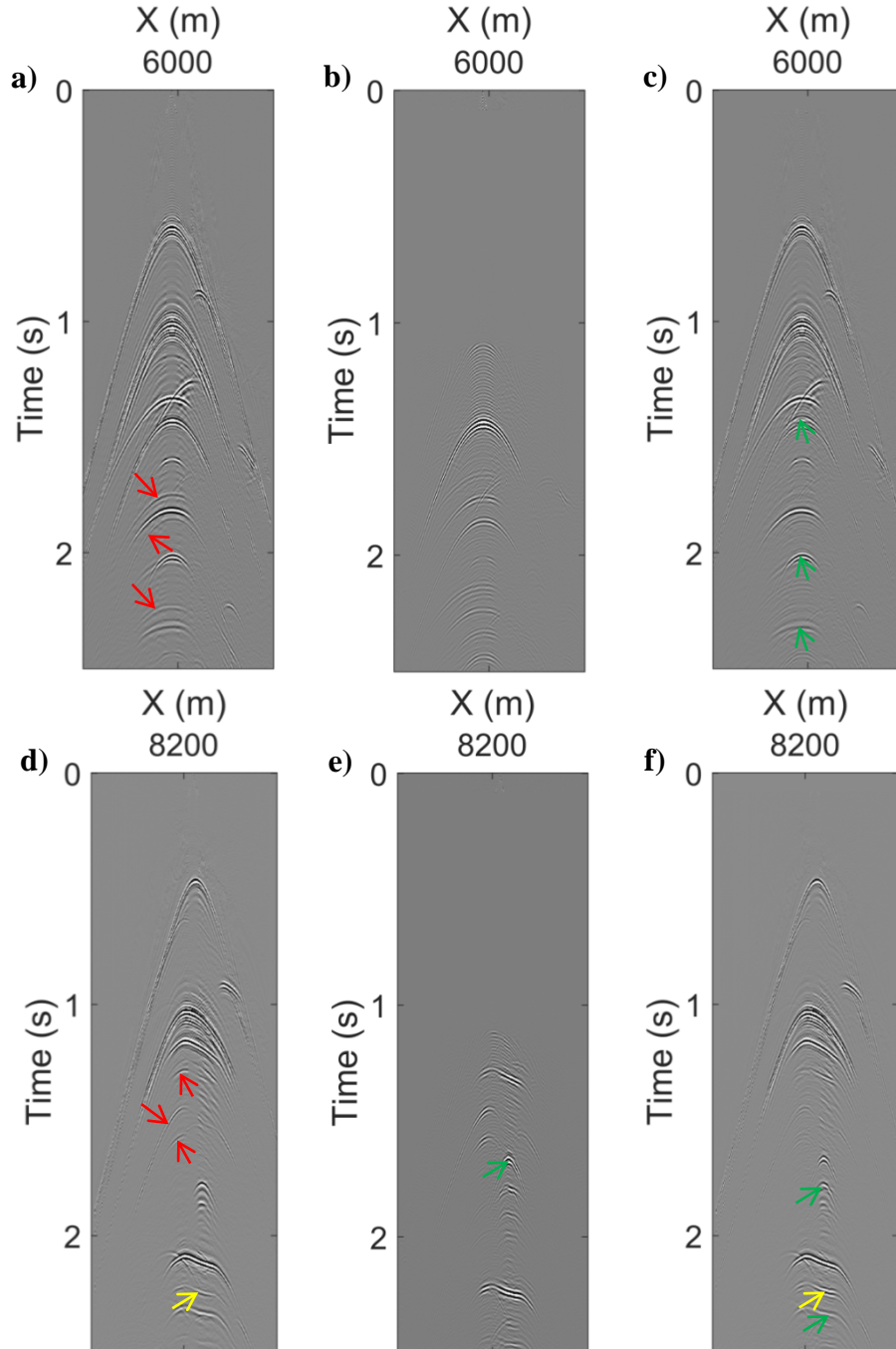


Figure 6.4: The (a) and (d) are original reflection responses from the 2D slice of the Laboratory dataset with source positions indicated by red stars in Figure 6.1b, (b) and (e) are predicted internal multiple reflections by the MME scheme, (c) and (f) are the corresponding multiple-attenuated datasets. Red, yellow and green arrows indicate internal multiple reflections.

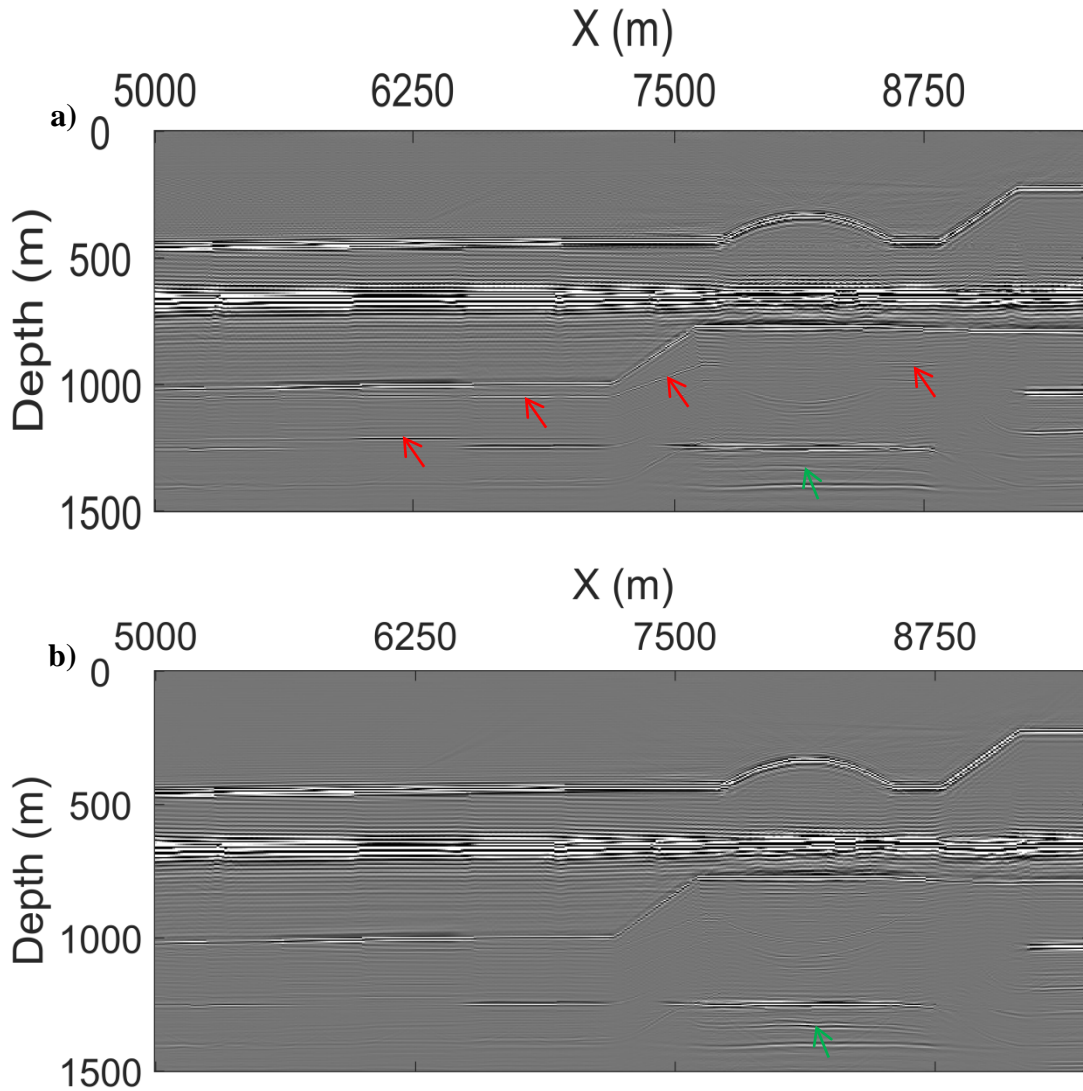


Figure 6.5: (a) The image from the 2D slice of the Laboratory dataset and (b) the image from the resulting dataset of the MME scheme. Red and green arrows in (a) indicate artefacts arising from internal multiple reflections and the green arrow in (b) indicates the artefact that has become stronger than the artefact in the image of the original data.

6.1.3 Discussion

The application of the MME scheme to the computed reflection responses shows that it has excellent performance, all orders of internal multiple reflections are successfully removed as shown in Figure 6.2. The migration image given in Figure 6.3b shows that the structure of the model can be imaged from the resulting dataset of the MME scheme without artefacts arising from internal multiple reflections. This validates the MME scheme for a synthetic model. No model information or adaptive subtraction is used to achieve these results.

The MME scheme successfully predicts all orders of internal multiple reflections in the measured dataset as shown in Figures 6.4b and 6.4e. The resulting R_t , shown in Figures 6.4c

and 6.4f, show that some of the internal multiple reflections are successfully removed. The events indicated by red arrows in Figures 6.4a and 6.4d are absent in Figures 6.4c and 6.4f. The related artefacts in the migration image have disappeared as shown in Figure 6.5. However, some internal multiple reflections are still visible in Figures 6.4c and 6.4f, such as events indicated by green arrows in Figures 6.4c and 6.4f. The polarity of the event indicated by the yellow arrow in Figure 6.4d is changed after the processing as shown in Figure 6.4f. This is caused by the fact that the amplitudes of these events do not conform to the 2D model assumption in processing a line dataset. These amplitude mismatches can be because of 3D effects, and possibly attenuation, such that the predicted events have different amplitudes from actual events in the measured dataset. Adaptive subtraction could be a possible option for the subtraction of internal multiple reflections from the measured Laboratory dataset. However, we prefer not to use it because adaptive subtraction could remove both primary and multiple reflections when they overlap each other.

The event indicated by the green arrow in Figure 6.4e is the internal multiple reflection related to the first and second horizontal reflectors and is successfully predicted by the MME scheme. It is also present in the computed shot gather shown in Figure 6.2c and indicated by the green arrow. Also there it is successfully eliminated by the MME scheme as shown in Figure 6.2d. However, it is not present in the measured data shown in Figure 6.4d but present in the retrieved data shown in Figure 6.4f. This does not necessarily mean that the MME scheme introduces a non-physical event. A possible reason can be that this event is cancelled by other events in the 3D geometry of the Laboratory model such that it is missing in the 2D slice of the Laboratory data.

High-quality pre-processing is crucial for any scheme that uses the data as a filter. The performance of the MME scheme in synthetic and laboratory datasets shows that its success depends on high amplitude fidelity. In the synthetic data all events have correct amplitudes and predicted multiple reflections have same amplitudes as the modelled multiple reflections, such that the MME scheme eliminates them. In the 2D slice of the Laboratory dataset, some internal multiple reflections are still present in the retrieved dataset because of incorrect amplitudes caused by imperfect source wavelet deconvolution, 3D effects, and possibly attenuation.

6.2 Field example

6.2.1 Application of MME scheme

In this subsection, we describe the application of the MME scheme to a 2D field dataset provided by Equinor, which was measured in the Norwegian Sea in 1994. The water bottom (1.5km) is deep enough such that free-surface multiple reflections are well-separated from primary and internal multiple reflections. There are 399 shot gathers and 399 traces per gather in the field dataset. The spatial sampling of the sources and receivers is 25m. For this

field dataset, as illustrated in Davydenko and Verschuur (2018), (1) the direct wave has been muted, (2) near offset traces have been estimated via the parabolic Radon transform (Kabir and Verschuur, 1995), (3) 3D effects have been compensated for by multiplying \sqrt{t} , (4) the source wavelet has been de-convolved and (5) free-surface related multiple reflections have been attenuated by SRME.

Figure 6.6 shows a macro velocity model of the target basin where the dataset is acquired. This model is not used for internal multiple reflection elimination and merely serves to illustrate the environment. The yellow box marks the target zone which is imaged. Red stars indicate the source position of the three shot gathers (convolved with 20Hz Ricker wavelet) shown in Figures 6.7a, 6.7c and 6.7e. Note that, between 2.5s and 3.5s, internal multiple reflections indicated by red arrows are present. We use the MME scheme to remove internal multiple reflections from the field dataset. The multiple-attenuated gathers convolved with 20Hz Ricker wavelet are given in Figures 6.7b, 6.7d and 6.7f. These results show that internal multiple reflections, indicated by red arrows in Figures 6.7a, 6.7c and 6.7e, are successfully removed or attenuated in the resulting gathers shown in Figures 6.7b, 6.7d and 6.7f. Note that the events indicated by green arrows in Figures 6.7b and 6.7d are not visibly present in Figures 6.7a and 6.7c. It does not necessarily imply that the MME scheme introduces new events. It can be caused by the fact that these two events are cancelled by internal multiple reflections in the original shot gathers and after internal multiple reflection elimination, these cancelled primary reflections are recovered in the resulting shot gathers. No model information or adaptive subtraction is used in the implementation of the MME scheme, such that masked primary reflections can be recovered.

We use the macro velocity model shown in Figure 6.6 in a one-way wave equation migration scheme to migrate both datasets before and after internal multiple reflection elimination. The resulting images are given in Figures 6.8a and 6.8b. The red boxes numbered 1, 2 and 3 mark the zones where internal multiple reflection related artefacts are visibly present in Figure 6.8a and almost absent in Figure 6.8b. We give the magnified portion of zones numbered 1, 2 and 3 separately in Figures 6.9, 6.10 and 6.11 for detailed comparison. In Figure 6.9, the internal multiple reflection related artefact, indicated by the red arrow in Figure 6.9a, is effectively attenuated with weak residual as shown in Figure 6.9b. In Figure 6.10, most artefacts arising from overburden multiple scatterings are successfully predicted by the MME scheme and, after the processing, most of them are successfully removed as shown in Figure 6.10b. Similarly, most artefacts due to internal multiple reflections are successfully predicted and, correspondingly, they are removed in the image from the multiple-attenuated dataset as shown in Figure 6.11b. Besides, the continuity of structures indicated by green arrows numbered 1 and 2 has been improved and structures numbered 3 and 4 have been successfully recovered. This is due to the fact that the cancelled primary reflections are recovered after internal multiple reflection elimination by the MME scheme. Especially in the zones indicated by green boxes in Figures 6.11a and 6.11b, most artefacts due to internal multiple reflections have been successfully removed and the continuity of the synclinal reflectors has been greatly improved.

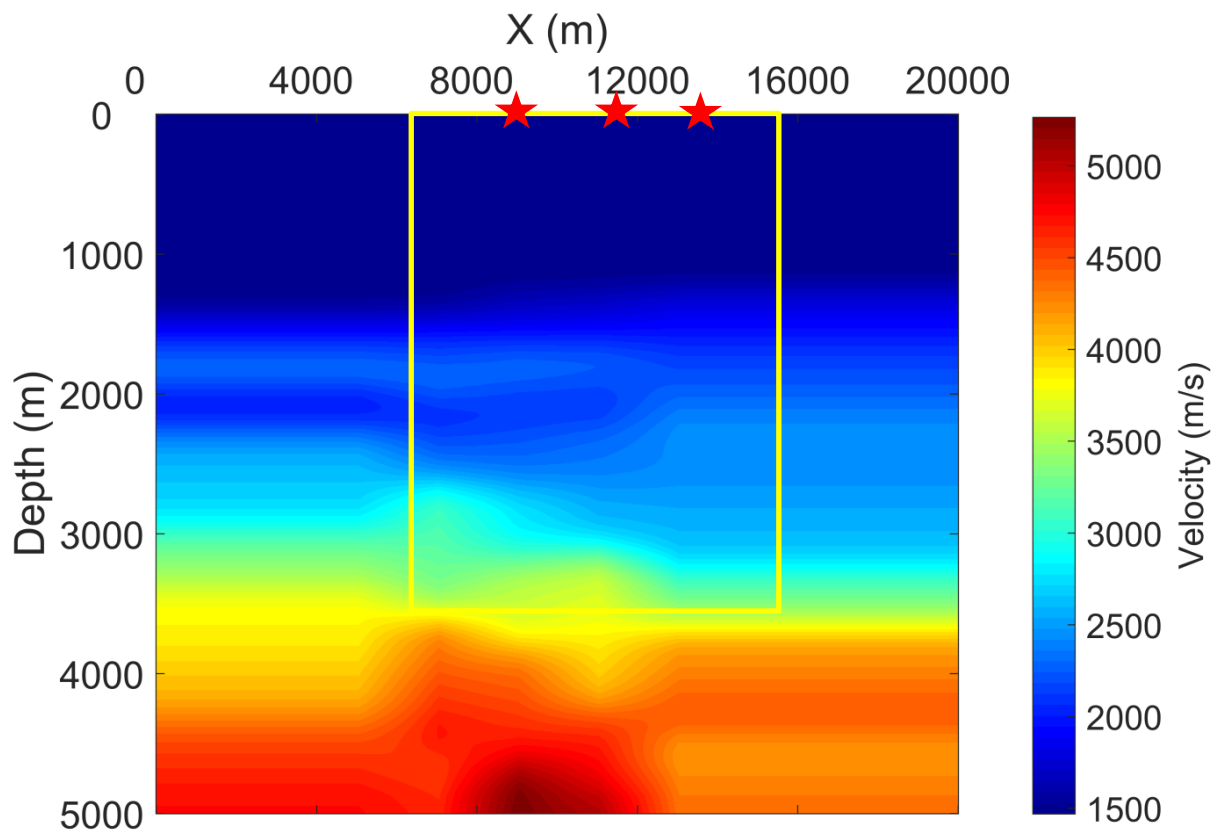
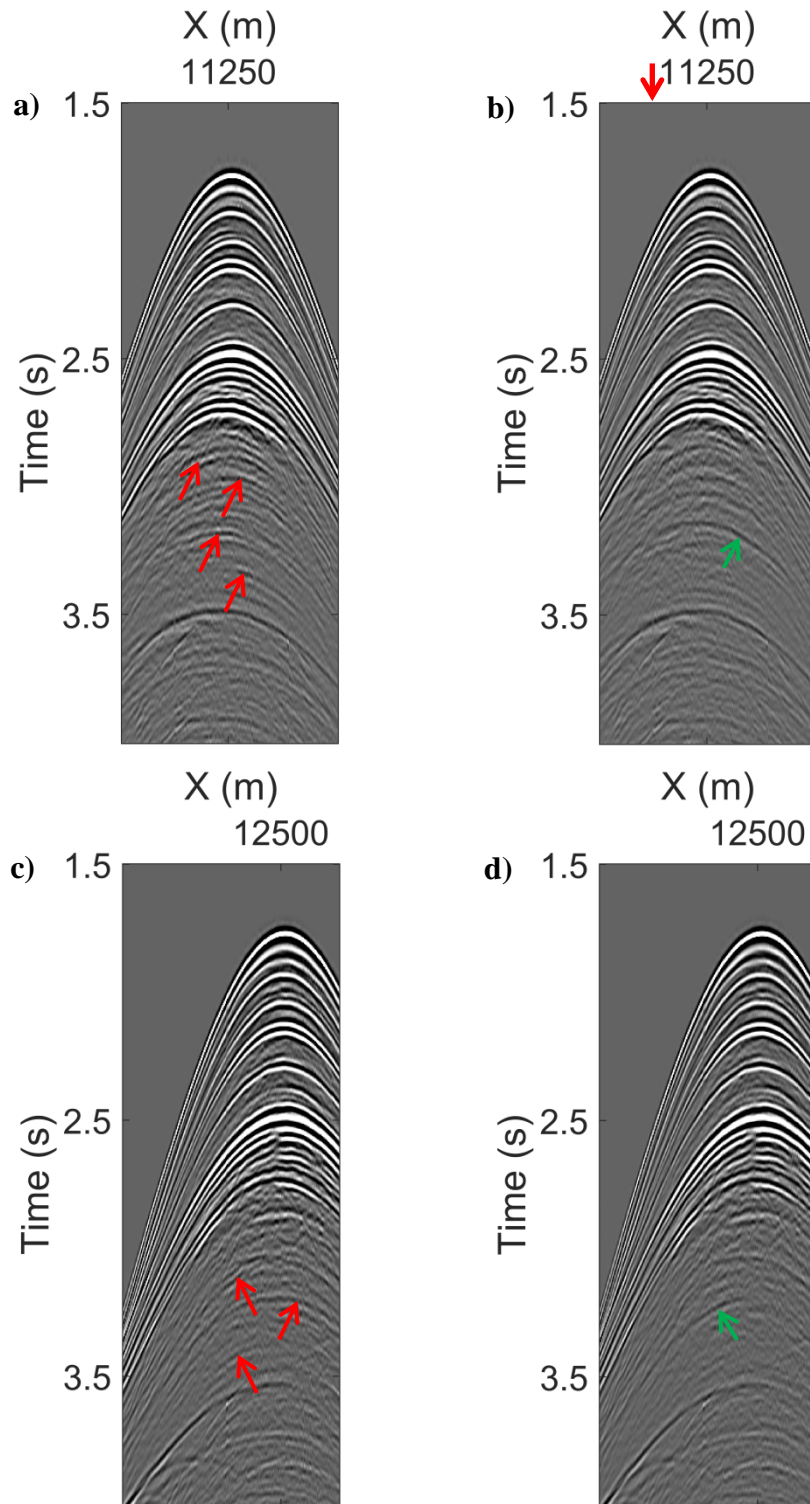


Figure 6.6: The macro velocity model that will be used to migrate the datasets before and after internal multiple reflection elimination. Red stars indicate source position of the shot gathers shown in Figure 6.7, the yellow box marks the target zone which is imaged.



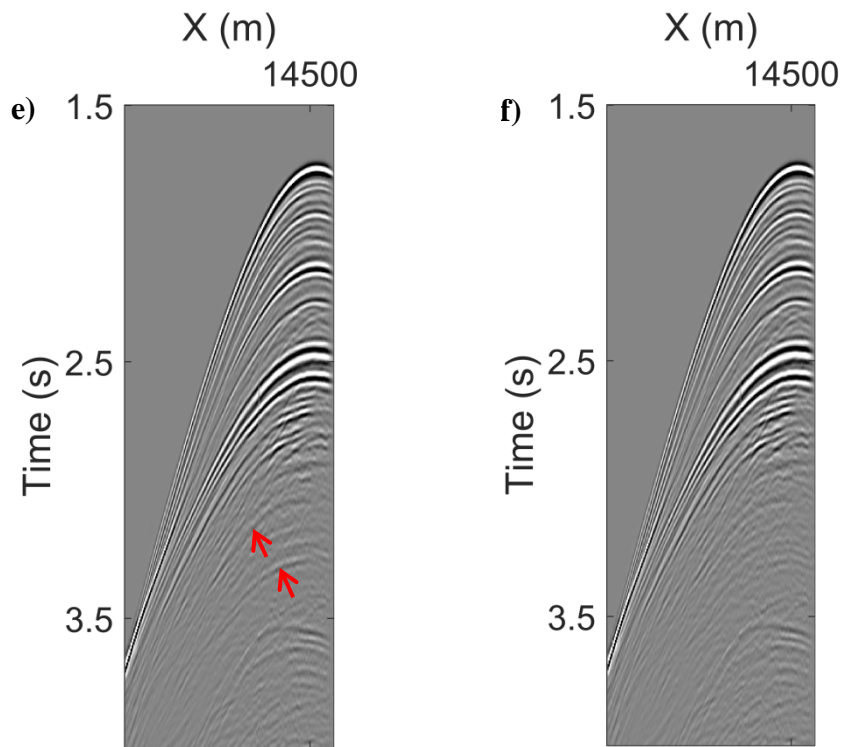


Figure 6.7: The (a), (c) and (e) are original shot gathers; (b), (d) and (f) are the corresponding multiple-eliminated datasets. Red arrows in (a), (c) and (e) indicate internal multiple reflections, green arrows in (b) and (d) indicate primary reflections recovered after the processing. The red arrow in (b) indicates the trace which will be used to compare the difference between MME and T-MME schemes in Figure 6.13.

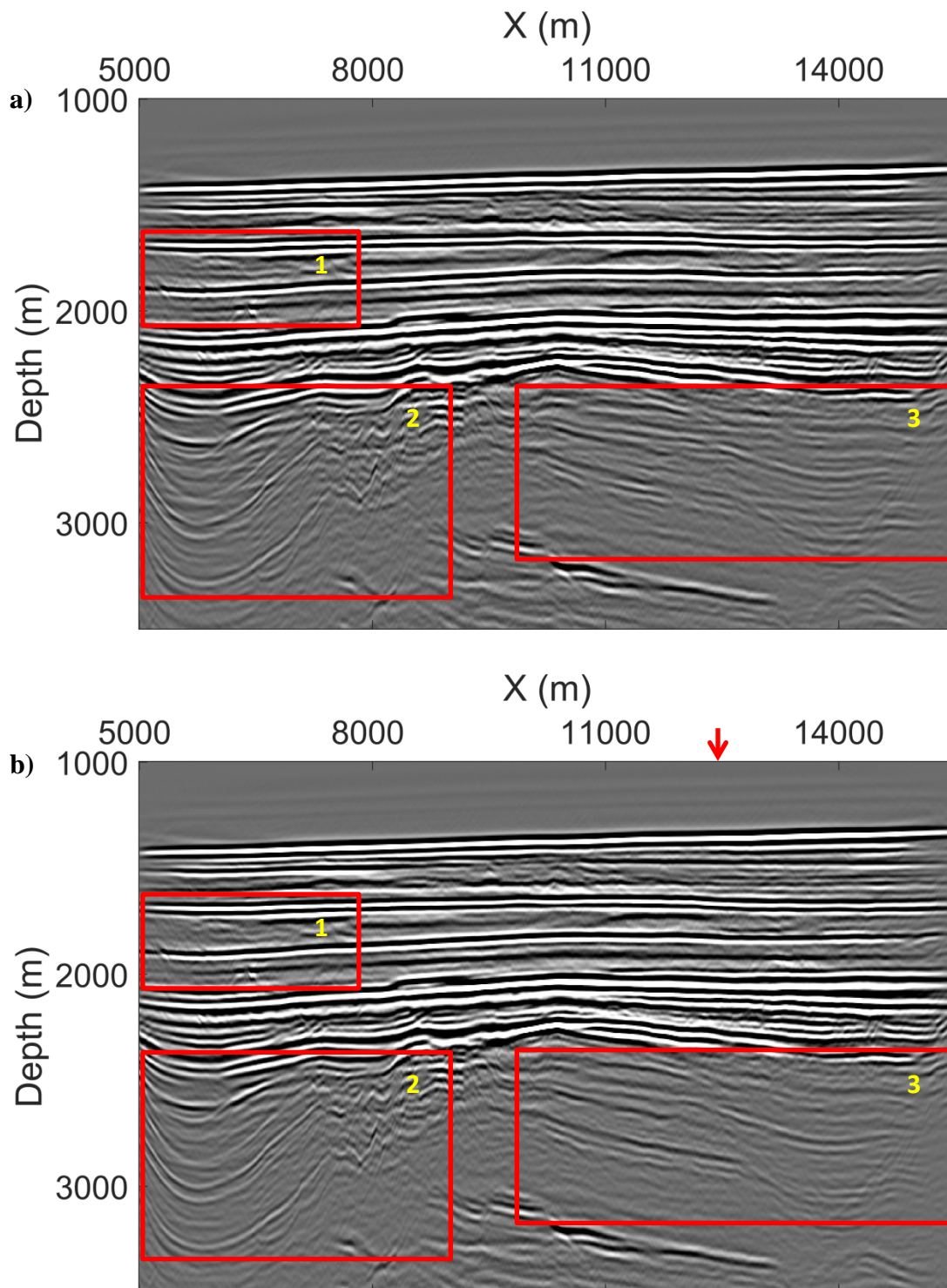


Figure 6.8: (a) The image from the original measured field dataset and (b) the image from the resulting dataset of the MME scheme. The numbered red boxes mark zones which are magnified in Figures 6.9, 6.10 and 6.11 for detailed comparison. Red arrow in (b) indicates the trace which will be used for comparison in Figure 6.18.

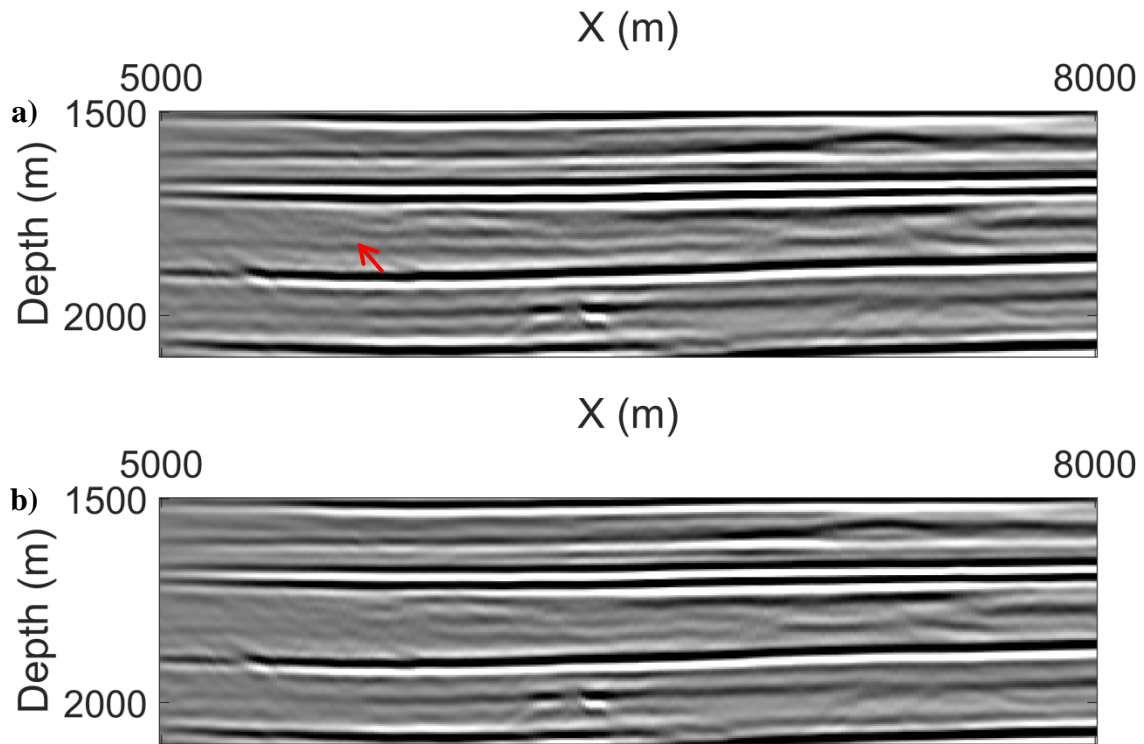


Figure 6.9: (a) The magnified portion of the zone 1 in Figure 6.8a and (b) the magnified portion of the zone 1 in Figure 6.8b. The red arrow indicates the artefact due to internal multiple reflection, which is attenuated after the processing by the MME scheme.

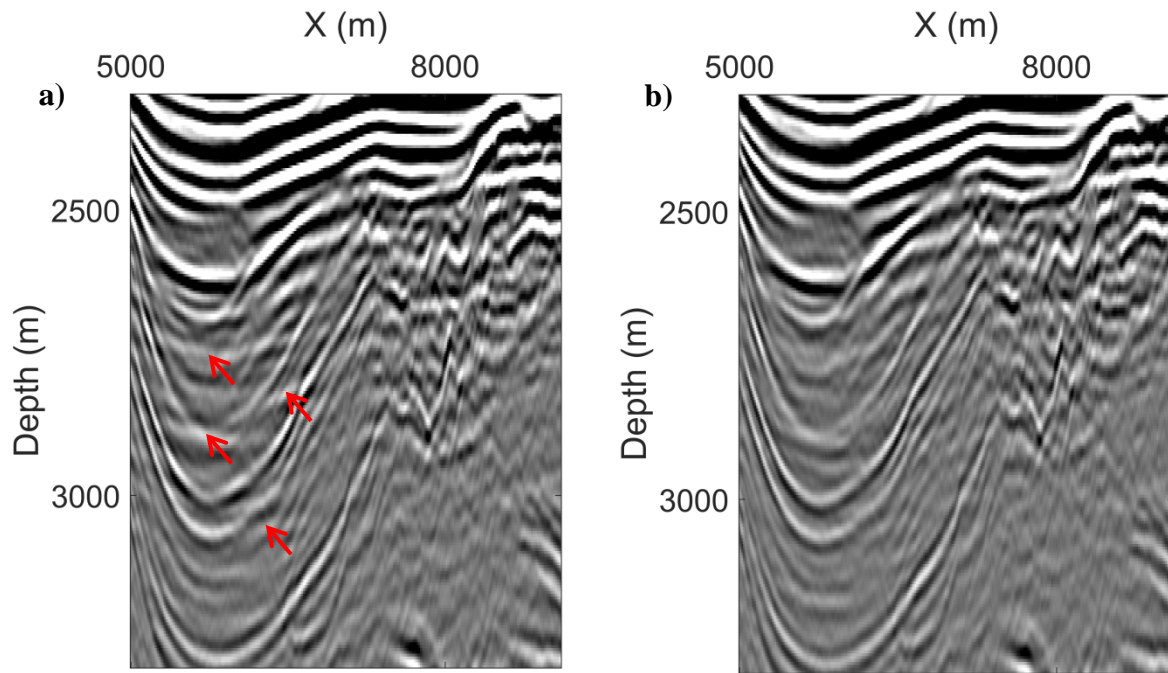


Figure 6.10: (a) The magnified portion of the zone 2 in Figure 6.8a and (b) the magnified portion of the zone 2 in Figure 6.8b. The red arrows indicate artefacts due to internal multiple reflections, which are removed after the processing by the MME scheme.

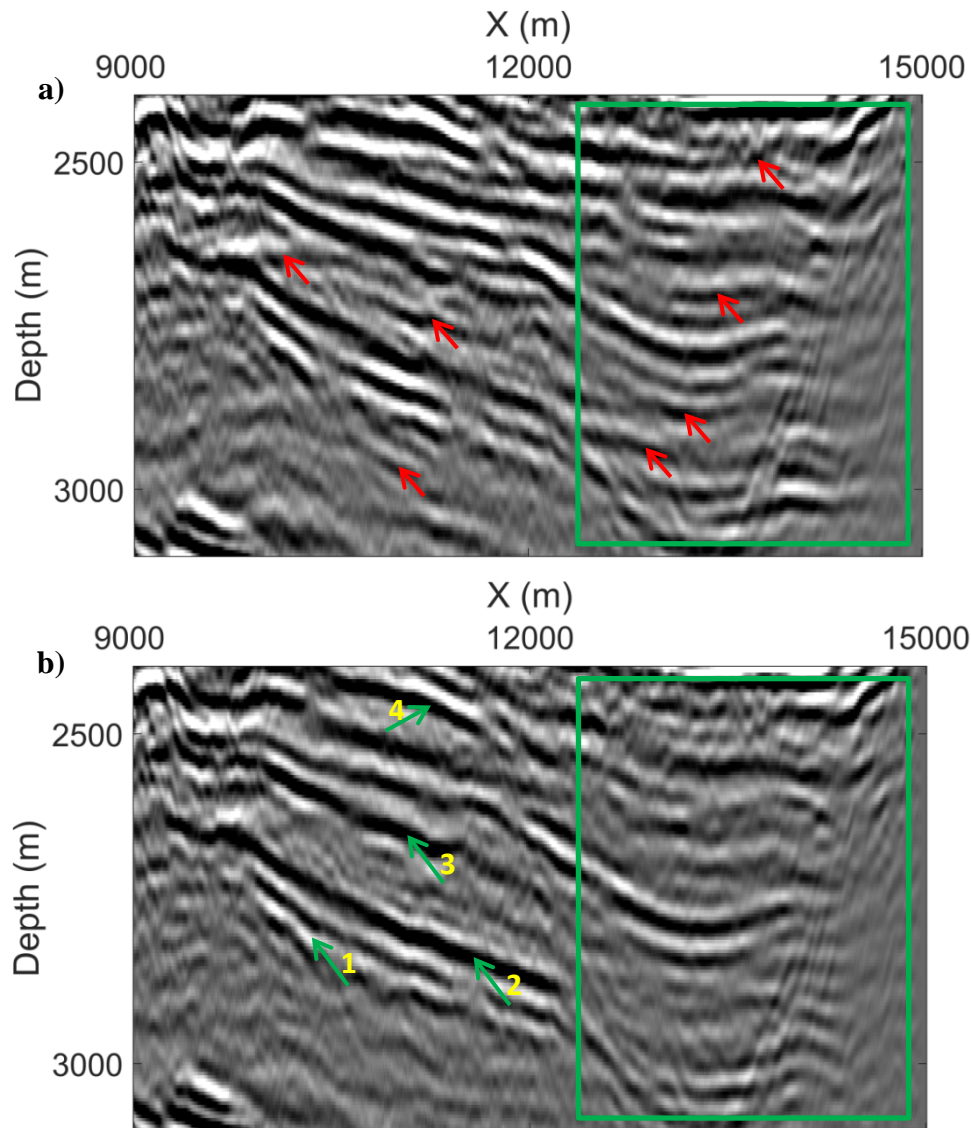


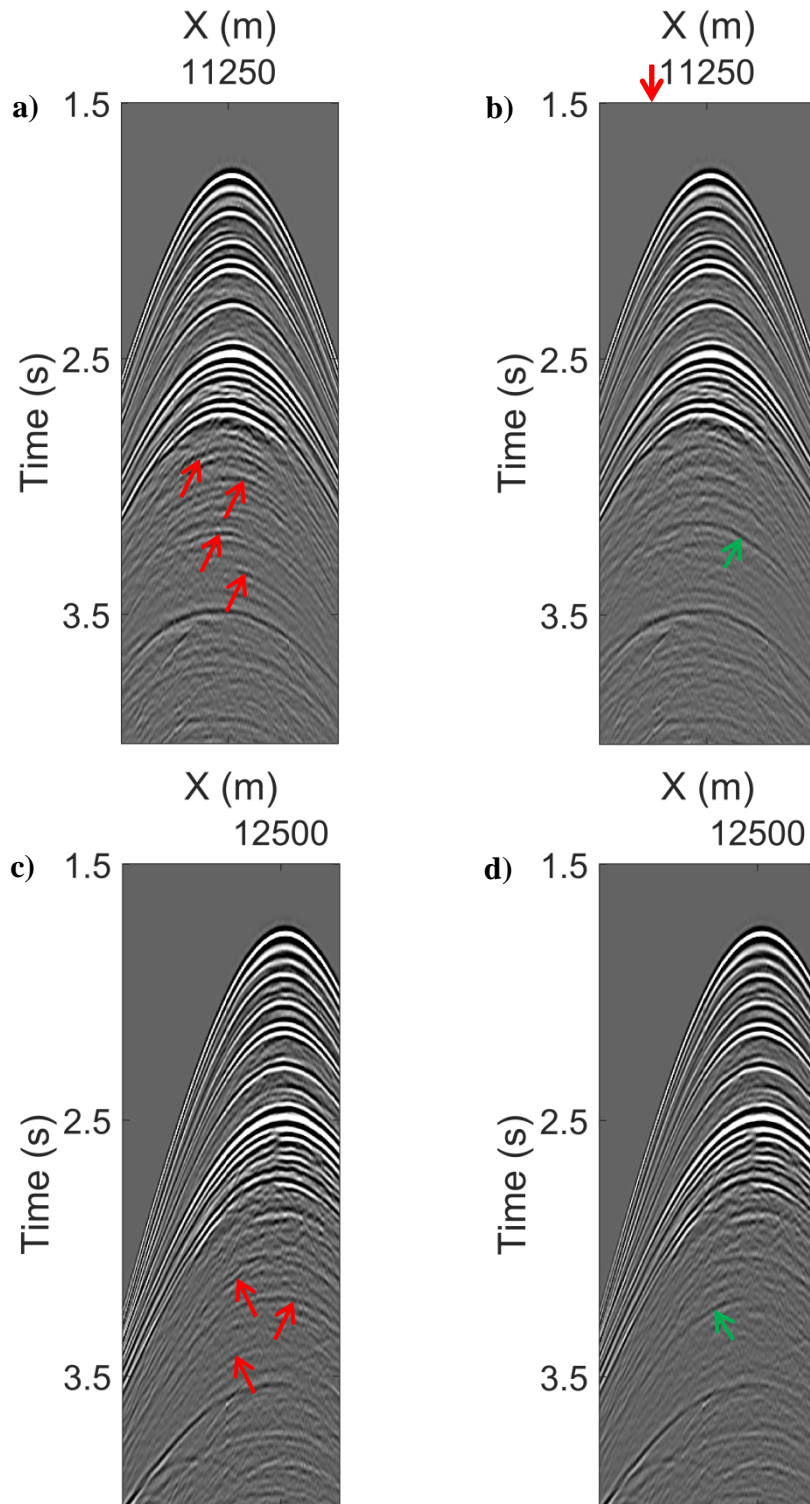
Figure 6.11: (a) The magnified portion of the zone 3 in Figure 6.8a and (b) the magnified portion of the zone 3 in Figure 6.8b. The red arrows indicate artefacts due to internal multiple reflections. Green arrows indicate structures recovered and the green boxes indicate the zone where most artefacts are removed by the MME scheme.

6.2.2 Application of T-MME scheme

We apply the T-MME scheme to the same field dataset to remove internal multiple reflections and compensate for transmission losses in primary reflections. The same shot gathers are used here to illustrate the performance. Figures 6.12a, 6.12c and 6.12e give the original shot gathers convolved with 20Hz Ricker wavelet (source positions are indicated by red stars in Figure 6.6) and multiple-eliminated gathers convolved with 20Hz Ricker wavelet are shown in Figures 6.12b, 6.12d and 6.12f. These results show that internal multiple reflections, indicated by red arrows in Figures 6.12a, 6.12c and 6.12e, are removed or attenuated in the resulting gathers shown in Figures 6.12b, 6.12d and 6.12f. Similarly, the

events indicated by green arrows in Figures 6.12b and 6.12d are not visibly present in Figures 6.12a and 6.12c but recovered after the processing by T-MME scheme. The nonzero-offset traces indicated by red arrows in Figures 6.12b and 6.7b are picked and shown in Figure 6.13. It can be seen that the trace from Figure 6.12b has higher amplitude because of the transmission compensation (the MME scheme only removes internal multiple reflections without touching primary reflections). Both traces have been normalised by the same factor.

We use the macro velocity model given in Figure 6.6 to migrate the dataset retrieved by the T-MME scheme. Still, the one-way wave equation migration scheme is used. The resulting image is given in Figure 6.14b. Compared with the image given in Figure 6.14a, which is from the original dataset, internal multiple reflection related artefacts are successfully removed in zones marked by red boxes numbered 1, 2 and 3. The magnified portions of marked zones numbered 1, 2 and 3 are given separately in Figures 6.15, 6.16 and 6.17 for detailed comparison. Note that, similarly, the internal multiple reflection related artefacts have disappeared from the image from the multiple-attenuated dataset as shown in Figures 6.15 and 6.16. In Figure 6.17, most artefacts due to internal multiple reflections, indicated by red arrows in Figure 6.17a, are successfully removed in the image from the multiple-attenuated dataset as shown in Figure 6.17b. Besides, the continuity of structures indicated by green arrows numbered 1 and 2 has also been improved and structures numbered 3 and 4 have been successfully recovered. We pick traces indicated by red arrows in Figures 6.8b and 6.14b and show the comparison in Figure 6.18. Because of the compensation for transmission losses in primary reflections, the trace from Figure 6.14b has higher amplitude. This validates the effectiveness of the T-MME scheme for transmission losses compensation in primary reflections. Both traces have been normalised by the same factor.



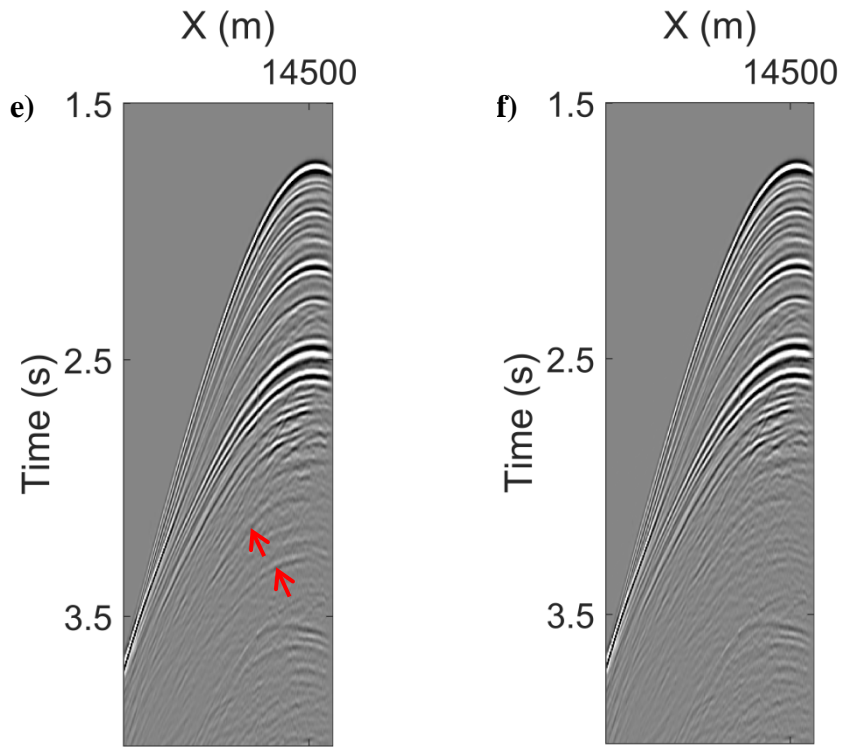


Figure 6.12: The (a), (c) and (e) are original shot gathers; (b), (d) and (f) are the corresponding multiple-eliminated datasets. Red arrows in (a), (c) and (e) indicate internal multiple reflections, green arrows in (b) and (d) indicate primary reflections recovered after the processing. Red arrow in (b) indicates the trace which will be used for comparison in Figure 6.13.

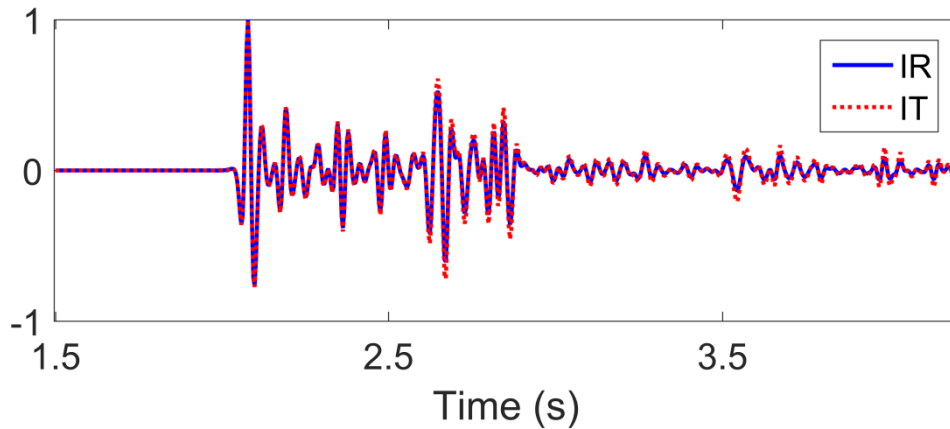


Figure 6.13: The comparison of traces from Figures 6.7b and 6.12b (indicated by red arrows in both Figures). IR indicates trace from Figure 6.7b and IT indicates trace from Figure 6.12b.

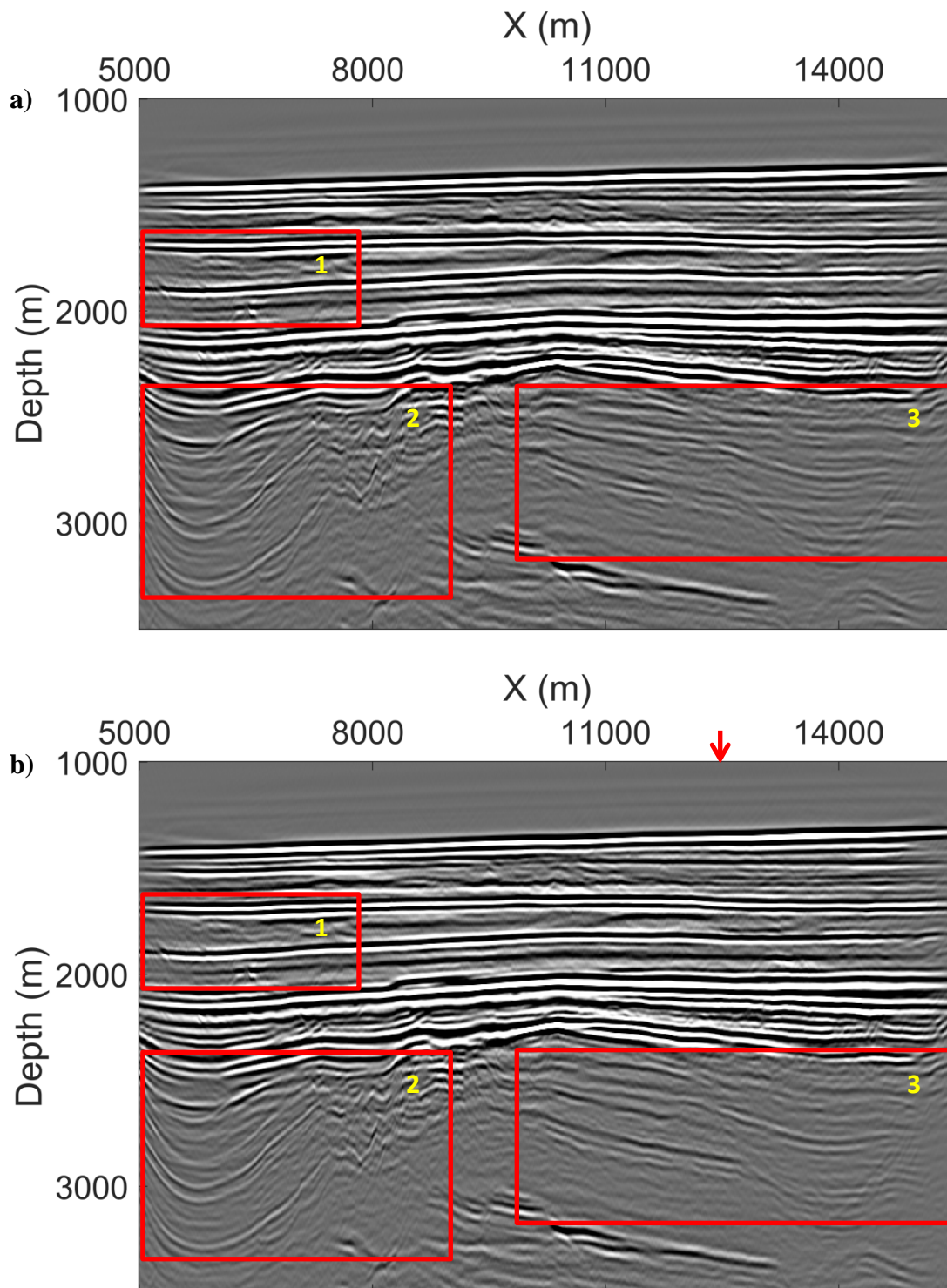


Figure 6.14: (a) The image from the original measured field dataset and (b) the image from the resulting dataset of the T-MME scheme. The numbered red boxes mark zones which are magnified in Figures 6.15, 6.16 and 6.17 for detailed comparison. Red arrow in (b) indicates the trace which will be used for comparison in Figure 6.18.

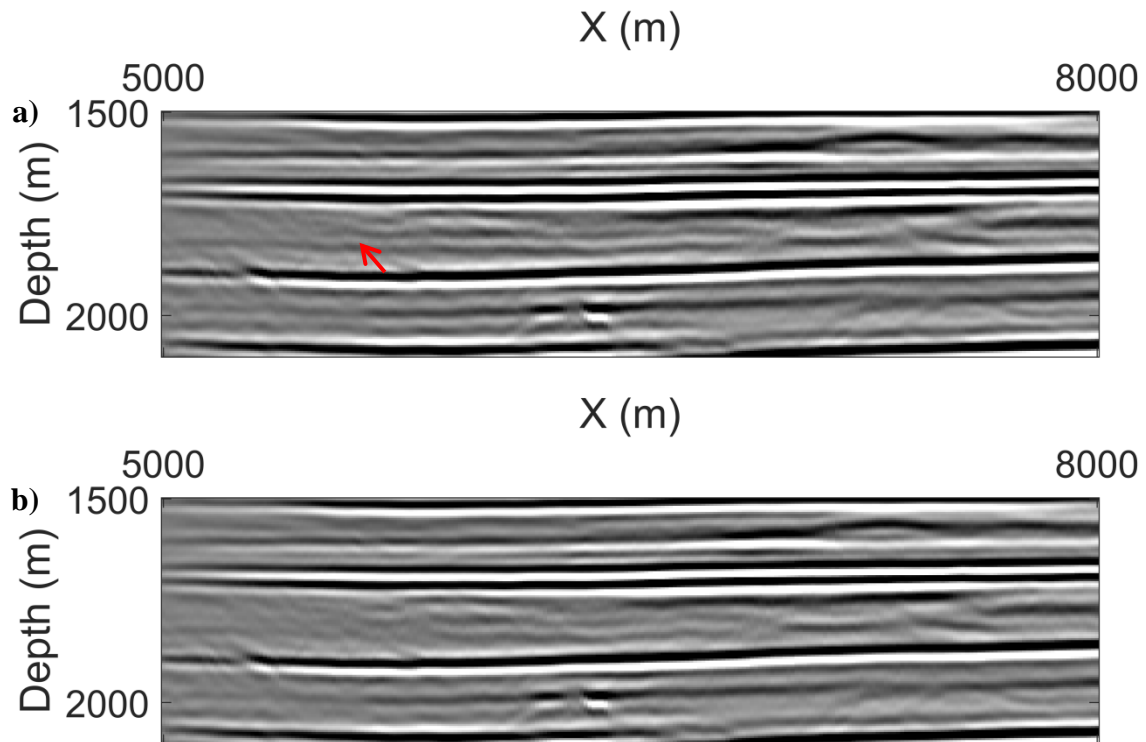


Figure 6.15: (a) The magnified portion of the zone 1 in Figure 6.14a and (b) the magnified portion of the zone 1 in Figure 6.14b. The red arrow indicates the artefact due to internal multiple reflection, which is attenuated after the processing by the T-MME scheme.

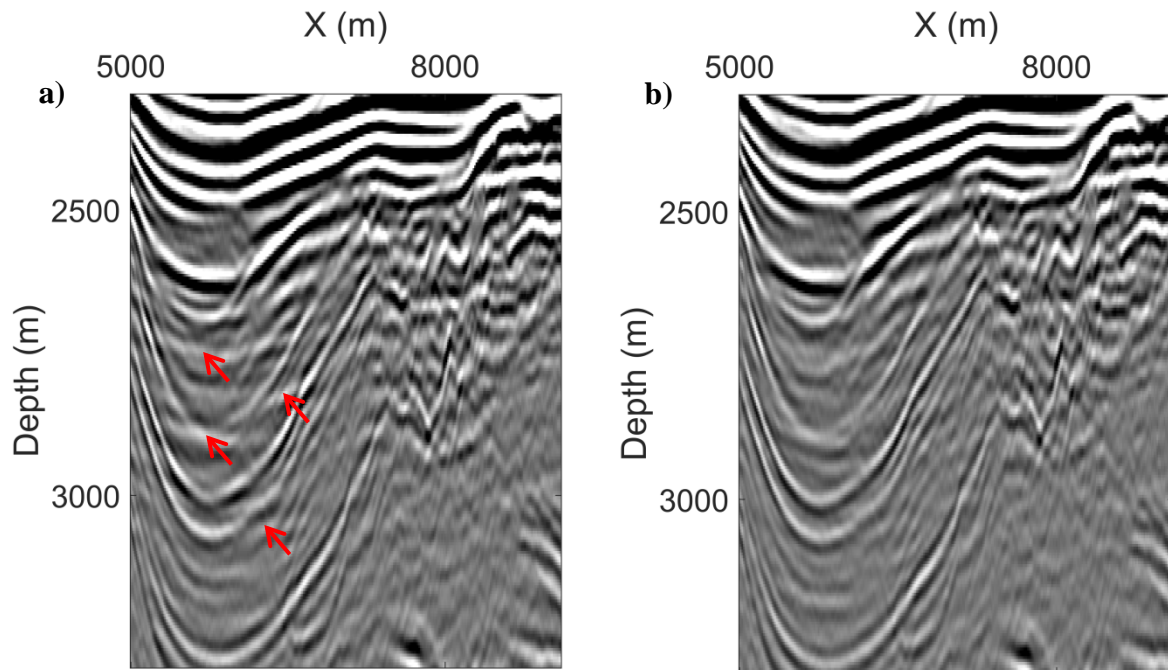


Figure 6.16: (a) The magnified portion of the zone 2 in Figure 6.14a and (b) the magnified portion of the zone 2 in Figure 6.14b. The red arrows indicate artefacts due to internal multiple reflections, which are removed after the processing by the T-MME scheme.

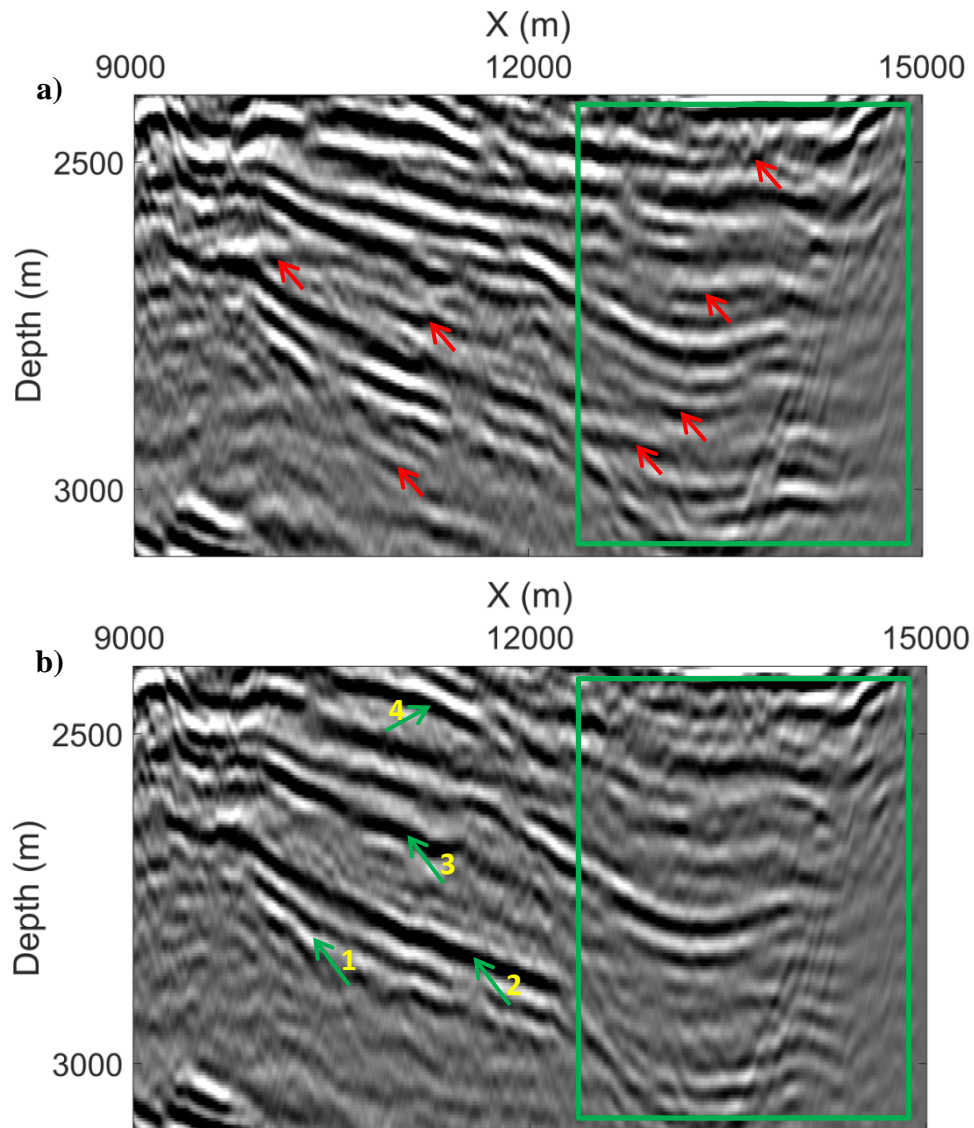


Figure 6.17: (a) The magnified portion of the zone 3 in Figure 6.14a and (b) the magnified portion of the zone 3 in Figure 6.14b. The red arrows indicate artefacts due to internal multiple reflections. Green arrows indicate structures recovered and the green boxes indicate the zone where most artefacts are removed by the T-MME scheme.

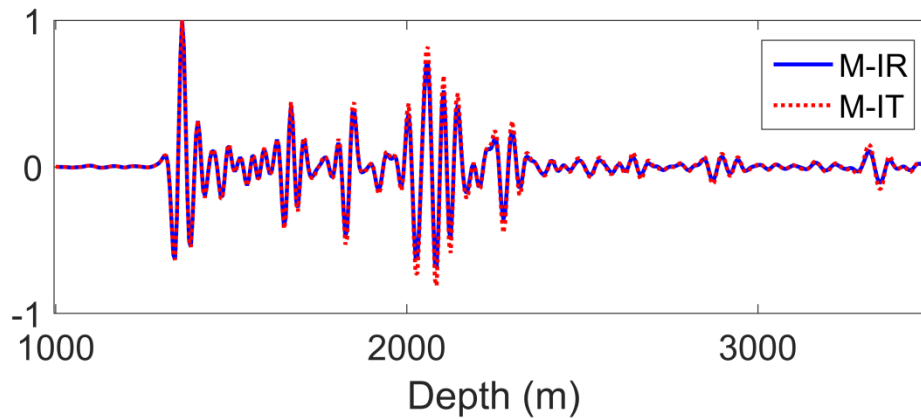


Figure 6.18: The comparison of traces from Figures 6.8b and 6.14b (indicated by red arrows in both Figures). M-IR indicates trace from Figure 6.8b and M-IT indicates trace from Figure 6.14b.

6.2.3 Discussions

As shown in the field example section, the MME and T-MME schemes successfully remove or attenuate most internal multiple reflections. Several primary reflections cancelled by internal multiple reflections are recovered and, correspondingly, the related structures are present in the image as shown in Figures 6.11 and 6.17. The transmission losses in primary reflections are compensated for by the T-MME scheme. From previous study in [Verschuur and Berkhout \(2005\)](#), where the IME scheme was applied to the same field dataset, most internal multiple reflections removed by the MME and T-MME schemes were effectively attenuated by the IME scheme. However, the cancelled primary reflections indicated by the green arrows in Figures 6.7 and 6.12 could not be recovered with the IME scheme, because of adaptive subtraction which is based on the minimum-energy criterion. Therefore, we surmise that other schemes that apply adaptive subtraction, such as ISS based schemes, can possibly attenuate internal multiple reflections which are removed by the MME and T-MME schemes, but cannot deal with the case where internal multiple reflections overlap with primary reflections.

The 2D field dataset used here as an example, is measured from an area with a deep ocean bottom. The deep water helps in reducing the mismatch in amplitude of the 2D MME and T-MME schemes that is necessarily applied to a 3D line dataset. The second advantage of deep water is the fact that the shallow part of the measured dataset is free from free-surface multiple reflections. High-quality de-noising, deghosting, source wavelet deconvolution and near offset traces estimation are necessary for the successful application of the MME and T-MME schemes. When the input dataset has severe amplitude problems, the performance of the MME and T-MME schemes are limited. In the laboratory data section, the MME scheme was applied to a measured laboratory dataset with variable quality. Because of amplitude errors in some parts of data, some internal multiple reflections were effectively attenuated or removed by the MME scheme, while some were stronger and had opposite polarity after the

processing. These caused artefacts in the computed image. Combining the performance in the Laboratory example and the field example here, we conclude that high-quality pre-processing is crucial for the success of the MME and T-MME schemes.

6.3 Conclusions

We have applied the MME and T-MME schemes to measured laboratory and field datasets to test the performance. No model information or adaptive subtraction is used in the implementation. The laboratory data example shows that several internal multiple reflections are successfully removed or attenuated, but some remnant multiple reflections remained. The field example shows that most internal multiple reflections are successfully eliminated and, because of the independence from adaptive subtraction, the primary reflections which are cancelled by internal multiple reflections are recovered by the MME and T-MME schemes. Given the overall successful application to the Laboratory and field datasets, we think the MME and T-MME schemes are appropriate methods for multiple-free dataset retrieval.

References

- Blacquiere, G., A. W. F. Volker, and L. Ongkiehong, 1999, 3-D physical modeling for acquisition geometry studies: 69th Annual Meeting, SEG, Expanded Abstracts, 1212–1215.
- Davydenko, M., and D. J. Verschuur, 2018, Including and using internal multiples in closed-loop imaging—Field data examples: *Geophysics*, **83**, no. 4, R297–R305.
- Kabir, M. M. N., and D. J. Verschuur, 1995, Restoration of missing offsets by parabolic radon transform: *Geophysical Prospecting*, **43**, 347–368.
- Koek, E. A., G. Faber, and A. J. Berkhout, 1995, 3-D data acquisition research with the Delft physical modeling facility: 65th Annual Meeting, SEG, Expanded Abstracts, 747–748.
- Verschuur, D. J., and A. Berkhout, 2005, Removal of internal multiples with the common-focus-point (CFP) approach: Part 2—Application strategies and data examples: *Geophysics*, **70**, no. 3, V61–V72.
- Wapenaar, K., J. Brackenhoff, J. Thorbecke, J. van der Neut, E. Slob, and E. Verschuur, 2018, Virtual acoustics in inhomogeneous media with single-sided access: *Scientific Reports*, **8**, 2497.

General Conclusions

The aim of this thesis is to investigate the process of forming a subsurface image from acoustic reflection data without artefacts due to multiple reflections. Two kinds of strategies are proposed. The first strategy works in imaging domain and an artefact-free image of the subsurface can be retrieved with the same macro velocity model as used for conventional migration schemes. This requires to first build a smooth velocity model from the reflection data. This model is used to estimate a first arrival to any location in the subsurface. Then the Marchenko equations are solved, and the artefact-free image is formed. The second strategy works directly on the data. Two multiple reflection elimination schemes are derived to obtain a multiple-free dataset. Both can be applied before or after free surface multiple reflection elimination. Here, first the multiple reflections are eliminated from the reflection data without any subsurface information or adaptive subtraction. The smooth velocity model is built from the data with only primary reflections, which are then used to compute the artefact-free subsurface image. Both strategies can be implemented in routine industry processing workflows. The second strategy is advantageous for velocity model building. In practice, this may lead to a higher quality image than would be obtained following the first strategy. Both strategies were applied to synthetic datasets, whereas the two methods in the second strategy were applied to laboratory and field datasets as well.

In Chapter 2, we have shown that an artefact-free reverse-time migration (RTM) image can be constructed based on a revised Marchenko scheme. To use RTM directly in Marchenko redatuming, a modified time truncation operator was designed. This allowed using the standard wavefield extrapolation operator in the Marchenko equations. An artefact-free RTM scheme has been derived, which can be used to image the medium without artefacts arising from internal multiple reflections. The new migration scheme uses the same macro-velocity model as the conventional RTM scheme. The constructed image does not contain artefacts because the data acts as a filter with time truncations to remove artefacts generated by the conventional RTM scheme. When the velocity model is accurate, the image is nearly perfect as shown with a synthetic example.

In Chapter 3, we have presented the MME and T-MME schemes for internal multiple reflection elimination in the two-way travel time domain. The MME scheme focuses only on internal multiple reflection elimination without touching primary reflections. The T-MME scheme removes internal multiple reflections and compensates for transmission effects in the

retrieved primary reflections. For both schemes, the measured dataset is its own filter with a time truncation that is a free parameter for which reason the method is fully automated and works without model information or adaptive subtraction. The synthetic examples illustrate the success of both schemes. The limitations are explored, and the analysis shows that scattered waves and refracted waves as well as thin layer effects are partially beyond the capability of both methods.

In Chapter 4, we have extended the MME and T-MME schemes to account for free-surface related multiple reflections. Thus, the extended MME and T-MME schemes remove free-surface and internal multiple reflections in one step, while the amplitudes of retrieved primary reflections by extended T-MME scheme are compensated for transmission effects. Because the introduction of a free surface does not increase the number of unknowns, the implementation of both extended schemes does not require model information or adaptive subtraction. The synthetic examples show that the extended MME scheme effectively removes free-surface and internal multiple reflections, and extended T-MME scheme removes multiple reflections and compensates for transmission losses in primary reflections in one step. Both extended schemes can be of interest in exploration geophysics for retrieving datasets with only primary reflections. These are suitable for velocity model building, artefact-free migration, and inversion.

In Chapter 5, we developed a fast implementation of T-MME and extended T-MME schemes by using the projected focusing functions computed for a certain time instant as an initial estimate for the next time instant. This reduces the computational cost in our examples by an order of magnitude. The same limitations apply to the fast implementation as for the conventional implementation of both schemes because the fast implementation modifies the starting point, but not the equation that is solved. The MME and extended MME schemes can be implemented in the same way and we did not repeat it in this Chapter.

In Chapter 6, we applied the MME scheme to a measured laboratory dataset to test the performance and compared the results with results from synthetic data based on an estimate of the same model. The results show that several internal multiple reflections are successfully removed or attenuated, but some remnant multiple reflections remained. In one location a multiple was predicted that was present in the computed data but not in the measured data. It is likely that the absence of this multiple in the measured data comes from 3D effects not captured in the 2D model slice used for modelling the 2D dataset. Using a 2D scheme on 3D line data always comes with amplitude difficulties. The MME and T-MME schemes were also applied to a measured field dataset to evaluate the performance. The field example shows that most internal multiple reflections are successfully eliminated and, because of the independence from adaptive subtraction, the primary reflections which are masked or cancelled by internal multiple reflections are recovered by the MME and T-MME schemes. No model information or adaptive subtraction is required for the implementation of both schemes. Given the successful application to the laboratory and field datasets, we think that the MME and T-MME schemes are appropriate methods for removal of internal multiple reflections in exploration geophysics.

All of the proposed schemes for dealing with the very challenging topic “multiple reflection” in this thesis have been illustrated by synthetic and measured examples in detail and the success has been validated. We expect these schemes can be widely used in seismic reflection imaging and monitoring of structures and processes in the Earth’s interior.

Acknowledgments

This work is a part of the Open Technology Program with project number 13939, which is financed by NWO, Domain Applied and Engineering Sciences.

During the last four years, the accompany of all individuals and numerous unforgettable memories make me realise that I would not be where I am today without the help of my family, friends, and colleagues. So, I would like to express my sincere gratitude to everyone who has helped or influenced me in my research and daily life.

First and foremost, I would like to thank my promoter and daily supervisor Prof. Evert Slob for your invaluable guidance and support. I vividly remember the great joy I experienced when you sent me the e-mail that you would like to offer me a PhD position on the project “Marchenko imaging and monitoring of geophysical reflection data”. I remember those Tuesdays when I came to your office with some naïve ideas, you kindly listened and taught me how to mathematically understand Marchenko imaging. I learned a lot from you, particularly, the theory of Marchenko redatuming, how to write a scientific Journal paper and how to nicely present our work at conferences. You gave me a lot freedom to do my research based on my thought. I am proud to be your student and to have been supervised by you. I look forward to our continued collaboration in the future.

I would also like to thank Prof. Kees Wapenaar for your kind support, especially for your review of my journal manuscripts. Your positive comments always help me a lot for improving my publications. When we were discussing, I was deeply impressed by your very strong theoretical knowledge and scientific integrity. Your course (advanced wave theory for geoscientist) helped me learn a lot. I am honoured to be a member of your group.

Special gratitude goes to Jan Thorbecke and Joost van der Neut. I actually see you both also as my supervisors. Let me start by acknowledging Joost van der Neut. Joost, you have a very friendly and unselfish personality. You helped me a lot, especially at the beginning of my PhD, to understand what the Marchenko redatuming is. It was a great motivation talking to you. You are the one who opened the door of Marchenko theory to me. To go to China for a travel is a plan we talked several times with Myrna as well and I hope us three will have a nice journey. Also, I wish you can achieve your dream to be a teacher soon. Jan, you are also very friendly and unselfish. Your regular Marchenko redatuming code helped me a lot and made my research much easier. Your review of my journal manuscripts and positive comments are always helpful for improving my publications. I greatly appreciate everything you have done for me in the past four years. I look forward to continuing working with you in the future.

Gratitude also goes to Eric Verschuur for offering the laboratory and field dataset used in this thesis. These examples make the thesis complete.

I would also like to thank the members of the User Committee of my project: Arie Verdel, Jesper Spetzler, Peter Mesdag, Marcin Dukalski, Koos de Vos, Vsevolod Kovalenko, Roald van Borselen, Rob Hegge, Alex Kirichek and Elisa Guasti, your comments helped me a lot during past four years.

Now it is time for me to thank my cheerful colleagues. Myrna, Joeri and Chris, I will never forget our amazing travel to Switzerland and to Cambridge. I had a lot of discussions with Giovanni and Carlos about some crazy ideas and you both always kindly explained to me why it would or would not work theoretically. I would also like to express my thanks to: Auke, Deyan, Guy, Ranajit, Wim, Kees, Shohei, Shahar, Pieter, Matteo, Atsushi, Musab, Gil, Florencia, Max, Johnno, Jianhuan, Shotaro, Billy, Aydin, Nicolas, Yohei, Jan-Willem, Niels, Sixue, Youwei, Lisanne, Martha, Karlien, Pawan, Siddharth, Runhai, Bingkun, Rueben, Shan, Dong, Junhai, Tiexing and Feng.

At last but not least, my special gratitude to my family, who have provided me with a through moral and emotional support and unconditional love in life.

Thanks for all your encouragement!

Lele Zhang
Delft
July 2019

Curriculum Vitae

Lele Zhang

08-07-1989 Born in Gansu, China.

Education

2016-2020 Ph. D. in candidate
Delft University of Technology, Delft, the Netherlands

2012-2015 Master of Science
Institute of Geology and Geophysics,
Chinese Academy of Sciences, Beijing, China

2008-2012 Bachelor of Science
China University of Petroleum (Beijing), Beijing, China

List of Publications

Journal Papers

- **L. Zhang**, E. Slob, J. van der Neut and K. Wapenaar, Artefact-free reverse time migration, *Geophysics*, 83, no. 5, A65-A68 (2018).
- **L. Zhang** and M. Staring, Marchenko scheme based internal multiple reflection elimination in acoustic wavefield, *Journal of Applied Geophysics*, 159, 429-433 (2018).
- **L. Zhang** and E. Slob, Free-surface and internal multiple elimination in one step without adaptive subtraction, *Geophysics*, 84, no. 1, A7-A11 (2019).
- **L. Zhang**, J. Thorbecke, K. Wapenaar and E. Slob, Transmission compensated primary reflection retrieval in data domain and consequences for imaging, *Geophysics*, 84, no. 4, Q27-Q36 (2019).
- **L. Zhang**, J. Thorbecke, K. Wapenaar and E. Slob, Data-driven internal multiple elimination and its consequences for imaging: A comparison of strategies, *Geophysics*, 84, no. 5, S365-S372 (2019).
- **L. Zhang** and E. Slob, Implementation of a fast algorithm for multiple elimination and transmission compensation in primary reflections, submitted to *Geophysical Journal International*.
- **L. Zhang** and E. Slob, Marchenko multiple elimination of a laboratory example, submitted to *Geophysical Journal International*.
- **L. Zhang** and E. Slob, A field data example of Marchenko multiple elimination, *Geophysics*, in press.
- J. van der Neut, J. Brackenhoff, M. Staring, **L. Zhang**, S. de Ridder, E. Slob and K. Wapenaar, Single- and double-sided Marchenko imaging conditions in acoustic media, *IEEE Transactions on Computational Imaging*, 4, no. 1, 160-171 (2017).
- G. A. Meles, **L. Zhang**, J. Thorbecke, K. Wapenaar and E. Slob, Data-driven retrieval of primary plane-wave responses, submitted to *Geophysical prospecting*.

Conference Abstracts

- **L. Zhang** and E. Slob, Electromagnetic Marchenko imaging in 1D, 16th GPR Conference, Hongkong, China (2016).
- **L. Zhang** and E. Slob, Electromagnetic Marchenko imaging in 1D for dissipative media, 86th annual SEG Conference and Exhibition, Dallas, TX, USA (2016).
- **L. Zhang** and E. Slob, Electromagnetic Marchenko scheme based internal multiple elimination for lossless media, 9th International Workshop on Advanced GPR, Edinburgh, Scotland (2017).
- E. Slob and **L. Zhang**, Obtaining local reflectivity at two-way travel time by filtering acoustic reflection data, 87th annual SEG Conference and Exhibition, Houston, TX, USA (2017).
- **L. Zhang**, E. Slob, K. Wapenaar and J. van der Neut, Marchenko scheme based artefact-free imaging, 80th EAGE Conference and Exhibition, Copenhagen, Denmark (2018).
- **L. Zhang** and E. Slob, Model-free internal multiple elimination in data domain, workshop of 88th annual SEG Conference and Exhibition, CA, USA (2018).
- **L. Zhang** and E. Slob, A comparison of data-driven internal multiple elimination strategies and their consequences for imaging, 81th EAGE Conference and Exhibition, London, UK (2019).
- **L. Zhang** and E. Slob, A field data example of Marchenko multiple elimination, 89th annual SEG Conference and Exhibition, San Antonio, TX, USA (2019).
- E. Slob and **L. Zhang**, Elimination of multiples from acoustic reflection data, 16th SAGA Biennial Conference and Exhibition, ELANGENI and MAHARANI, Durban (2019).